

Alma Mater Studiorum - Università di Bologna

DOTTORATO DI RICERCA IN
MONITORAGGIO E GESTIONE DELLE STRUTTURE E
DELL'AMBIENTE - SEHM2

Ciclo 35

Settore Concorsuale: 09/E3 - ELETTRONICA

Settore Scientifico Disciplinare: ING-INF/01 - ELETTRONICA

HARDWARE-SOFTWARE DESIGN OF EMBEDDED SYSTEMS FOR
INTELLIGENT SENSING APPLICATIONS

Presentata da: Matteo Zauli

Coordinatore Dottorato

Luca De Marchi

Supervisore

Luca De Marchi

Co-supervisore

Alessandro Marzani

Esame finale anno 2023

Well, shall we go?

Yes, let's go.

They do not move.

A tante persone, ma ad un sentimento, la vicinanza.

In ordine sparso a Federica Zonzini, Lorenzo Mistral Peppi, Luca De Marchi, Simone Sindaco, Igor Valič, Mariano Nerone, Valerio Antonio Arcobelli, Sabato Mellone, Valerio Coppola, Denis Bogomolov, Stefano Taccetti, Luca Di Bonaventura, Serena Moscato, Alessandro Marzani, Federico Montori, Marco Di Felice, Lorenzo Gigli, Alessandro Calvio, Tullio Salmon Cinotti e a chi mi son scordato, ma che non scorderò.

Alla mia famiglia.

Alla compagna della vita, Marta.

Contents

Introduction	XI
1 Precision Agriculture	1
1.1 How to measure a fruit	3
1.2 Architecture	4
1.2.1 Energy Harvester	8
1.3 Sensor node operation, thermal compensation and calibration	11
1.3.1 Timing and data acquiring	11
1.3.2 Thermal compensation	11
1.3.3 Data calibration	13
1.4 In-field test	15
1.5 Conclusions	19
2 Bioengineering	21
2.1 Vascular Phantoms Setup for ultrasonic investigation	24
2.1.1 Components and design	25
2.1.2 Hydraulic circuit	25
2.1.3 Control system	26
2.1.4 Design	27
2.1.5 Tests and performance evaluation	29
2.2 Smart Crutch	31
2.2.1 Motivations	33
2.2.2 Materials and Methods	34
2.2.3 Calibration	39
2.2.4 Results	42
2.3 Smart wearable system for chest and lung auscultation	45
2.3.1 Microphones	46
2.3.2 Gold Standard	50
2.3.3 Chestpiece	52

2.3.4	Electronic prototype	55
2.3.5	Setup	59
2.3.6	Results	62
2.4	Conclusions	70
3	Automotive	73
3.1	First prototype	75
3.1.1	Design	75
3.1.2	Installation	79
3.1.3	Development and test	80
3.1.4	Considerations	85
3.2	Final design	86
3.2.1	Design	87
3.2.2	Installation	90
3.2.3	Development and test	92
3.3	Conclusions	95
4	Structural Health Monitoring	97
4.1	Compressive Sensing	102
4.1.1	Basics	102
4.1.2	Data recovery algorithms	103
4.1.3	Proposed SHM architecture	103
4.1.4	Experimental validation	105
4.1.5	Results	107
4.2	IoT Toolchain Architecture	111
4.2.1	The Arrowhead Tools Project	112
4.2.2	The Eclipse Arrowhead Framework	113
4.2.3	Toolchain architecture	114
4.2.4	The Structural Health Monitoring Pilot	115
4.2.5	The Deployment Use Case	117
4.2.6	Integration with Legacy Systems	118
4.2.7	Results	119
4.3	Output-only SysId models for vibration analysis	121
4.3.1	New Hardware for SHM	122
4.3.2	Experimental validation	125
4.3.3	Results	126
4.4	Artificial Intelligence perspective	130
4.4.1	OCCNN-based vibration diagnostics	131

4.4.2 Experimental validation 133

4.5 Conclusions 137

Conclusions **139**

Copyright **141**

List of Figures

- 1.1 System architecture scheme. [©2021 IEEE] 5
- 1.2 Computer-Aided Design (CAD) view of the pliers components. 6
- 1.3 Battery voltage of the energy harvester during open field tests. It is worth noting that the battery is always fully charged, and even during bad weather days no significant battery discharge is noticeable. [©2021 IEEE] 9
- 1.4 Battery voltage acquired during test conducted in greenhouse. The sensor node stops working when the battery voltage becomes lower than 3.3 V due to poor lighting conditions. [©2021 IEEE] 10
- 1.5 Magnification of 18 March–28 March section in the plot of Fig.1.4. the energy supplied by the photovoltaic panel is not sufficient to cover daily consumption, thus causing the battery to discharge down to the shut-down threshold. [©2021 IEEE] 10
- 1.6 Scheme of the compensation stages. [©2020 IEEE] 12
- 1.7 Relation between opening distance and deviation from the best fit line. [©2020 IEEE] 14
- 1.8 Experimental in-field setup, apples monitoring. First prototype, single plier. 15
- 1.9 Data acquired compared with time and temperature perceived 16
- 1.10 Summer 2022 experimental setup, four pliers. 17
- 1.11 Particular of the aggregator sensor node from 2022 setup. 17
- 1.12 Citrus fruit setup. 18

- 2.1 Designed flow phantom setup scheme. [©2019 IEEE] 25
- 2.2 Closed-loop control. [©2019 IEEE] 27
- 2.3 Target flow black track, flowmeter acquisitions green track. [©2019 IEEE] 28
- 2.4 Open-loop control. [©2019 IEEE] 28
- 2.5 (a) Vascular Phantom (b) Flow Simulator Prototype. [©2019 IEEE] . . . 29
- 2.6 Magnetic flowmeter and eco-doppler acquisitions. [©2019 IEEE] 29
- 2.7 Main types of crutches. 32

2.8	System Overview: mCrutches and Mobile App.	34
2.9	mCrutch assembly: (a) mCrutch final prototype; (b) battery placement; (c) Tip modified mechanical structure embedding the miniaturized load cell (d) plastic protective case containing the electronics and (e) handle's front panel with the status led, the power button, and the USB port for battery charging.	35
2.10	Diagram of electronic connections.	36
2.11	Layers of the mCrutch system architecture. The figure shows the flowcharts of the Arduino/data collection layer (A), the communication layer (B), and the mCrutch app layer (C).	38
2.12	Smart Crutches app layout and descriptors: (A) button control panel; (B) message panel from system or mCrutch; (C) chronometer and switch for a real-time plot; (D) data indicator for both pitch [°] and applied force [N]; (E) live-chart of pitch [°] in upper graph and applied force [N] in the lower graph.	39
2.13	Calibration setup: laboratory environment (a) and marker positioning (b).	40
2.14	Relationship between the mCrutch reference frame and the laboratory ref- erence frame.	41
2.15	Smart tip calibration performance and distribution of the difference be- tween FP and mCrutch.	43
2.16	Smart tip calibration performance and distribution of the difference be- tween FP and mCrutch.	44
2.17	Murata Piezoelectric Diaphragms 7BB-35-3L0.	48
2.18	Primo Electret Condenser Microphone EM272Z1.	48
2.19	STMicroelectronics Analog MEMS microphone MP23ABS1: (a) device, (b) STEVAL-MIC004V1 evaluation board.	49
2.20	STMicroelectronics Digital MEMS microphone IMP34DT05: (a) device, (b) STEVAL-MIC003V1 evaluation board.	49
2.21	Thinklabs One, digital stethoscope.	50
2.22	eKuore, digital stethoscope.	51
2.23	Stethoscope parts [110].	53
2.24	Cup for piezoelectric diaphragm.	54
2.25	Cup size small, for electret condenser mic.	54
2.26	Cup size big, for electret condenser mic.	54
2.27	Cup size small, for MEMS mics.	55
2.28	Cup size big, for MEMS mics.	55
2.29	“Piezoelectric preamplifier board” electronic schematic.	56

2.30	“Analog preamplifier board” electronic schematic.	57
2.31	The developed auscultation device prototype components.	59
2.32	Laminated plywood board, part of the auscultation phantom setup to test microphone technologies.	60
2.33	Auscultation phantom setup, on left side the Position 1, on right one Po- sition 2.	60
2.34	Test of piezoelectric diaphragm (left) and digital MEMS (right).	61
2.35	RDNet settings for white noise generation.	62
2.36	Position 1, normalized PSD microphones acquisitions with white noise. . .	64
2.37	Position 1, normalized PSD microphones acquisitions in total silence. . . .	65
2.38	Position 2, normalized PSD microphones acquisitions with white noise. . .	66
2.39	Position 2, normalized PSD microphones acquisitions in total silence. . . .	67
3.1	Architecture scheme of the described system. [©2021 IEEE]	75
3.2	Station board architecture scheme. [©2021 IEEE]	77
3.3	Sensing board architecture scheme. [©2021 IEEE]	77
3.4	The mechanical system that anchors the Sensing Board to the shaft. [©2021 IEEE]	78
3.5	Position of the main installed thermocouples. [©2021 IEEE]	80
3.6	Top and bottom side of the first prototype. [©2021 IEEE]	81
3.7	The climate chamber accuracy test. Red line, climate chamber target tem- perature. Grey band, $\pm 1^\circ\text{C}$ than target. [©2021 IEEE]	82
3.8	The high temperature validation test performed in a Carbolite Gero AX 30 laboratory oven (with a temperature uniformity of 5°C at 250°C). Grey band, $\pm 1^\circ\text{C}$ than target. Orange band, $\pm 5^\circ\text{C}$ than target. [©2021 IEEE]	82
3.9	Upper plot, typical temperature trends obtained from simulations (blue line) and from experiments (red line). In the bottom plot, a sample ac- quisition of the temperature profile performed with the novel system is displayed (green line). [©2021 IEEE]	83
3.10	A 1:1 scale 3D printed motor model where is clear that the end windings are not in direct contact with the cooling circuit (as one might mistakenly conclude looking only at Fig. 3.5). [©2021 IEEE]	84

3.11	Digital timing diagram of the presented system, from top to bottom: – orange line is high when the Terminal (see Fig.3.1) command arrives on the Station Board VCOM and low when the answer is sent back to the Terminal, – green line is high when the Station Board forwards the command via BLE to the Sensing Board and low when the Station Board receives the response from the Sensing Board via BLE, – pink line is high when the Sensing Board receives the command via BLE and low when the Sensing Board sends the response via BLE, – blue line is high when the sensing board starts acquiring from thermocouples and low when the sensing board stops acquiring from the thermocouples. [©2021 IEEE]	85
3.12	New architecture proposed. [©2022 IEEE]	87
3.13	The integration of the PCB into the shaft. [©2022 IEEE]	87
3.14	Acquisition Board architecture scheme. [©2022 IEEE]	89
3.15	Top and bottom side of the first prototype of the Acquisition Board. [©2022 IEEE]	89
3.16	Communication Board architecture scheme. [©2022 IEEE]	90
3.17	Temperature distribution in the shaft in upper limit temperature condition. [©2022 IEEE]	92
3.18	The accuracy validation test performed in a Carbolite Gero AX 30 laboratory oven prove that the thermocouples used are accurate from 50 °C up to 250 °C. [©2022 IEEE]	93
3.19	Climate Chamber data. The upper plot shows temperatures measured by the thermocouples placed outside the chamber while the electronics was kept inside the chamber at a rising temperature (lower plot). All x-axis are reported in seconds. [©2022 IEEE]	94
4.1	The proposed HW/SW architecture for modal analysis. From left to the right, the compression/decompression stages are allocated to the PSNs and the CHNs, respectively. Then, the pure modal analysis is performed, firstly identifying cluster-related modal shapes Φ_j and then merging the local estimates into a full-scale modal shape matrix Φ . Finally, the current health status can be derived by monitoring trends in MAC values over time.104	
4.2	Experimental testbed and related sensor installation plan, comprising two clusters (C1 and C2, respectively) of six accelerometers. An inset depicting the practical connection of three PSNs is also enclosed.	105

4.3	Left: trend in MAC values between CS-reconstructed and compression-free full-scale modal shapes as a function of the compression ratio, superimposed to the chosen accuracy level indicated by the black-dotted line at 90%. Red-rumbled, green-rounded and blue-squared line styles refer to the first, second and third modal shape, respectively. Right: reconstructed full-scale modal shapes for a representative selection of CR values.	108
4.4	Cost analysis for the considered recovery algorithm. In the left-hand side, memory occupancy, execution time and ARNSR are displayed from top to the bottom. The MTA product between the three curves per CR is conversely displayed in the right panel.	109
4.5	Example of IHT-reconstructed signal over 29 different signal frames.	110
4.6	A graphical overview of the Arrowhead Tools Engineering Process. [©2023 IEEE]	113
4.7	Generic toolchain architecture for condition monitoring.	114
4.8	Toolchain architecture of the whole System-of-Systems. Main abbreviations are: WT (Web Thing), SN (Sensor node), CH (Cluster Head), WAE (WoT Arrowhead Adapter), ATM (Arrowhead Thing Mirror), OAS (OpenAPI Specification), AHA (Arrowhead Adapter), SR (Service Registry), A (Authorisation), O (Orchestration).	116
4.9	Bridge model under test. [©2023 IEEE]	117
4.10	Sensor readings of the SHM sensors on MODRON, it shows an accelerometer bursts that change after the vibrodyne is turned on. [©2023 IEEE]	118
4.11	Sensor readings of the gas sensor on MODRON, it shows how the data from the gas sensor changes before and after the gas sensor is sprayed with gas. [©2023 IEEE]	119
4.12	Top and lateral view of the developed Sensor Node	122
4.13	SM141K09L solar cells during test.	124
4.14	Electromagnetic Energy Harvester.	124
4.15	Experimental setup: simply supported steel beam with magnified damage positions (blue, red and green marker).	126
4.16	Normalized power spectra computed via the embedded ARMA(16,16) (blue) and AR(16) (red) SysId algorithms, compared to the Welch (black) estimation performed offline.	128

4.17	Normalized power spectra in damaged configurations computed by the SN from ARMA (top) and AR (bottom) model parameters. Apart from the mass-free configuration (label Nom), a dead mass as been hanged at three different positions to simulate the effect of anomalies. Grey background boxes have been included to underline the variations in the peak spectral values.	129
4.18	Workflow for OCCNN-based anomaly detection combined with OMA. . . .	131
4.19	Sequence of steps to be implemented to transform NN architectures from Cloud/Server-based Tensorflow programming to MCU-compliant ML models passing through Tensorflow Lite quantization.	134

Introduction

The aim of this Dissertation is to highlight the importance of well designed and developed embedded systems in the implementation of intelligent sensor networks. Indeed, in many works presented in literature, the focus is on the processing, or in the software architecture and in the networking aspects, while the devices which host these elaborations are somehow overlooked, and the demonstration activities are often based on commercial evaluation boards, or simulations on a PC. Conversely, this Thesis puts a strong accent in the Embedded systems' Hardware implementative aspects, as key enablers for the development of the highest abstraction layers. Obviously, this does not mean that the data processing aspects are neglected, but simply that the focal point is on the complexities of ad-hoc electronic boards prototyping. Even if most of the smart systems proposed in this Thesis are based on ad-hoc boards, it must be anticipated that, in some cases, due to the electronic components shortage experienced in the last years, it was not possible to design full custom boards. In these cases, I opted for hybrid solutions merging purposely-developed boards and commercial ones. Such solution is compatible with the realization of compact and high-performing devices.

In my research activity, during the last three years, I had the pleasure to forge collaborations with academic and industrial partners and to participate in a national inter-university project, in two industrial projects and in an European one.

Concerning academic collaborations, this Thesis will show how my research has been a truly multidisciplinary activity. As a member of the Department of Electrical, Electronic and Information Engineering (DEI), Intelligent sensor system lab, I collaborated with the Emerging biomedical technologies for diagnosis and therapy Laboratory, and the Personal Health Systems Laboratory.

At the University of Bologna, I had also the opportunity to collaborate with researchers belonging to different Departments: the Department of Agricultural and Food Science and Technology (DISTAL), the Department of Medical and Surgical Sciences (DIMEC), the Department of Computer Science and Engineering (DISI) and the Department of Civil, Chemical, Environmental, and Materials Engineering (DICAM). Moreover, I worked with

researchers of the following institutions: Politecnico di Milano, University of Modena and Reggio Emilia and ETH Zürich.

Concerning industrial partnerships, I cooperated with HPE COXA of Modena, an automotive company, and Rete Ferroviaria Italiana (RFI), in the railways sector.

All these collaborations gave me the chance to study embedded systems and their intelligent sensing applications in many field. Specifically, in this Thesis, four application areas are presented: precision agriculture, bioengineering, automotive and Structural Health Monitoring (SHM). More in detail, Chapter 1 is about a precision agriculture project. In particular, the design and development of a fruit meter is presented. In the bioengineering field, I faced three different projects, which are reported in Chapter 2, detailing the architectures implemented and the validation tests conducted. Two prototypes realization of an inner temperature measurement system in electric motor are reported in Chapter 3, for an automotive application.

Lastly, in Chapter 4 a global combination of embedded hardware and software techniques is illustrated: the goal is the realization of a Smart Sensor Network for Structural Health Monitoring applications, featuring on-board data management and processing, integration in an IoT toolchain, Wireless connectivity and Artificial Intelligence capabilities.

Chapter 1

Precision Agriculture

Abstract

During my studies on embedded systems, one of the first application domains I approached was Precision Agriculture, thanks to a collaboration with the Department of Agricultural and Food Science and Technology of the University of Bologna. This project led to the realization of a device to track the fruit growth rate and it's currently being used in many research activities related to orchards monitoring. The developed hardware it is not characterized by a high level of integration (as the one which can be reached by designing ad-hoc PCB), but it is mainly based on evaluation- and developer-boards. This choice was due to three main reasons: i) necessity to speed up the device prototyping phase, ii) no stringent requirements about device dimensions from the end-users, iii) electronic components shortage. This research has led to the development of a microcontroller based system, featuring energy harvesting and on-board processing capabilities for an innovative sensing approach.

Introduction

Precision Agriculture, or Agriculture 4.0, tackles important challenges like rising populations boosting the need of food, necessity of greener approaches for farmland sustainability and threats to productivity related with climate changes [1][2]. Facing such challenges benefits from recent technology developments, bringing forward Digital Agriculture [3], that is, Precision Agriculture and the entire farm production value chain [4].

Precision Agriculture is based on a wide range of enabling technologies: GPS guidance, control systems, sensors, robotics, autonomous vehicles, Variable Rate Technology (VRT), Internet of Things, drones and Big Data powering Artificial Intelligence use and Cloud Computing [5][6]. The farmer perceives difficulties to uptake new digital technology because of barriers like: high costs, complexity, lacking of appropriateness for farming contexts, interoperability and precision. Besides, Digital Agriculture frequently lacks a

clear added-value to farming activities, and also lacks a value proposition [7]. These difficulties are typical in many fields when faced with innovation adoption, and agriculture is not an exception. Therefore, complexity of operation is one perceived obstacle to the adoption of Precision Agriculture, and efforts must be made to boost adoption of simple, easy to deploy and manage systems.

The goal of my study is to overcome these limits by realizing a smart sensor which monitors fruit growth during the growing season, in order to provide real-time information to the orchard manager. The utility of this information is twofold: to guide management decisions, and to confirm the soundness/lack of effectiveness of those already implemented.

This chapter provides an introduction about fruit meters, then presents the architecture of the sensor node designed, and discusses the calibration technique and on-board temperature compensation method. Results are presented together in-field usage and validation.

The content of this Chapter is based upon the research works [P1] and [P2]:

- “A Low-Cost and High-Accuracy Non-Invasive System for the Monitoring of Fruit Growth” by Peppi L. M., Zauli M., Manfrini L., Traverso P. A., Grappadelli L. C., De Marchi L. in 2021 IEEE International Workshop on Metrology for Automotive (MetroAutomotive), pp. 248–253, 2021. ©2020 IEEE.
- “Implementation and Calibration of a Low-Cost Sensor Node for High-Resolution, Continuous and No-Manning Recording of Fruit Growth” by Peppi L. M., Zauli M., Manfrini L., Grappadelli L. C., De Marchi L., Traverso P. A. in 2021 IEEE International Instrumentation and Measurement Technology Conference (I2MTC), pp. 1–6, 2021. ©2021 IEEE.

From which part of the text is drawn. I participated in the choice of electronic components and in the firmware developing.

1.1 How to measure a fruit

The measurement of the fruit diameter gives useful information which can be used for research purposes and in support to farming practices, to evaluate the tree water status [8], as well as in models developed to manage orchard irrigation [9].

Different systems to measure continuously fruit or stem growth have been developed. The use of Linear Variable Displacement Transducer sensors [10], linear potentiometer [11] or strain gauge [12, 13] allows to achieve very high resolution of the measure at the expense of a very small measurable length, requiring every few days relocation of the measuring unit on the fruit. The relocation process is time consuming and requires labour intervention, leading to an increased cost of the measure. Different systems with a maximum measurable range were also developed using optical readers, like [14], but their resolution turned out to be unsuitable for acquiring night-and-day growth variations.

In this thesis, a low power, inexpensive and high accuracy sensor node is described. The sensor is able to measure continuously fruit diameter in a non-invasive or damaging way without requiring any relocation during the whole growing season, with a geometrical effective resolution suitable for the estimation of sub-millimetre variations, which are typical of fruit diameter dynamics along a single-day time interval scale. Moreover, the response of the system should be made strongly immune to environmental conditions (in particular, daily temperature fluctuation).

1.2 Architecture

The main components of the mechanical designed system are:

- Potentiometer-based angular sensor, measure system core;
- Plier, catches the fruit to measure;
- Low-power Microcontroller Unit, acquisition and processing;
- Micro-SD card adapter, data storage;
- LoRa transceiver, data transmission;
- Linear DC/DC converter, generates the 3.3V required for the system and to control the power for the angular sensor;
- Solar Energy Harvester and lithium-ion battery, power supply;

In Figure 1.1, it is shown the tool part (plier) and the electronics side, which can host up to five pliers. Therefore, the sensor node designed operates as aggregator of a maximum of five fruit sensor outputs. The node requires a power supply greater than 3.6 V for the whole system. For the first testing phase, a common power bank for mobile phones was used, than it has been equipped with a solar energy harvester and a single cell lithium battery. Each unit of the system will be detailed in the following.

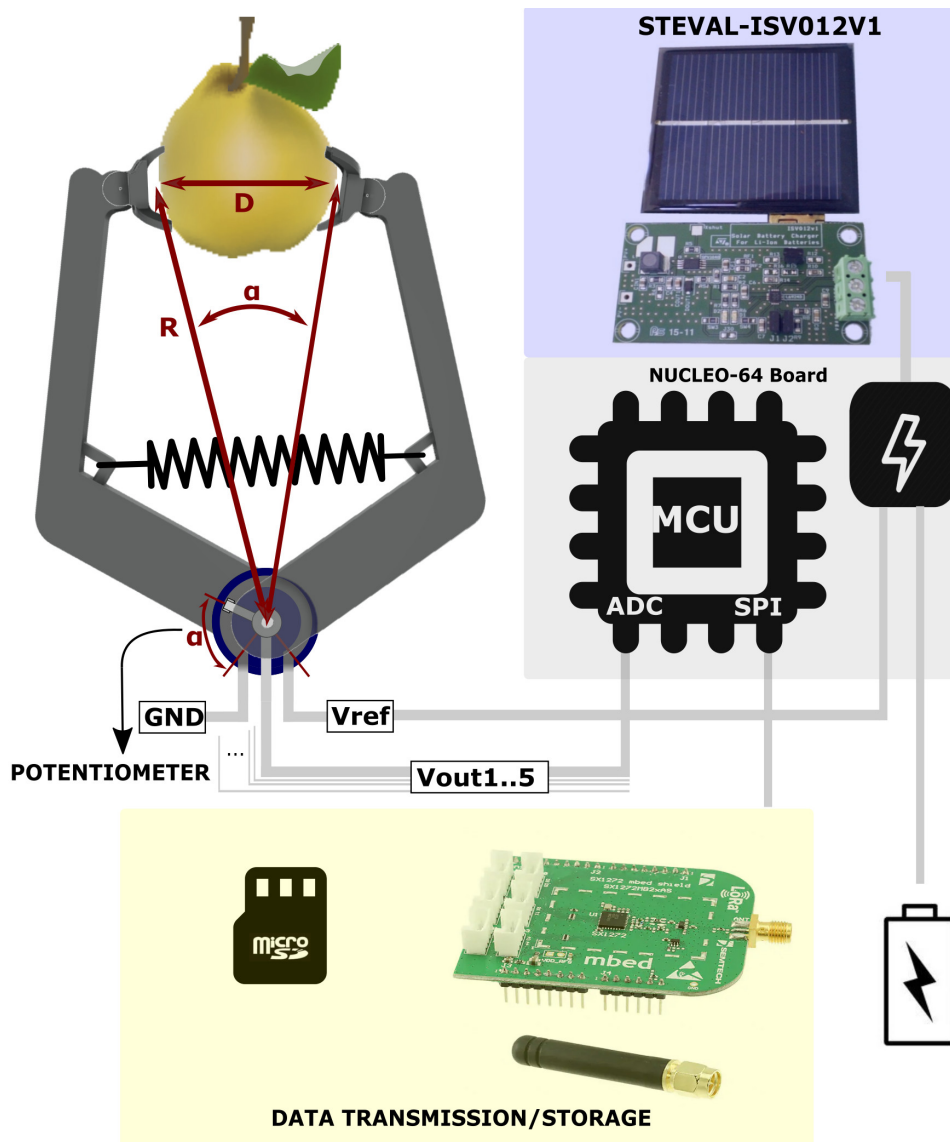


Figure 1.1: System architecture scheme. [©2021 IEEE]

- The angular sensor, for this particular prototype, is a single-turn potentiometer, assembled on the pivot of the plier. Aperture variations of the plier directly modify the resistive partition ratio, and the transduction of the measurand into a voltage V_{out} can be obtained, which is a fraction of the supply applied to the potentiometer. The single-turn resistive potentiometer has been accurately selected in order to match its angle range with the maximum aperture of the plier. This potentiometer, manufactured by TT Electronics, model PHS11-1DBR10KE60 [15], is dust proof and has a low electrical angle of sixty-degrees which allows to use the whole dynamic range offered by the ADC converter.
- Up to 5 pliers for each board, which are manufactured making use of a 3D printer in Acrylonitrile Butadiene Styrene (ABS). The plier must be extremely light to

avoid warping of the fruit. It should also not change its shape with temperature and should be resistant to UV radiation. At the present the plier was printed using “ABSpeciale”, from FiloAlfa [16]. This material is selected because of its heat resistance and quite high bending temperature, as well as ease of print. It is composed of two arms linked together with a small bolt and restrained with a spring. The two retains for the potentiometer and the shaft are interlocked with the two arms. The mathematical relation between angle α and distance D , is given by the following formula:

$$D = 2 \cdot R \cdot \cos\left(\frac{\pi}{2} - \frac{\alpha(V_{out})}{2}\right) \quad (1.1)$$

where R is the length of plier’s arm. The value of α is linearly dependent on the partition ratio, thus on the output voltage.

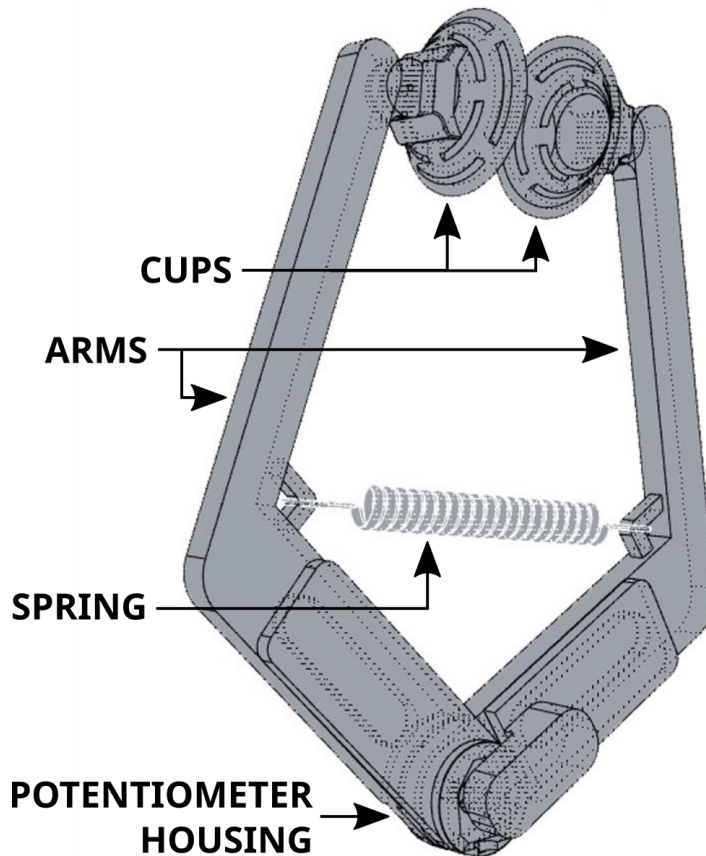


Figure 1.2: Computer-Aided Design (CAD) view of the pliers components.

The plier aperture is equal to 12 cm, which is adequate for the diameter of a fully grown apple, peaches, oranges or kiwis and other fruit.

- The development board STM32 Nucleo-64 with a STM32L152RE microcontroller has been used to acquire and process data. This MCU is made up of a low energy consumption ARM Cortex M3 core operating at a maximum frequency of 32 MHz, flash

memory of 512 kilobytes and RAM of 80 kilobytes and one Successive-Approximation ADC with a bit depth of 12-bit and up to 40 channels. The full-scale voltage of the ADC equals to that of the MCU power line (3.3 V) and potentiometers supply, and can be fully exploited to convert the voltage at the output of a potentiometer, thanks to the accurate matching of plier aperture range and potentiometer maximum turn angle. The ADC quantization step (of about $806 \mu\text{V}$) defines the nominal resolution of the sensor, whose value can be approximately estimated in $30 \mu\text{m}$. The internal temperature sensor is used, which is accessible with the ADC converter integrated in the STM32L152RE. All acquired and computed data are stored into an SD card.

- The LoRa transceiver uses an MBED SX1272MB2DAS [17] demoboard, fitted with a Semtech SX1272 [18] transceiver. All RF-related circuitry is relegated to this board, which is connected to the Nucleo-64 via a set of arduino-compatible connectors. The SX1272 transceiver is designed to operate in the 868 MHz frequency band and it communicates with the microcontroller via an SPI interface. In addition, Digital IO lines are used by the Semtech LoRaMac-node stack to interface with the transceiver. The power supply line of this board is connected directly to the Nucleo board, whose power supply stage is used.
- A high quality power supply is required for this application since supply noise determines instability in the measured data and variations of the mean voltage can lead to inaccurate readings. The powering of the potentiometer must be controlled, in order to minimize the energy consumption of the system. For these reasons two linear, Low Drop Out (LDO), DC/DC converter are used. The first one, LD39050PU33R [19] from STMicroelectronics, is used to supply the MCU and it is available in the Nucleo board. It can reach very good performance in terms of output voltage noise ($30 \mu\text{VRMS}$ over 10 Hz to 100 KHz bandwidth) and thermal stability. This power line is also used as reference voltage for the ADC converter. The second one, MIC5365-3.3YD5-TR [20] from Microchip, is used only to give power to the potentiometer. In order to decrease the energy consumption of the system the enable pin of this DC/DC converter is used. The MCU enables the LDO just before readings start, taking into account the power up transient, and disable it when readings are over. It is worth noting that this LDO has worse thermal stability with regard to the STM one.
- The Energy Harvester is based on STEVAL-ISV012V1 [21] evaluation board from STMicroelectronics. This board includes a 400 mW_{peak} photovoltaic panel (model SZGD6060-4P from NBSZGD), a SPV1040 [22] step-up converter with MPPT (Maximum Power Point Tracker) and a L6924D [23] charge controller for lithium-ion bat-

teries, both from STMicroelectronics. The use of a step-up converter with MPPT algorithm permits to continuously tracks output voltage and current of the solar cell, and therefore allows to maximize the harvested energy, increasing the overall efficiency of the stage. The li-ion battery used has a capacity of 4.7 Ah, to suit indoor application too (more details in the next section 1.2.1).

1.2.1 Energy Harvester

A key point of the target application is install the sensor nodes in orchards, or greenhouses, at the beginning of fructification at take them back when is near the fruit ripening. Consequently, it is fundamental get an autonomous system whereby my team and I have given attention to power budget. That's why an Energy Harvester has been studied and applied.

Basing on consumption estimates and planned duty cycles, it is possible to determine the most suitable energy source to ensure high system autonomy. One acquisition cycle, consisting of interrogating all five sensors every 600 seconds, processing and storing of data on the SD card, requires a total of 1.63 J, such estimation being performed by averaging data from different manufacturers [24]. With a 500 mAh battery the operating time of the system is around 25 days, without taking into account self-discharge phenomena, while for many fruit species the growth and ripening times are much longer [25, 26]. Therefore, the mentioned battery is not suitable for a virtually maintenance-free device. Increasing the battery capacity is not practical: at the beginning of the season all the batteries should be charged, and if the number of nodes is high many chargers are needed, which could be a significant cost, because of their price and required manpower, even if Wireless Power Transfer is used to charge batteries, such as in [27]. For this reason, the adoption of a photovoltaic harvesting sub-system, with a small rechargeable back-up battery, was considered the optimal solution. This avoids the use of external chargers or non-rechargeable batteries, which are by their nature a major source of pollution. In addition, the state of charge of the batteries does not have to be monitored periodically, since the back-up battery is able to keep the node powered during night and when bad weather occurs for few days. Tests carried out in open field, at the farm of the Faculty of Agriculture of University of Bologna (Cadriano, Bologna) between June and August 2021, have shown how this solution is able to ensure a sufficient power supply to power the prototype: the harvester is able to keep the battery fully charged during the day, while during the night the discharge is minimal, as it is possible to appreciate in Figure 1.3. It is worth noting that the test was carried out in rows protected by rain-hail nets and the photovoltaic panel oriented in the east direction.

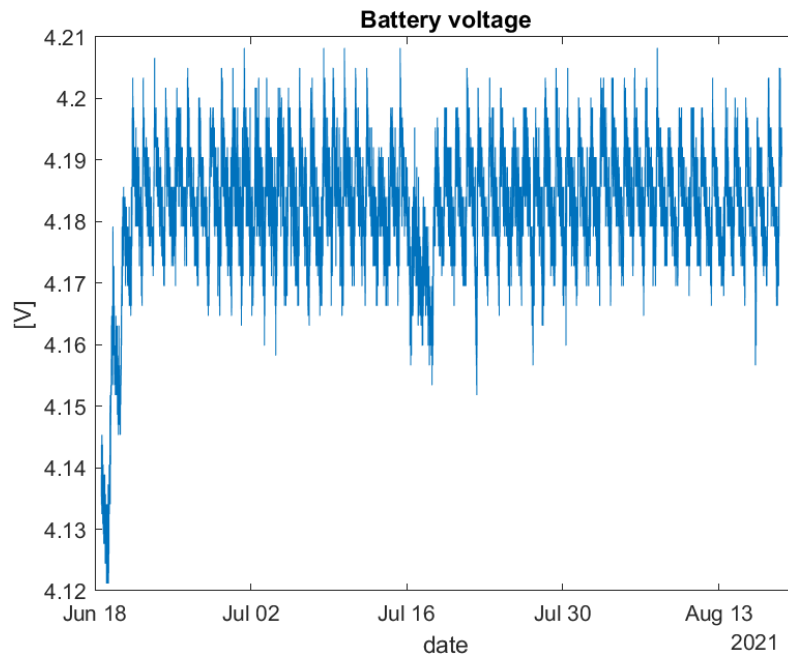


Figure 1.3: Battery voltage of the energy harvester during open field tests. It is worth noting that the battery is always fully charged, and even during bad weather days no significant battery discharge is noticeable. [©2021 IEEE]

The sensor-node prototype could also be used indoors: for this reason, an additional test was carried out under critical lighting conditions and during periods with a limited number of daily sunshine hours. The prototype was placed from 18 March 2021 to 30 April 2021 inside the greenhouses of the Faculty of Agriculture of the University of Bologna. The lighting control inside the greenhouses is managed autonomously, through an automated system of reflective curtains, in order to control the internal temperature: in case of intense sunshine greenhouses are partially darkened, allowing only diffuse lighting. Therefore the panel of the prototype, although it was oriented in a south-west direction, was never illuminated by direct light. In order to accelerate the charge/discharge profile, a 3.7 V 350 mA h Li-Ion battery was initially used in the test. In Fig. 1.4 it can be seen that the harvester was unable to keep the battery in a charged condition, causing the prototype to be shutdown due to lack of power on 29 March. Subsequently, from 10 April a pre-charged 4.7 A h battery replaced the previous one in order to continue the test. By zooming the interval 18 March–28 March in Figure 1.3 the resulting plot in Figure 1.5 shows that the previous 350 mA h battery is mildly charged during the day, but not enough to compensate for the energy consumed when the charging is not in progress.

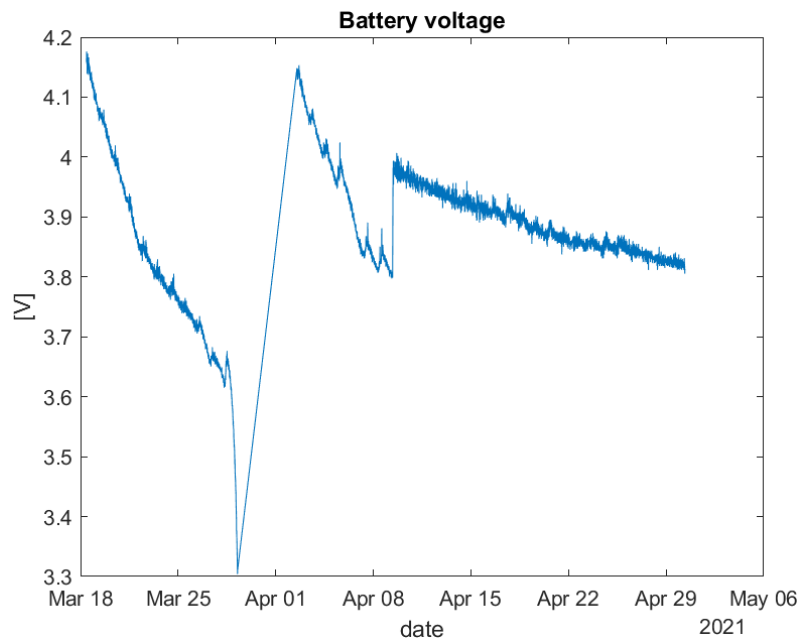


Figure 1.4: Battery voltage acquired during test conducted in greenhouse. The sensor node stops working when the battery voltage becomes lower than 3.3V due to poor lighting conditions. [©2021 IEEE]

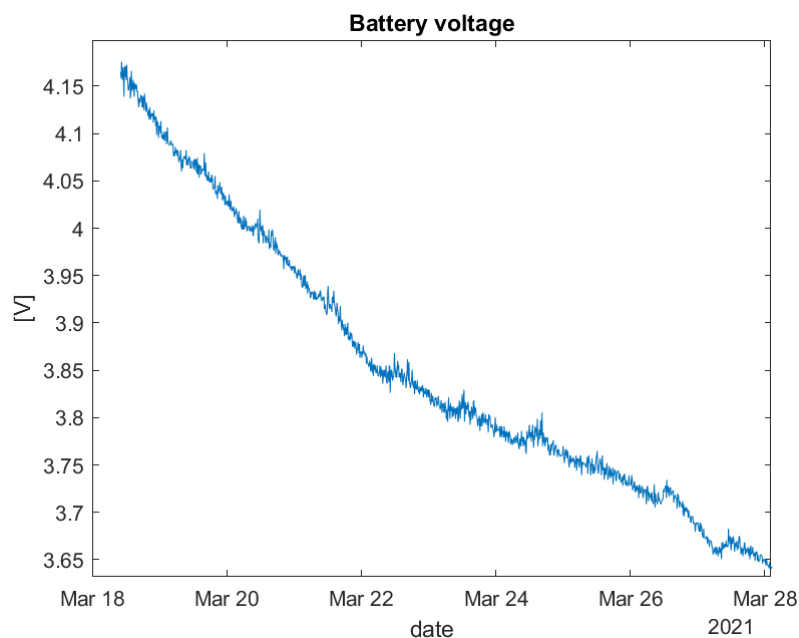


Figure 1.5: Magnification of 18 March–28 March section in the plot of Fig.1.4. the energy supplied by the photovoltaic panel is not sufficient to cover daily consumption, thus causing the battery to discharge down to the shut-down threshold. [©2021 IEEE]

1.3 Sensor node operation, thermal compensation and calibration

In this section on-board processing for thermal compensations and the whole logic of the device will be detailed.

1.3.1 Timing and data acquiring

One timer of the STM32 is used to generate an interrupt signal to trigger the sensor reading. This interrupt invokes a function that starts the reading and elaboration sequence of instructions.

A trade-off between accuracy and power consumption must be considered in the number and length of the sample records. More precisely, the general strategy for obtaining a single, final reading consists in acquiring M records of N samples each, and then to compute a double-average estimate \bar{d}_R

$$\bar{d}_R = \sum_{m=1}^M \sum_{n=1}^N d_{(R,n)}^m(V_{out}) \quad (1.2)$$

where $d_{(R,n)}^m$ is the n -th sample of the m -th record, used to filter out additive noise and short-time fluctuations of the influence quantities on the sensor response.

The values $M = 10$ and $N = 250$ have been found to be the optimal trade-off so far. With a total of 2500 samples, the standard deviation of the estimator in (1.2) is found negligible with respect to the other sources of uncertainty, while the power consumption to obtain \bar{d}_R is still very low.

In order to compensate the effect of temperature and obtain ready-to-read results, an algorithm based on an analytical separation of the two main perturbing effects is employed.

1.3.2 Thermal compensation

Two main temperature variation effects to be compensated were observed in this application. First of all, thermal compensation of the ADC and DC/DC converters has to be considered. While temperature is increasing, data acquired is found to linearly decrease, following the relation

$$\bar{d}_{R - T_{\text{norm}}} = \bar{d}_R(1 + \Delta T \times C_{\text{th}}/100) \quad (1.3)$$

A constant percentage correction factor C_{th} can be obtained keeping the plier at a constant angle and applying a cycle of temperature variations thanks to a climate chamber.

All data collected are used to estimate the best fit line between the measured values and the differences between the perceived temperature and a reference temperature. The angular coefficient of the best fit line represent the relation between the two quantities. Normalizing this number with the mean value measured by the ADC and multiplying it x100 the constant percentage correction factor C_{th} is obtained. The extraction of the C_{th} coefficient was made through the use of a climatic chamber (Galli Genviro 060 [28]).

By doing so, the temperature residual effect throughout the range 20-70 °C becomes comparable to the nominal RMS quantization noise.

A second step is necessary to compensate for the thermal expansion of the plier, which is the second perturbing effect. ABS has a linear thermal coefficient of expansion λ of about $10^{-4}K^{-1}$. Thermal expansion value ΔL , which is computed using the same ΔT used in (1.3), is added with the nominal length of the plier (where the nominal length L is the value measured when $\Delta T = 0$). Then, it is possible to re-write (1.1) as

$$\bar{d}_R = 2 \cdot (L + \Delta L) \cdot \cos\left(\frac{\pi}{2} - \frac{\bar{d}_R - T_{norm}}{2}\right) \quad (1.4)$$

The above compensation process is outlined in Figure 1.6.

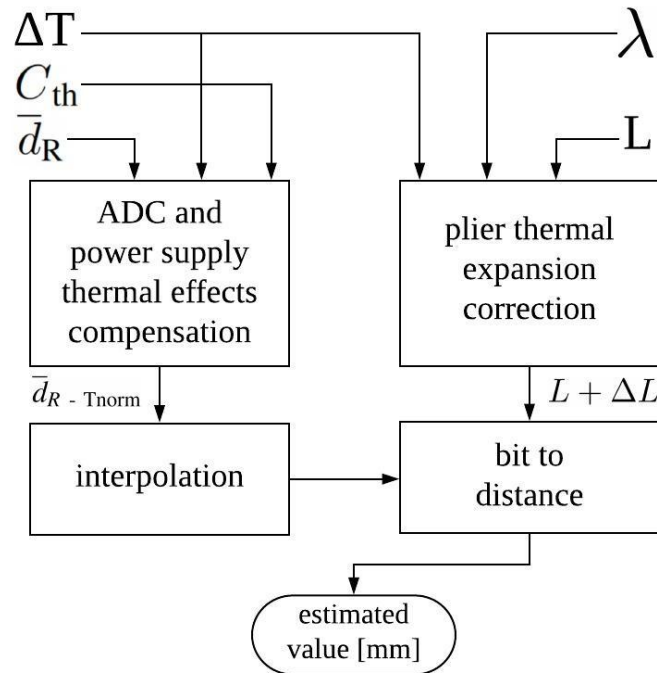


Figure 1.6: Scheme of the compensation stages. [©2020 IEEE]

1.3.3 Data calibration

The value found by (1.4) is affected by a fixed offset, caused by the dimension of the cups used to grab the fruit, and keeps all the non-linearities caused by inherent non-idealities of the production process of the potentiometer. So this value cannot be defined as the best length estimate.

In order to solve these problems a cubic-spline interpolation was adopted. The calibration of the interpolation coefficients was performed using a caliber and a precision lift platform. The measured opening of the plier, taken with caliber, and \bar{D}_R , acquired with the interpolation process disabled, were stored into the MCU memory, and every time the system was powered polynomial coefficients were calculated.

A dedicated function in the MCU takes the current value of \bar{D}_R and automatically solves the equation with the previously computed right coefficients, in order to obtain the best estimated value.

The points used in the calibration process were used to compute the best fit line, which can be expressed, for the components used in the plier depicted in Fig. 1.2, with the following equation:

$$y = 0.9487 \cdot \bar{D}_R + 14.09 \quad (1.5)$$

where y [mm] represents the expected value to be measured experimentally.

Equation 1.5 was used to compute y , and the real measured opening distances were subtracted to it in order to determine the deviation z between the real measured value and the estimated value by the best fit line. The mean value found of the deviations is $\bar{z} = -0,002502273$ [mm] while the standard deviation is $\sigma_z = 0,77335495$ [mm].

From these results it follows that the potentiometer characteristic is slightly non-linear. However, the calibration algorithm previously introduced can be used to compensate the non-linearities.

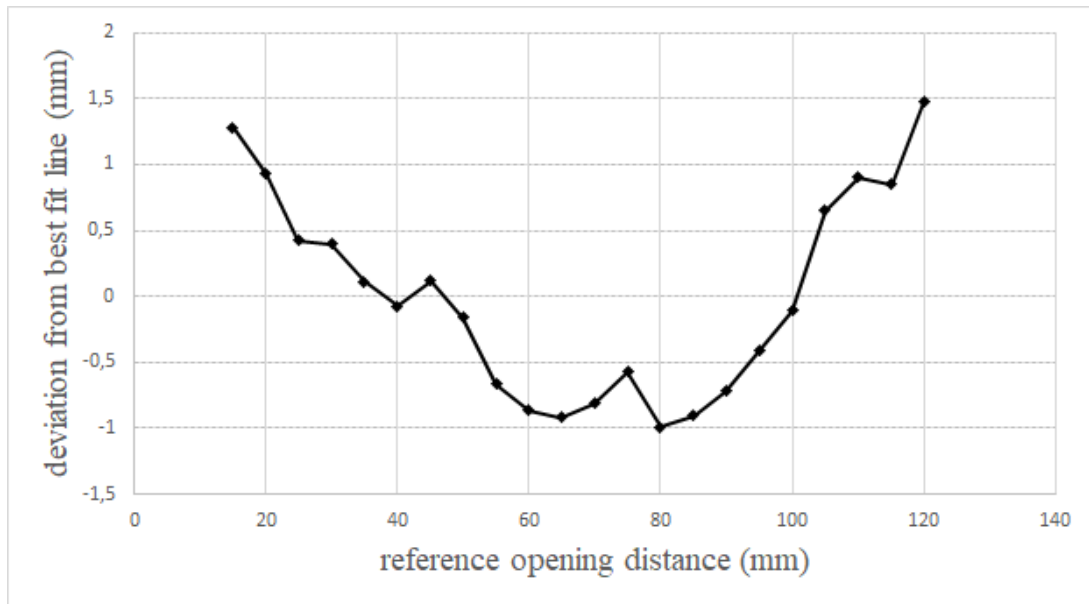


Figure 1.7: Relation between opening distance and deviation from the best fit line. [©2020 IEEE]

Analyzing more carefully the deviations from the best fit line, represented in Fig. 1.7, it can be noticed that potentiometer non linearities have just a modest effect.

It is important to emphasise that the calibration process and the extrapolation of thermal coefficients has to be performed for each sensor/plier.

1.4 In-field test

The first trial (Fig. 1.8) was conducted for three days and nights, from 13th July to 16th July 2020 (collected data Fig. 1.9), in an apple (*Malus x domestica* Borkh., cv “Fuji-Fujiko”) orchard located at the experimental farm of the Department of Agriculture and Food Sciences and Technology of Unibo (44.5543 N - 11.41872 E). The orchard was established in early 2019 in a deep silt-clay soil. Orchard row spacing was 2 m and tree spacing was 3.0 m. Trees were grafted onto “M9” rootstock and trained to a multi-axis system (10 axis/tree) with a Nord-Sud orientation. The irrigation system consisted of drip irrigation with a distance between emitters of 0.5 m and emitter flow of $2.3 L \cdot h^{-1}$. The orchard was managed according to commercial practices, including manual fruit thinning to achieve optimal crop load, winter pruning to maintain the desired training system, mineral fertilization, pest control and diseases, herbicide application below the trees and mowing of inter-canopy cover crop.



Figure 1.8: Experimental in-field setup, apples monitoring. First prototype, single plier.

Readings of opening angle were performed every 30 seconds. All data were processed directly into the MCU and the results saved into the SD card along with raw data for comparison purposes. Sample data are plotted in Fig. 1.9.

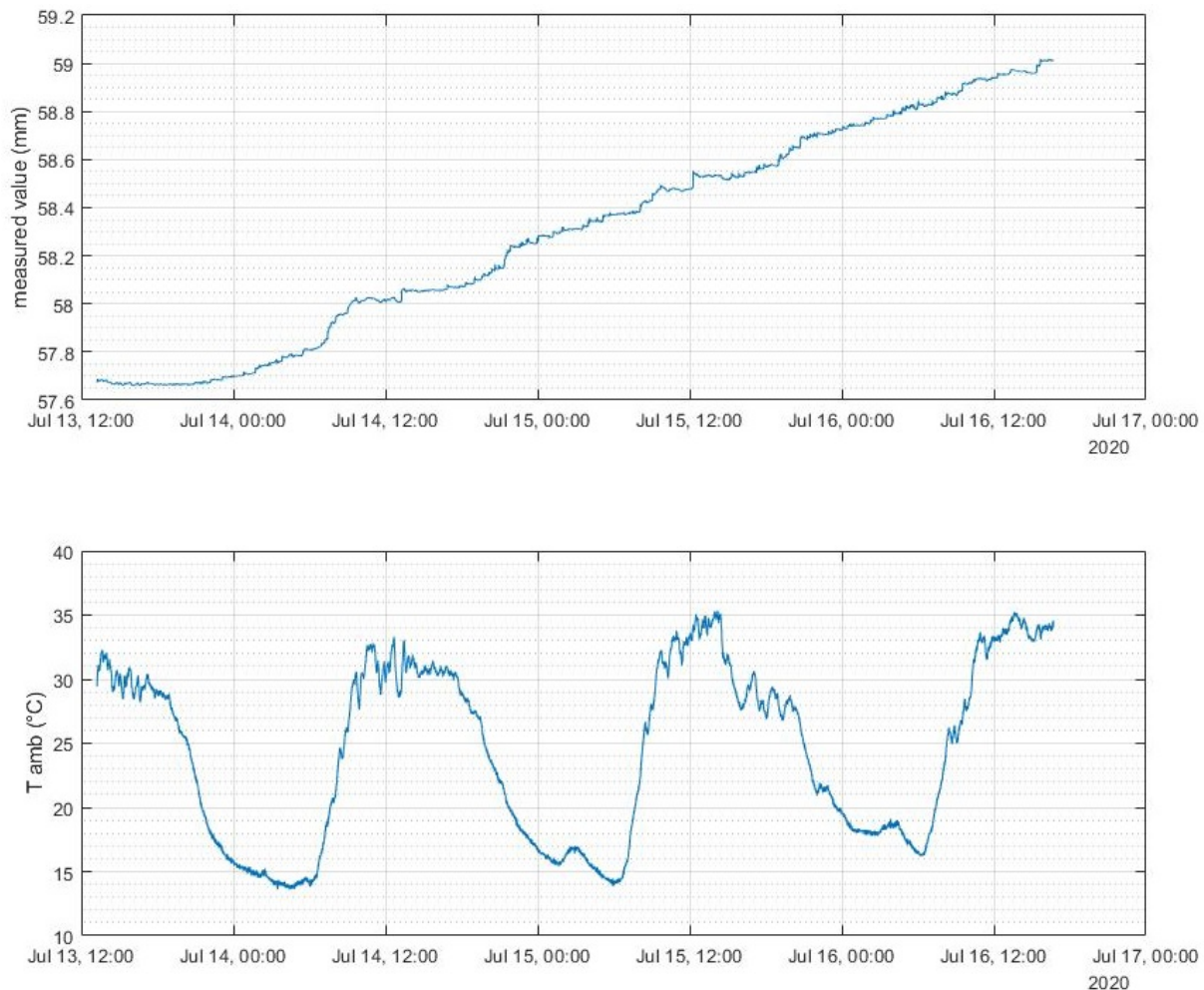


Figure 1.9: Data acquired compared with time and temperature perceived

The growth pattern recorded by the sensor is in line with what was expected, based on the apple growth physiology. In particular, at this phenological stage, apples grow almost linearly in time, with a slower growth during the warmer hours of the day, and accelerating in late-afternoon and through the night. The measured growth rate is also comparable to the typical one (about 0.6 mm/day).

In the following years (2021-2022) minor improvements has been adopted for the sensor node, such as solar Energy Harvester. A new case and solar cell are visible in Fig. 1.11. In Figure 1.10 the summer 2022 setup at the same orchard above mentioned, a setup commissioned by the Department of Agricultural and Food Science and Technology of the University of Bologna for their research purposes. In addition, the last year a test on citrus fruits has been performed (Fig. 1.12) too.



Figure 1.10: Summer 2022 experimental setup, four pliers.



Figure 1.11: Particular of the aggregator sensor node from 2022 setup.



Figure 1.12: Citrus fruit setup.

1.5 Conclusions

In this Chapter, the realisation of a sensor node prototype for continuous distributed monitoring of fruit growth was presented. Such activity can be considered as the starting point in my journey to investigate MCU based systems.

The developed low-cost prototype, implemented by means of commercial boards and 3D-printed devices, showed an adequately-high effective resolution with a full scale range suitable for no-manning operation. By adopting a multi-step calibration procedure it was possible to compensate for temperature dispersion, noise and non-linearity, which made the system rugged to environmental conditions and suitable for all-season operation. Thanks to the energy harvesting system and the possibility of data transmission in real-time over the air, the sensor-node and its sensing elements can be positioned at the beginning of the season and operate, without any maintenance required, until harvest time.

Future work will be devoted to the refinement and re-engineering of the pliers, so that they can better maintain the grip on the fruit, to prevent accidental falls or changes in position due to external agents, while preserving the non-invasiveness inherent to the approach. As anticipated in the introduction, electronic devices shortage did not allow the manufacturing of a single board devices. Nevertheless, the design of a custom board is planned, in order to integrate the harvesting stage, the MCU and the LoRa transceiver for performance and power consumption optimization.

Chapter 2

Bioengineering

Abstract

Bioengineering is a field where there is a high demand of intelligent smart systems, in particular, those based on wearable devices. These systems require a high level of integration combined with high computational performances. The requirement of a small form factor is common to a plurality of applications, because those devices should be comfortable, or mini-invasive. High processing performances are crucial to actuate real-time control system, or to perform data fusion combining multiple sensor acquisitions. So, despite being related to a different field, the bioengineering devices discussed in this Chapter share similar embedded system requirements w.r.t. the ones described in the previous Chapter. In particular, in this Chapter, three bioengineering research applications are reported, together with the related challenges and the solution adopted to face them.

Introduction

The first application addressed concerns the realization of a control system for a vascular phantom setup. A vascular phantom can be used as an in vitro test object to explore the blood flow behaviour in pathological conditions and novel ways of improving ultrasound diagnosis. This kind of phantom should be anatomically realistic both in terms of geometry, acoustic and physical properties. In particular, enhancing measurements reliability of in vitro models test requires the capability to realistically simulate the physiological flow. Such flow must mimic patient-specific conditions and should be performed by a reliable phantom set-up.

This Section describes the design of a programmable flow pump system, designed to be used in an in vitro experimental studies. This system wants to overcome the budget problem due mainly to expensive flowmeters. The proposed solution is based on the use of a low cost device, not able to perform a reliable closed loop control, but suitable to

obtain an ARX non-linear model of the hydraulic circuit thanks to Matlab tools. By using that model, it is possible to act an open loop control able to produce the targeted waveform with median deviation less than 9% and a similarity index of 0.98.

Here, we present also the flow rate calibration steps of the designed flow phantom setup. In the current work, the flow pump system has been developed using Carotid artery Phantom (CaP), but thanks of its programmability it is possible to implement different flow profiles.

The second bioengineering device discussed in the Thesis is designed for gait monitoring. In particular, it reports a novel m-Health approach, based on prototype instrumented crutches and a custom Android application, that can be used in either clinical or home environment. Crutches are sensorized with a 6-axis inertial measurement unit, a uniaxial load cell, and a WiFi data acquisition board for connectivity, as well as for data gathering and processing. Crutches kinematics and dynamics are calibrated with a motion capture system and a force platform. Data are transmitted via WiFi to an Android smartphone, where it is processed, visualized in real-time, and stored on the smartphone local memory for further off-line analysis. This thesis shows the prototype architecture and post-calibration accuracy for estimating crutch orientation (5° Root-Mean-Square Error - RMSE in dynamic conditions) and applied force (10 N RMSE). Future developments include the design of real-time biofeedback applications for motor rehabilitation and tele-rehabilitation.

Finally, the third bioengineering project concerns a wearable system. More specifically, an auscultation device. Chest auscultation is a crucial key point in clinical evaluation, thanks to the capability to rapidly collect complementary features such as heartbeat and breathing.

The purpose of this research is to realize a smart and compact system, to be used both as a wearable device for remote monitoring and as an aid for medical staff auscultation, overcoming the limitations of conventional stethoscopes.

Basically, we want to propose an advanced digital stethoscope which embeds digital processing for providing a second opinion diagnosis to the clinician aiming to minimize diagnostic errors. The device aims to become useful for telemedicine as well.

Moreover, the aim of this work is to present a selection of suitable sound transduction systems and analogue electronic processing. The focus on various microphone technologies, such as Micro Electro Mechanical System (MEMS), electret and piezoelectronic, aims to emphasise the most suitable transducer for auscultation. Tests are performed on a designed phantom setup and a qualitative comparison is reported with sounds recorded

with the developed device and two commercial digital stethoscopes.

For each Section 2.1, 2.2 and 2.3 contained in this chapter, one for each application introduced above, there is initially an introduction to the application, then the selection of electronic components and architecture, and finally a testing and validation phase. In addition, for each one there is a description of the on-board processing too.

The content of this Chapter is based upon the research work [P3, P4, P5]:

- “Design and Prototype Development of a Low-Cost Blood Flow Simulator for Vascular Phantoms” by Zauli M., Corsi C. and De Marchi L. in 2019 Computing in Cardiology (CinC), pp. 1–4. ©2019 IEEE.
- “mCrutch: a novel m-Health approach supporting continuity of care” by Arcobelli V. A., Zauli M., Galtieri G., Cristofolini L., Chiari L., Cappello A., De Marchi L. and Mellone S. in MDPI.
- “To make an Electronic Stethoscope it takes microphone: mic technologies comparison for auscultation device” by Zauli M., Peppi L. M., Di Bonaventura L., Arcobelli V. A., Alberto Spadotto, Igor Diemberger, Valerio Coppola, Mellone S. and De Marchi L. in MDPI. *To be submitted.*

From which part of the text is drawn. I have conducted autonomously the design and realization of the vascular phantom setup and the electronic boards in the other two projects. Moreover, I have realized the firmware of each systems, including on-board processing.

2.1 Vascular Phantoms Setup for ultrasonic investigation

A vascular phantom should be anatomically realistic both in terms of geometry, acoustic and physical properties to have good ultrasound measurements using equipment like echograph and eco-doppler [29]. The reliability of in vitro models can be enhanced by simulating the blood stream according to the characteristics of the vascular portion, reproducing a realistic physiological flow which mimics patient-specific conditions for in vitro experimental studies. Such studies are very important for improving ultrasound diagnosis, calibrating instruments and as educational support.

In this context, we propose a low-budget flow pump system to produce physiological-specific stream in flow phantoms. In particular, we focused on the development of a flow phantom setup for a carotid artery (CaPs - Carotid artery Phantoms). But, the system is programmable, so it is suitable for different flow phantoms thanks of its performances.

The CaPs used in the current work have been developed at the University of Bologna [30]. In particular, such phantoms are made by three main parts that simulate real vascular system: vessel, tissue around vessel and blood. Reproducing these parts it's possible thanks of three type of materials: Vessel Mimicking Material (VMM), Tissue Mimicking Material (TMM) and Blood Mimicking Fluid (BMF). It's possible to build CaP using two approaches: wall-less and walled. In the first one the vessel is obtained by realizing an empty channel in a TMM and a BMF is pumped trough the channel. This method enables the realization of complex geometries, but a wall-less phantom is prone to breakage due to BMF infiltrations in the TMM. Conversely, walled phantoms consist in tubular structures made of VMM, embedded in TMM and crossed by BMF. The CaP used to test the setup designed is a walled phantom built up with PVA-C as VMM, nylon-scatterer solution as BMF and water for TMM only to have coupling with the ultrasound probe.

The flow pump system is a fundamental component of a phantom setup. It is usually realized with expensive [31, 32] and bulky components to power a pulsatile flow rate into a vascular phantom. The cost and form factor may limit the use of such conventional system. In this work, a novel programmable flow pump is proposed to overcome these problems with compact and cheap sub-components. The main parts of this setup are two: i) the hydraulic circuit and ii) the control system. The hydraulic circuit has a liquid reservoir, one centrifugal pump, one ultrasound flow sensor and the CaPs. Each components has been chosen to suite the flow profile in carotid artery, but taking in account also other phantom types. The control system is powered by a microcontroller-based circuit board, which enables a flow loop which simulates either the full circulatory system, or a profile

measured locally. The control algorithm is based on an open-loop approach and on a Non-linear ARX model of the hydraulic circuit where fluid is pumped. Such model it's obtained during a calibration time of the system, this procedure has two phases: first of acquisition by embedded flowmeter and a second one of data elaboration by Matlab to generate a certain PWM vector useful to control the centrifugal pump.

2.1.1 Components and design

The designed flow phantom set-up is made by two parts: hydraulic circuit and control system. The set-up is shown schematically in Fig. 2.1, where it's possible to identify a flow loop (liquid reserve, centrifugal pump, flowmeter, carotid artery) and a control part (power supply, signal condition and MCU).

The choice of the components was performed taking in account a good balance between cost and performances. The target is to offer a low cost set-up, but with good performances (i.e. capable to simulate realistic physiological flows) and flexible (i.e. programmable for different phantoms).

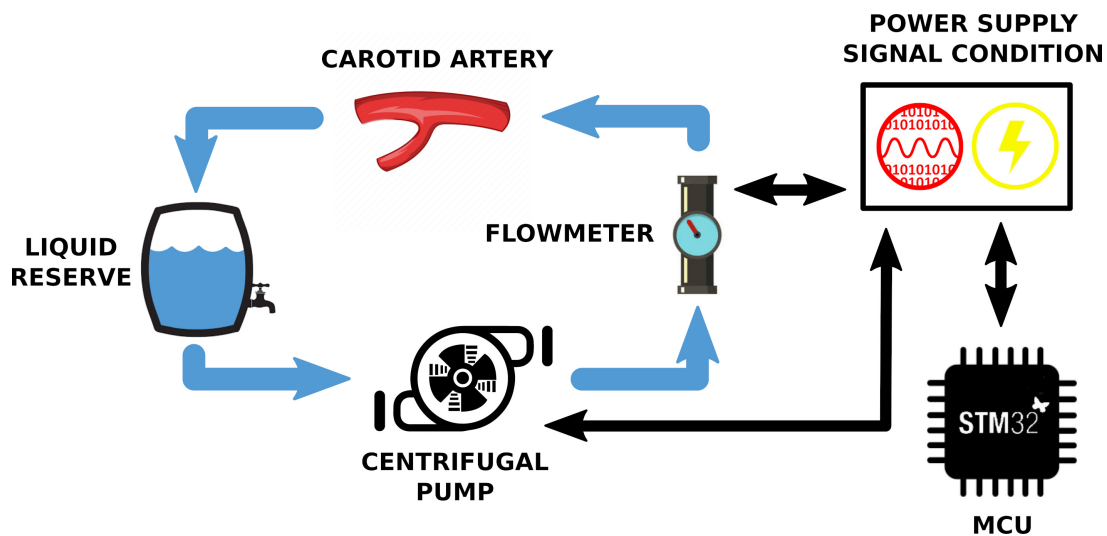


Figure 2.1: Designed flow phantom setup scheme. [©2019 IEEE]

2.1.2 Hydraulic circuit

The most relevant characteristics for a physiological waveform are maximum flow rate, minimum flow rate and highest value of first time derivative. The hydraulic circuit must adequately mimic these characteristics to simulate the pulsatile flow rate of real systems. In particular, the maximum flow rate and its dynamic characteristics have a strong influence in the pump selection which, in its turn, heavily impacts the design of the remaining system components. The hydraulic circuit consists of 4 main components interconnected

by a flexible silicon pipe. These devices are: liquid reservoir, centrifugal pump, flowmeter and the carotid artery phantom. Each component was carefully selected to perform the flow simulation: 1) liquid reservoir contains the liquid (BMF) pumped into flow loop. It has a capacity of around 3 litres; 2) the centrifugal pump is a TCS Micropumps M510S-180, chosen because of its maximum flow rate 8000 ml/min (free flow), robust high quality aluminium case and BLDC motor connection (no integrated controller); 3) flowmeter is a low cost ultrasonic transducer by Cynergy3 (model UF08B100). Such transducer has a measurement range from 0.4 ml/min to 8000 ml/min, maximum precision of 3% of reading, response time better than 0.1 seconds and an ABS plastic case. Finally, 4) the CaP is the one described in [30].

2.1.3 Control system

The flow control sub-system is constituted by three circuit boards: one for power supply and signal conditioning, a BLDC motor controller board and a microcontroller based circuit board.

The microcontroller board is a discovery board by ST Microelectronics (STM32F746G-Discovery). This board was chosen because it features the STM32F746NGH6, a high performances MCU. The Discovery board has a 4.3-inch 480x272 color LCD-TFT with capacitive touch screen which enables the implementation of a user-friendly interface to operate the flow phantom set-up. Moreover this ST development board has been chosen for its easy connections to microcontroller's GPIO.

The BLDC motor controller board is an EQi-V2 provided by the same manufacturer of the pump, TCS Micropumps. It supports a power supply from 12 V up to 30 V and requires a 0-5 V signal to produce various flow rates. An additional feature, not exploited in the current work, is the possibility to reverse flow rate through a control pin and RPM measurement by a pulse output pin.

The power supply and signal conditioning board is a circuit which generates multiple reference voltages, for the different needs of system devices, and interfaces some components. In particular, it interfaces the pump and the flowmeter to enable PWM control of the pump and acquisition reading from ultrasonic flowmeter, by applying the suitable voltage level shifts to the MCU's GPIOs.

Therefore, the power supply and signal condition board acts as a bridge between the STM32F7-Discovery board and the flow sensor as well as the pump. The Discovery board controls flow rate using PWM signal applied to the EQi-V2 motor controller which drives the centrifugal pump. Conversely, the flow sensor gives a PWM output whose frequency is proportional to the flow rate reading.

2.1.4 Design

The flow loop control is an open-loop control which needs a suitable calibration procedure. In this work, the initial calibration is performed using a closed-loop control, whose aim is to iteratively select the control sequence which outputs the desired flow values at specific time samples. The closed-loop control is shown schematically in Fig. 2.2. Unfortunately the feedback provided by the flowmeter has a low (and irregular) sample rate (see Fig. 2.3 green track), this means that the flowmeter output is not able to reproduce high flow dynamic, like carotid artery profile. Therefore, the closed-loop control is used only to perform a rough comparison between the desired flow (described by the two programmed vectors) and real one (measured by flowmeter). Despite these limitations, the results of such comparison can be fed to the Matlab tool System Identification in order to build the hydraulic circuit model. In particular, an ARX non-linear model was used in this work.

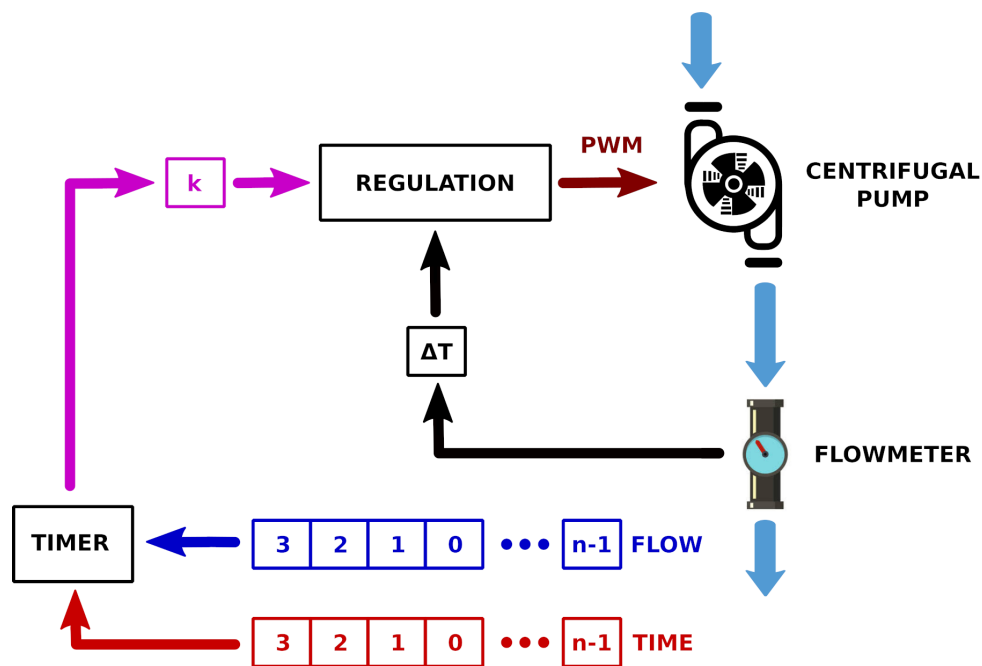


Figure 2.2: Closed-loop control. [©2019 IEEE]

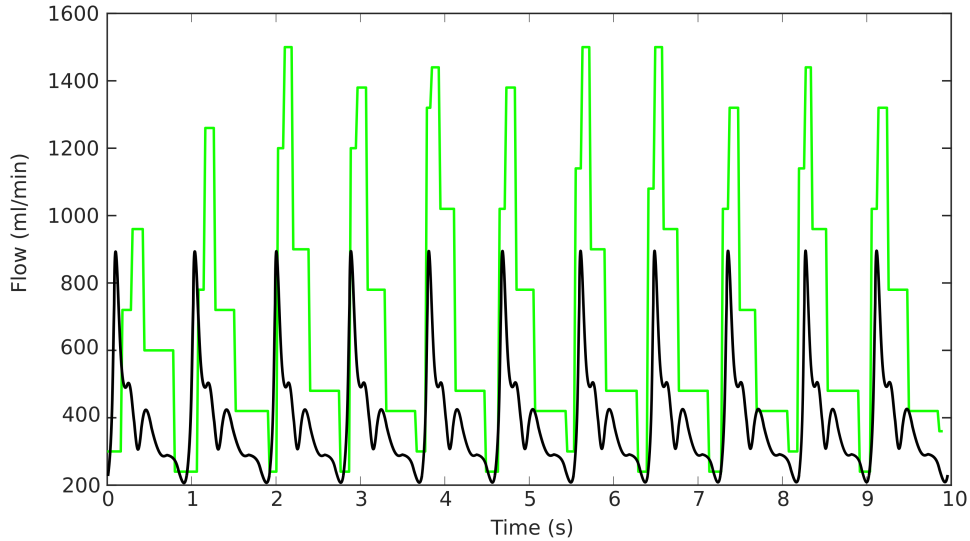


Figure 2.3: Target flow black track, flowmeter acquisitions green track. [©2019 IEEE]

The ARX model allows to calculate an appropriate PWM motor controller board input vector to have the desired output flow rate. This vector is programmed in the open-loop control mode (open-loop algorithm shown in Fig. 2.4) and it enables the flow simulation.

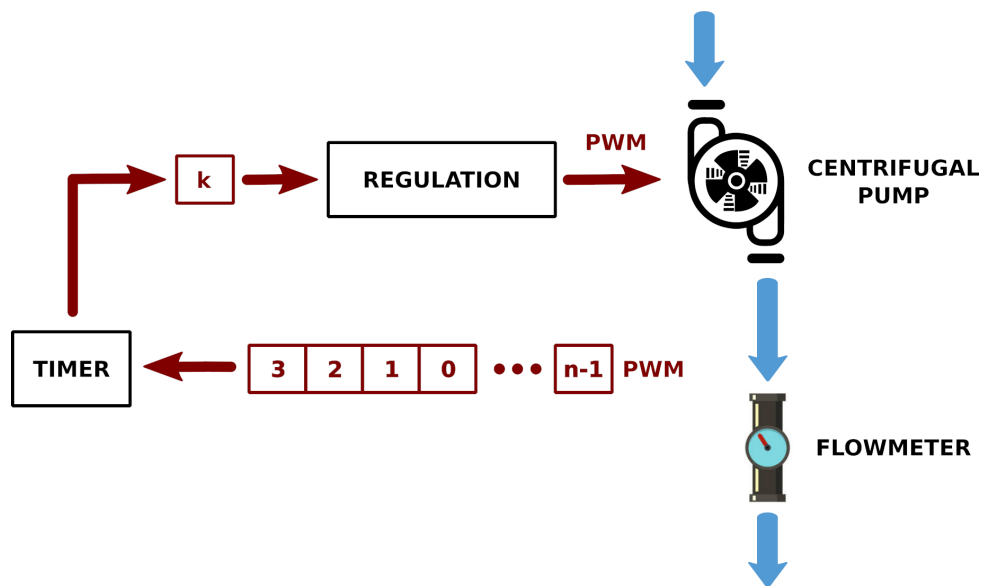


Figure 2.4: Open-loop control. [©2019 IEEE]

This method, closed-loop calibration and open-loop flow generation, allows to overcome the necessity of a high-cost high-sample rate flow sensor. Moreover, in designing the final device, a special care was devoted to dimensions and usability. A compact case was developed to host the electronics boards and hydraulic components, including a liquid reservoir of 3 litres. The flow simulator case has inlet and outlet silicon pipes to connect

the vessel phantom (Fig. 2.5 (a)). In Fig. 2.5 (b), it is possible to see the flow phantom set-up connected to a CaP placed in a white case adapter.

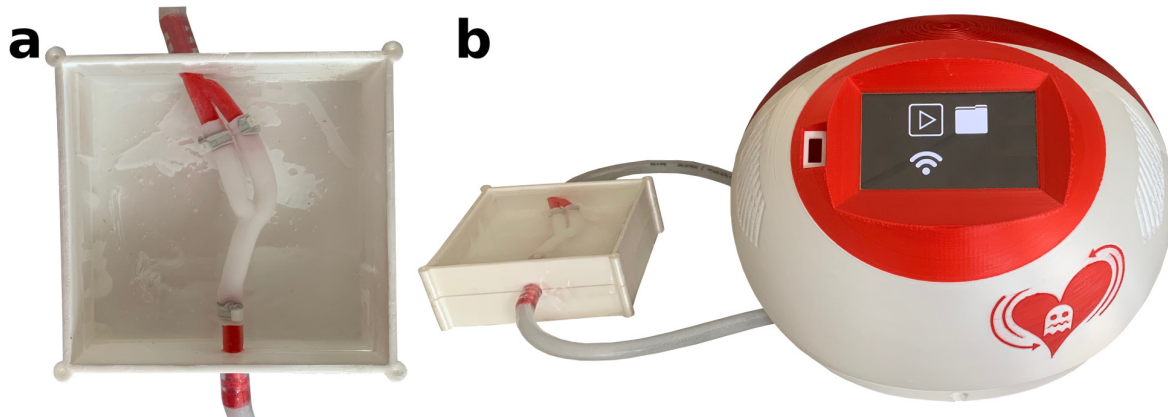


Figure 2.5: (a) Vascular Phantom (b) Flow Simulator Prototype. [©2019 IEEE]

2.1.5 Tests and performance evaluation

In order to evaluate the performances of the designed flow phantom set-up, since the vascular phantom under studies is meant to be used for ultrasonic acquisitions, it was used an eco-doppler machine. Using this device, it is possible to evaluate the waveform generation with respect to the targeted one. In Fig. 2.6, the yellow track illustrates the target flow profile (i.e. a typical carotid artery profile) and the two black tracks are the measurements of the actual flow acquired with a magnetic flowmeter (upper curve) and with the ecodoppler machine (lower one), respectively.

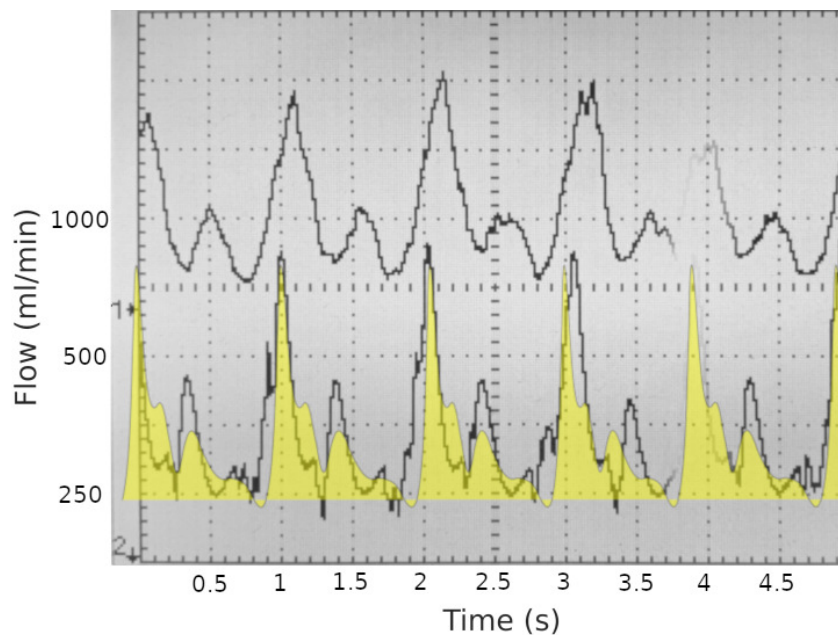


Figure 2.6: Magnetic flowmeter and eco-doppler acquisitions. [©2019 IEEE]

In Table 2.1, target values of the carotid flow profile analysed are collected and compared with eco-doppler measurements of flow rate generated by the programmable flow set-up designed. In these acquisitions, the maximum deviation of the simulated flux with respect to the target value is equal to 40% at the diastole peak (610 ml/min instead of 430 ml/min). Apart from this isolated case, the median deviation is less than 9% and the similarity index (SI) is 0.98. The similarity index formula is shown below, where φ_t and φ_m are respectively target values vector and measured values vector from Table 2.1.

$$SI(\varphi_t, \varphi_m) = \frac{|\varphi_t^t \varphi_m|^2}{(\varphi_t^t \varphi_t)(\varphi_m^t \varphi_m)}$$

Since SI is close to one, the agreement between target values and measured values can be considered very good.

Table 2.1: Samples each 45 ms, comparison between carotid flow profile target value and measured value by ecodoppler.

Sample	Target value	Measured value
1	250	300
2	360	390
3	710	700
4	875	850
5	660	640
6	520	510
7	500	480
8	480	450
9	395	360
10	325	290
11	395	520
12	430	610
13	420	520
14	380	450
15	340	380
16	320	360
17	305	300
18	300	280
19	300	260
20	295	250

2.2 Smart Crutch

Gait, or the act of walking, is a fundamental human function. When an individual's ability to walk is compromised due to an impairment or injury, rehabilitation efforts often prioritize the restoration of this ability [33]. Approximately 10% of adults experience limitations in their mobility or balance as a result of conditions affecting the Central Nervous System (CNS). Gait impairments are the result of a variety of medical conditions, including lesions of the central and peripheral nervous systems. Walking aids are frequently prescribed to enhance mobility and balance [34], and are also prescribed for neurological patients [35]. Other common medical conditions are osteoarthritis, multiple sclerosis, fractures, muscle lesions, and stroke [36]. Gait impairments have a significant impact on patients' quality of life [37], and walking aids play a major role in increasing their daily mobility and independence [6]. Crutches are the most common assistive devices for individuals with mobility impairment [38]. As the number of individuals with mobility impairments increases with the longer life expectancy, it is likely that the use of assistive devices, such as crutches, will also increase over time [39, 40].

Whenever possible, the use of crutches in place of wheelchairs is often preferred by clinicians because they promote a patient's participation, allow them to keep an upright posture with related physiological benefits, and improve their independence in daily living activities. These factors can lead to better long-term recovery outcomes. In addition, crutches may be a more practical and convenient option for individuals who only require short-term or intermittent mobility assistance [41, 42].

From a biomechanical point of view, crutches increase an individual's base of support while walking. They also allow patients to transfer part of their body weight from their lower to upper limbs while walking or standing [43].

There are three main types of crutches, as illustrated in Fig. 2.7: axillary (or underarm) crutches, forearm (or elbow/Canadian/lofstrand) crutches, and gutter crutches. Each type has its own unique characteristics and may be suitable for certain individuals depending on their specific needs.

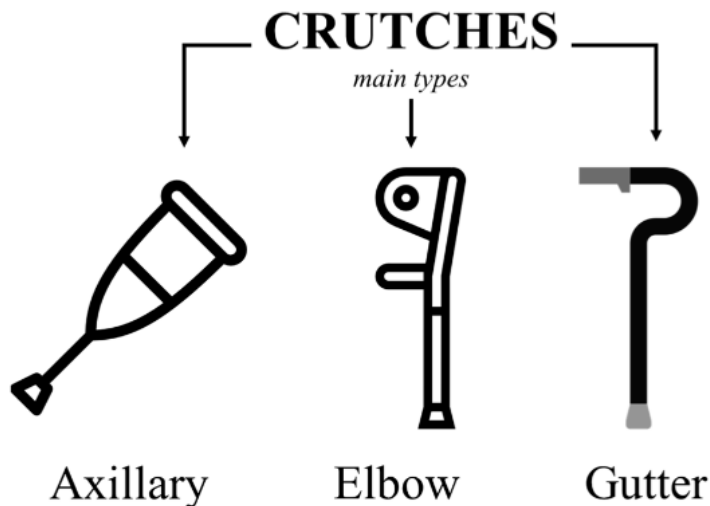


Figure 2.7: Main types of crutches.

Several different walking patterns that can be adopted when using crutches. These include the two-point crutch gait, where the crutches and the affected limb move forward as one unit while the uninvolved weight-bearing limb is carried forward on the crutches as a second unit. Another pattern is the two-point gait, where the crutches and the uninvolved limb are moved forward in alternating steps. The four-point gait involves moving the crutches and the uninvolved limb forward in a coordinated manner. Finally, in the step-to-gait pattern, the affected limb moves forward, followed by the non-affected limb, while the step-through gait pattern shows the opposite sequence [38, 44, 45, 46, 47].

Crutches are frequently used in motor rehabilitation to aid in the recovery from diseases that affect the lower limbs [37, 48, 38]. However, during rehabilitation sessions, therapists often do not have tools for a quantitative assessment of patients' progress and usually rely on visual observation and clinical scales that cannot capture relatively small changes [49, 50]. This can lead to incorrect share of weight between the crutches or incorrect crutch position while walking or standing, especially in unsupervised settings. Sensorized crutches, embedding sensors, processing capabilities, and connectivity options can address the need for real-time and long-term monitoring of crutches usage, providing therapists with more accurate and quantitative information on patients' recovery [51].

Sensorized crutches, or instrumented crutches, are assistive devices developed to support the mobility of patients during rehabilitation. These crutches are equipped with sensors that measure various physical parameters related to gait, such as force, acceleration, and pitch angle. The data collected by the sensors are used to provide feedback to both the patient and the therapist, allowing for a more accurate assessment of the patient's progress and guiding treatment decisions. The use of sensorized crutches has shown promise in improving patient outcomes and facilitating telerehabilitation. The

current state of the art in the field of sensorized crutches includes a range of designs and features, including gait analysis which has the potential to transform the way crutches are used in rehabilitation [52, 53, 54, 55, 56]. However, there is a lack of applications for sensorized crutches in a standalone modality in the current state of the art for outdoor and long-term monitoring. The aim of this work is to study a system to fill that gap. In addition, further research is needed to fully understand the potential benefits of this technology, particularly for which locomotion pathologies it may be most suitable.

2.2.1 Motivations

The growth of wearable technologies has led to a proliferation of smart devices in various fields, including healthcare. The World Health Organization (WHO) defines “mHealth” as “the use of mobile devices, such as mobile phones, patient monitoring devices, Personal Digital Assistants (PDAs), and other wireless devices, for medical and public health practice” [57]. To our knowledge, there are no applications of sensorized crutches for long-term monitoring of patients with motor impairments. We believe that a mobile health application based on a set of instrumented crutches could be a valid support to continuity of care scenarios for multiple reasons:

1. Instrumented crutches can provide continuous, real-time monitoring of the patient’s mobility and gait pattern, enabling the objectification of the rate of progression of the rehabilitation for each individual patient..
2. Instrumented crutches can collect and transmit data to smartphones or other mobile devices. The computational capacity of modern devices enables real-time applications/feedback and advanced reporting functions for both therapists and patients.
3. Instrumented crutches in a mHealth scenario can improve the communication between the patient and the therapist, enabling remote monitoring and teleconsultation. Telerehabilitation applications can be important for patients living in underserved or remote areas. They would improve access to rehabilitation services and reduce the healthcare system’s burden.
4. Through smart biofeedback applications and personalised reporting functions, instrumented crutches can empower patients and allow them to take a more active role in their rehabilitation program.

The COVID-19 pandemic highlighted the need for more efficient, accessible, and pervasive healthcare approaches, such as intelligent systems and mHealth technologies [58,

59, 60, 61]. The use of sensorized crutches in a mHealth scenario supporting the continuity of care may also help reduce healthcare costs [62]. However, despite the variety of applications and prototypes reported in the literature, there is still the need to assess the potential impact of instrumented crutches in the continuity of care applications, from real-time guidance in rehabilitation facilities to long-term remote monitoring outdoors and at home.

The aims of our study are as follows:

1. To develop a set of instrumented crutches suitable for mobile health applications. Expected outcomes are orientation angles and applied loads;
2. To develop a smartphone app, mCrutch, for the management of the instrumented crutches and for enabling real-time applications;
3. Verify the accuracy of the estimate for the orientation angles and the applied loads;
4. To keep manufacturing costs in line with those of mass-market technologies.

2.2.2 Materials and Methods

A pair of Lofstrand (or Canadian) crutches was instrumented to measure axial force and orientation with a dedicated Android application for process, visualizing and storing real-time data coming from mCrutch (Fig. 2.8). All of the electronics were contained inside the crutch's original structure.

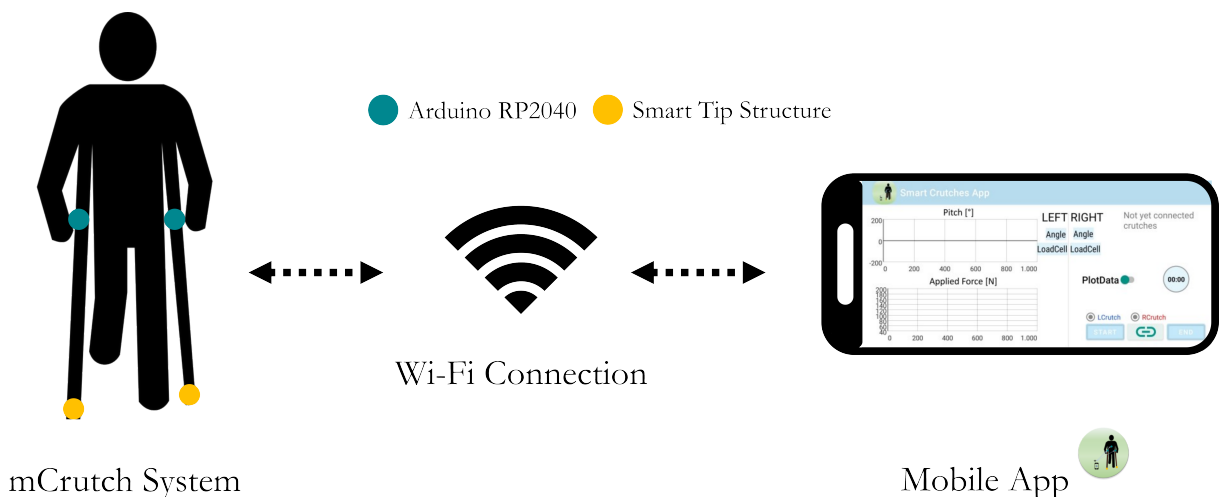


Figure 2.8: System Overview: mCrutches and Mobile App.

Each crutch embeds an Arduino RP2040 equipped with a 6-axis Inertial Measurements Unit (IMU). The Arduino is also connected to a uniaxial load cell placed at the tip of the crutch inside a custom mechanical structure.

Figure 2.9 shows the crutch prototype and lists the different components.

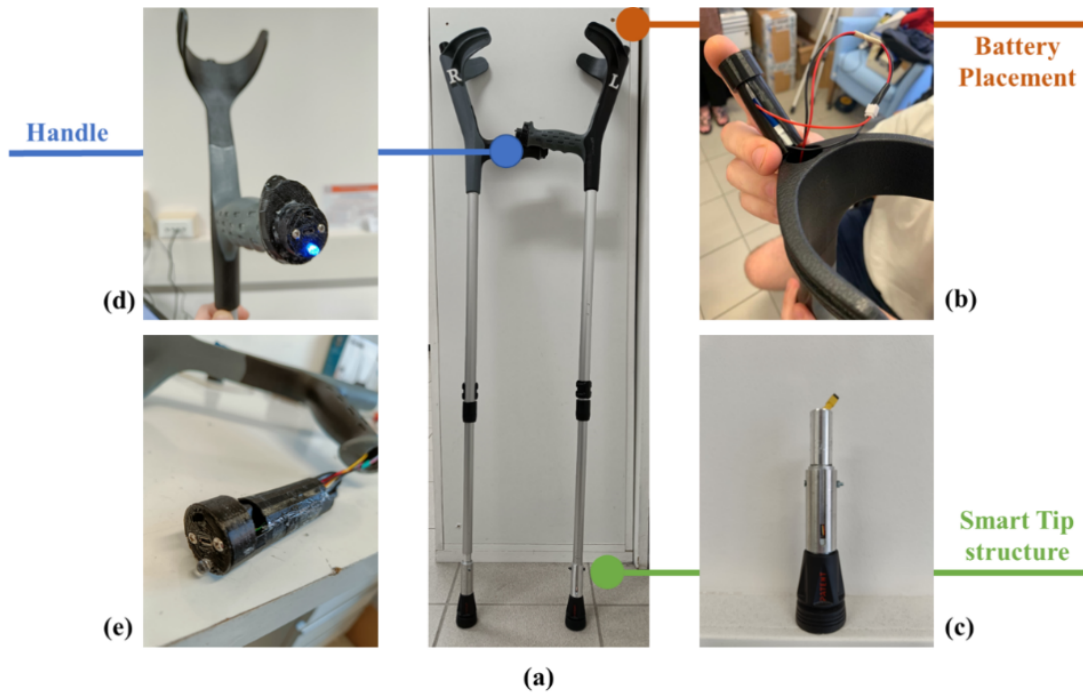


Figure 2.9: mCrutch assembly: (a) mCrutch final prototype; (b) battery placement; (c) Tip modified mechanical structure embedding the miniaturized load cell (d) plastic protective case containing the electronics and (e) handle's front panel with the status led, the power button, and the USB port for battery charging.

Electronic components

Most of the electronics were inserted in the crutch's handle cavity, approximately 84 mm deep, with a 28 mm diameter. The handle cavity communicates with the crutch's vertical shaft and the forearm cuff (Fig. 2.9), enabling the run of wires inside the crutch structure. In Figure 2.10 shows all the electronic components: the main boards (U2) and the power management board (U3). U2 in Figure 4 is an Arduino Nano RP2040 Connect, selected for its small form factor (18 x 45 mm) that can fit the housing in the crutch's handle; the Arduino board collects data from the embedded IMU, and the load cell and manages the WiFi connection with the Android App. The main board hosts a Raspberry Pi RP2040 MCU, a U-blox Nina W102, an STMicroelectronics LSM6DSOX 6-axis IMU with an on-chip temperature sensor and an MP34DT05 microphone. U3 in Figure 4 is the power management board. It features an MCP73832 single-cell charger, and it is connected to a Lithium-Ion (Li-Ion) battery (U1).

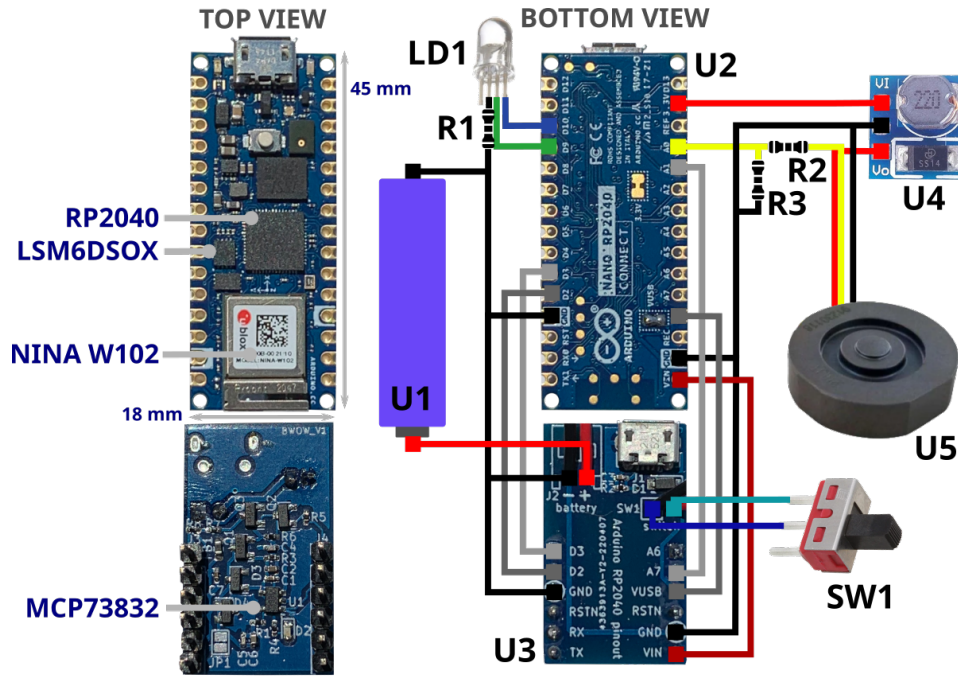


Figure 2.10: Diagram of electronic connections.

With reference to Figure 2.10, the full list of components is provided below:

- U1 – Power supply: Li-Ion battery RS-ICR14500 [63], 3.7 V at 820 mAh;
- U2 – Processing, data acquisition and wireless communication management: Raspberry Pi RP2040 MCU [64], a dual core 32-bit ARM Cortex operating at a frequency of up to 133 MHz, 264 KB on-chip SRAM, up to 16 MB off-chip Flash and various digital and analog peripherals (SPI, I2C, UART, ADC, etc.);
- U2 – Wireless communication: U-blox Nina W102 [ds], Bluetooth V4.2 and WiFi 802.11b/g/n module;
- U2 – IMU: LSM6DSOX [65], STMicroelectronics MEMS sensor, which embeds a three-axial accelerometer and three-axial gyroscope (6-axis IMU) with a full-scale acceleration range up to ± 16 g and a maximum angular rate of ± 2000 dps. It is used to measure linear acceleration and angular velocity of the crutch for estimating its orientation;
- U3 – Li-Ion on-board battery charger: MCP73832 [66], Microchip 500 mA linear charger management controller for single cell Li-Ion/Li-Polymer battery;
- U4 – Voltage Converter: ANGEEK DC-DC Step-Up, 0.9-5 V to 5 V, operating frequency 150 KHz, conversion efficiency 85 %. It boosts Arduino 3.3 V output to 5 V to power the load cell (U5);

- U5 – Load cell: uniaxial load cell FX293X-100A-0100-L [67], analog output (0.5-4.5 V) by TE Connectivity, with a Full-Scale range of 500 N, a precision of $\pm 0.25\%$ FS and a round shape (diameter 19.7 mm, height 5.45 mm) used to measure axial force applied on the crutch tip;
- SW1 – Slide switch, to power ON/OFF the device;
- LD1 – RGB LED, it signals the system status (green power on, blue connected to the host device - smartphone);
- R1 – Limits the current to LD1;
- R2, R3 – Level shifter to adapt 0.5-4.5 V load cell output to RP2040 MCU ADC channel 0-3.3 V;

Data collection from LSM6DSOX IMU was performed at 204 Hz with a ± 4 g range for the accelerometer and at 208 Hz with a ± 2000 dps range for the gyroscope. The orientation of the device is estimated with a sensor fusion approach based on Madgwick Filter [68]. The choice of a high-performance MCU, such as the one on Arduino RP2040 Connect, provides a smooth data fusion with a high data rate of up to 100 Hz. The same rate was used to sample the output of the load cell, using one RP2040 ADC channel. Force signal were digitally filtered with an 8-point window moving average filter. Orientation and force data were transmitted to the smartphone via a WiFi protocol through the U-blox Nina W102 module. Therefore, the system sends in real-time, every 10 milliseconds (100 Hz), a frame consisting of the values of the triaxial accelerometer, the triaxial gyroscope, the estimated orientation angles, the applied load, the battery charge level, and the timestamp. The manufacturing cost for the current prototype version is around 100 per crutch.

Smart Crutches App

The mCrutches system was designed to be connected to a host device running an Android operating system (a SAMSUNG Galaxy A50 in this study). The mCrutches App was developed on Android Studio 2021.3.1 (Dolphin). This application is responsible for collecting, storing, and visualizing data for debugging purposes. Currently, the interface design of the Smart Crutches App is of a low level, intended for use by researchers.

The Smart Crutches App enables the concurrent or individual connection of each crutch and allows for the control of mCrutch operations through the manipulation of buttons on the basic interface, as depicted in Figure 2.12.

The Android operating system supports the creation of a hotspot WiFi, and the connection between the mCrutch and the host device is established through the use of socket

communication, with the Smart Crutches App serving as the server and the mCrutch functioning as the client.

The data transmitted from the mCrutches includes heading and applied weight, as previously described in the introduction. In addition to these parameters, the packet message also includes information such as the timestamp, the battery level (expressed as a percentage from 0-100%), battery status (either charging or not charging), and the status of the crutches (including any errors detected by the accelerometer, gyroscope, or orientation estimation).

The sampling frequency is set to 100 Hz, which is fast enough for most motion analysis applications. To verify data loss, a function on the smartphone App compares the current timestamp with the previous one. If there is any gap in the data, a message is sent to the user through the display of a string on the user interface panel, and a 1s vibration is activated too. This allows the user to be aware of the data loss. The mCrutch system architecture, along with flowcharts for each single layer, is reported in Figure 2.11.

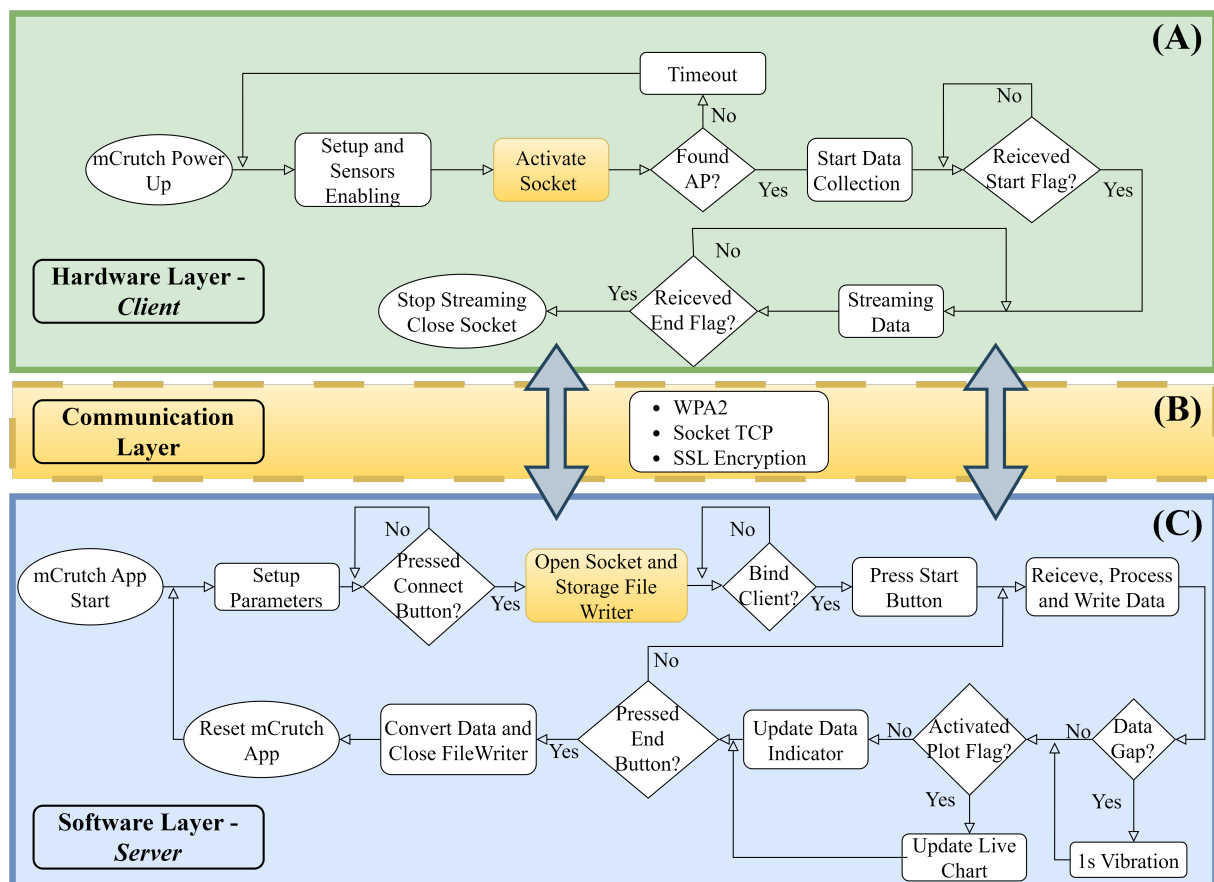


Figure 2.11: Layers of the mCrutch system architecture. The figure shows the flowcharts of the Arduino/data collection layer (A), the communication layer (B), and the mCrutch app layer (C).

The interface of the mCrutch App includes a control panel (Fig. 2.12.1) with a “Con-

nect” button in the center, which allows the user to initiate the connection with the crutches. Once the connection is established, the indicators for the left and right crutch will turn green, indicating that the connection has been successfully established. The user can start the data stream by pressing the “Start” button, while a chronometer (Fig. 2.12.3) shows the elapsed time (Fig. 2.12.2). Data is transmitted from the crutches and displayed in the “Data Indicators” box (Fig. 2.12.4). The user has the option to activate a real-time chart by switching on the “PlotData” flag (Fig. 2.12.5). The box displays the pitch angle in degrees [°] and the applied force in Newtons [N]. The user can stop the data stream by pressing the “End” button. Collected data is stored in the internal memory of the smartphone and can be accessed by the user for offline analysis.

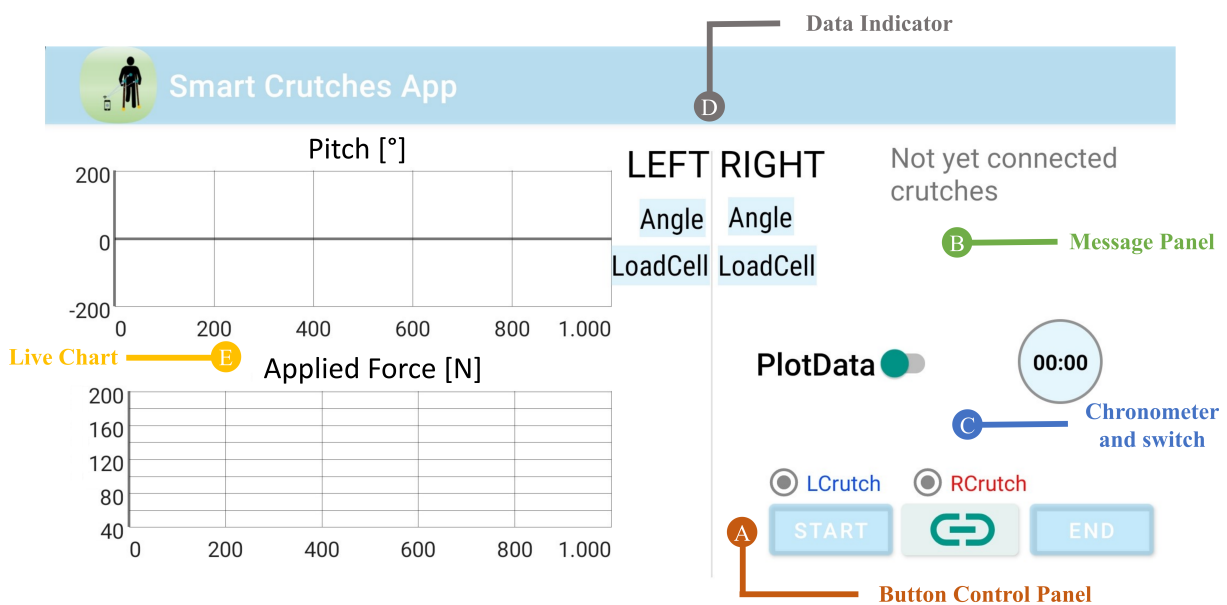


Figure 2.12: Smart Crutches app layout and descriptors: (A) button control panel; (B) message panel from system or mCrutch; (C) chronometer and switch for a real-time plot; (D) data indicator for both pitch [°] and applied force [N]; (E) live-chart of pitch [°] in upper graph and applied force [N] in the lower graph.

2.2.3 Calibration

Calibration is an essential step in analyzing kinematics and dynamics quantities. It is crucial to calibrate custom devices that include transducers embedded within a mechanical structure, as the structure itself may alter the physical characteristics or positioning of the transducers in a way that deviates from the manufacturer’s recommendations. For example, a 6-axis IMU embedded in an Arduino system refers to an internal local reference frame that may not correspond to the reference frame of the device. The calibration converts the measurements from the internal local reference frame of the sensor to the

desired reference frame on the device. A movement analysis laboratory was used to calibrate the instrumented crutches. The laboratory was equipped with four Kistler force platforms and a BTS Motion Capture SMART-DX EVOs system [69], systems that can be considered the gold standard for movement analysis. The crutches have a sampling frequency of 100 Hz, while the force platforms and the Motion Capture system have a sampling frequency of 1000 Hz and 250 Hz, respectively. Figure 2.13 illustrates the setup that was used during the calibration procedure. Cameras were used to capture the movement of the instrumented crutches through four optical reflective markers fixed on the crutch. During the calibration, a random sequence of movements and applied loads were produced in order to capture a wide range of orientation and force values.

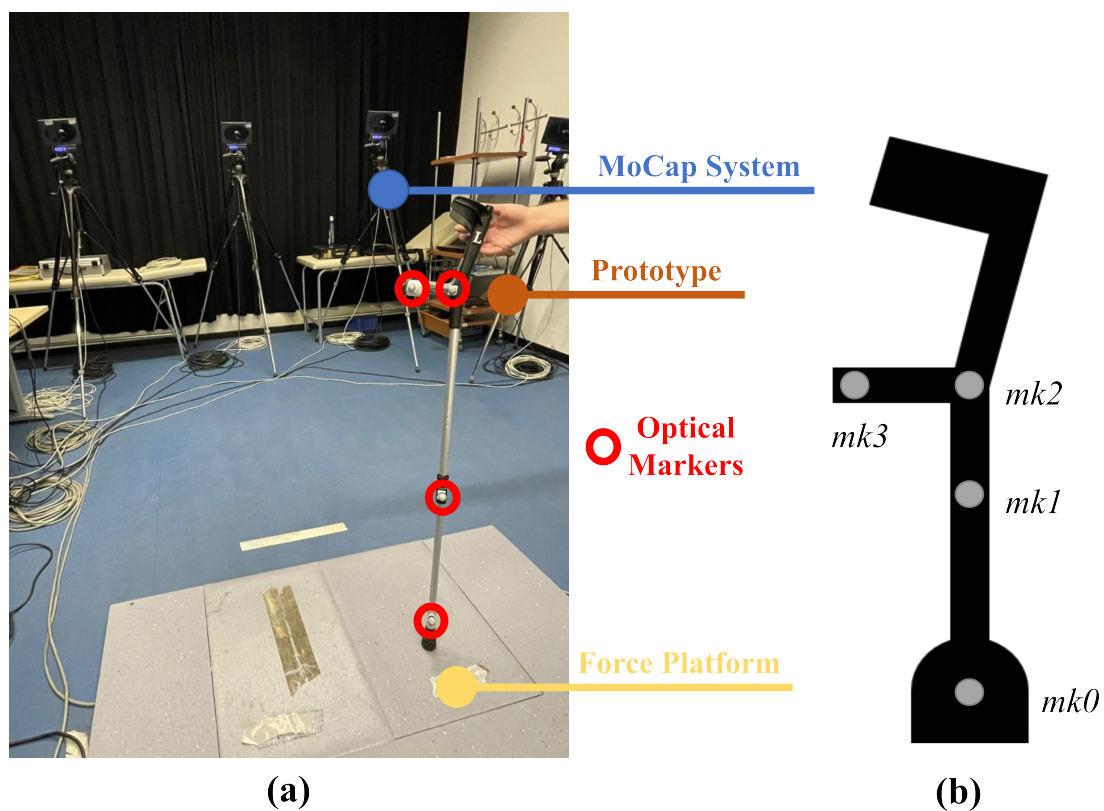


Figure 2.13: Calibration setup: laboratory environment (a) and marker positioning (b).

Data from the motion capture system and the instrumented crutches were imported in MATLAB (R2022b) for offline analysis. Camera data were down-sampled and synchronized with the IMU signals. As shown in Figure 2.13, a cluster of markers was used, where: marker *mk0* was placed on the tip, marker *mk1* was placed on the shaft, marker *mk2* was placed at the intersection between the handle and shaft, and marker *mk3* was placed at the end of the handle. A cluster of four markers has been used for two reasons: (i) in future validations with end-users, guidelines for full body kinematics would require a cluster of four markers on each body segment and each crutch [70]; and (ii) the

diameter of the handle is approximately 2 cm wider than the diameter of the shaft; hence, two markers on the shaft and two markers on the handle would provide a more accurate representation of the vertical and anterior–posterior axis of the crutch. Markers' trajectories were low-pass filtered with a zero-phase 6th-order Butterworth filter with a cut-off frequency of 5 Hz. A local reference frame was defined on the crutch aligning the axis with the shaft and the handle of the crutch. With reference to Figure 2.14, we derived a rotation matrix gR_l and a translation vector gT between the laboratory reference frame, defined by means of the markers placed on the crutch, and the mCrutch reference frame of the embedded IMU. Given the rotation matrices R_g of the crutch in the laboratory reference frame and R_l the rotation matrix of the mCrutch (embedded IMU) reference frame, we match the origins of the reference systems to their centroids, and we calculate R_T as reported in Equation (2.1).

$$R_T = R_g R_l^T \quad (2.1)$$

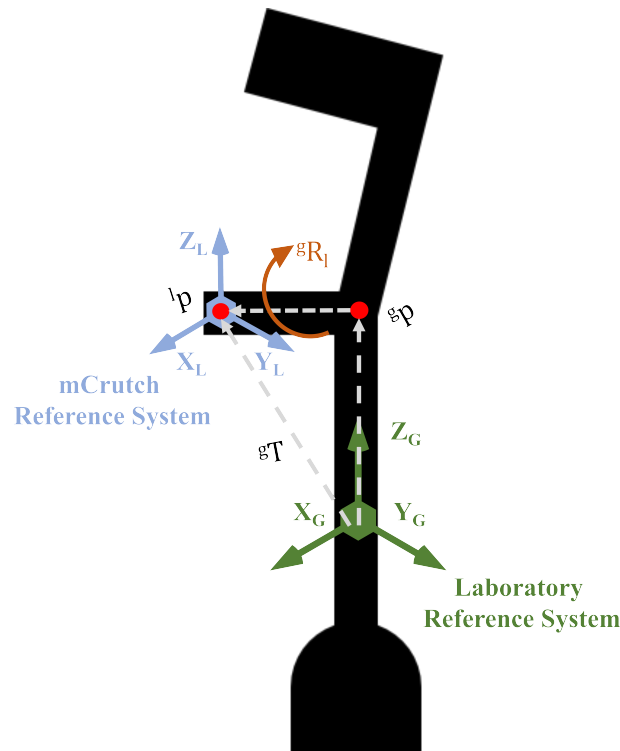


Figure 2.14: Relationship between the mCrutch reference frame and the laboratory reference frame.

The Singular Value Decomposition (SVD) method [71] is applied to R_T as shown in Equation (2.2).

$$[U, D, V] = svd(R_T) \quad (2.2)$$

Outcomes of the SVD, namely U , S , and D , which are, respectively, the left singular vectors, the singular values, and the right singular vectors of the homogeneous transformation matrix T , are used to calculate the rotation matrix gR_l as shown in Equation (2.3).

$${}^gR_l = U \begin{bmatrix} 1 & 0 & 0 \\ 0 & 1 & 0 \\ 0 & 0 & \det(UV^T) \end{bmatrix} V^T \quad (2.3)$$

The latter was also used in Equation (2.4) for calculating the translation vector gT , where G_m and L_m correspond to the centroids of R_g and R_l , respectively.

$${}^gT = G_m - {}^gR_l L_m \quad (2.4)$$

Finally, in Equation (2.5), R_{gl} and gT are applied to R_l , to obtain the calibrated rotation matrix, R_c , which is then converted to Euler angles.

$$R_c = {}^gR_l R_l + {}^gT \quad (2.5)$$

The uniaxial load cell in the smart tip requires calibration too. Data obtained from the force platform are used as the gold standard. The load cell calibration is expressed in Equation (2.6).

$$\hat{F} = k \cdot F + F_0 \quad (2.6)$$

where:

- \hat{F} is the calibrated value of the force measurement;
- F is the measured value from smart tip;
- F_0 is the offset compensation factor;
- k is the gain factor.

2.2.4 Results

This study aimed to describe the mCrutch prototype architecture and report on the accuracy of orientation angles and applied force. From an aesthetic point of view, aside from the status LED and the power button, the instrumented crutches are equivalent to any simple pair of Lofstrand crutches. mCrutch can stream data at a sampling frequency of 100 Hz and the WiFi connectivity with TCP protocol ensures data retransmission. Under normal usage, the mCrutch app requires only 5% of the total CPU usage and

approximately 78 MB of memory, with light energy consumption as defined in Android Studio Profiler. This ensures that the app runs smoothly without causing any significant drain on the smartphone’s resources or battery life. Concerning Arduino’s computational time and complexity, sensor reading is not computationally expensive, unlike onboard orientation extraction. This feature requires a high-performance MCU, in particular for a data rate such as 100 Hz. RP2040 has the required computational capacity, thanks to its computational power enabled by a Dual-Core Arm Cortex-M0+ operating at a frequency up to 133 MHz.

Preliminary results indicate that the mCrutch system can provide accurate measurements for both pitch and roll angles and applied force. Figure 2.15 illustrates an example of force recorded for both the left and right crutch during the calibration procedure. A random sequence of movements and applied loads, in the range of $\pm 50^\circ$ and 0–400 N, respectively, were performed for approximately 120 s of recording while the crutches were placed on the force platform (FP).

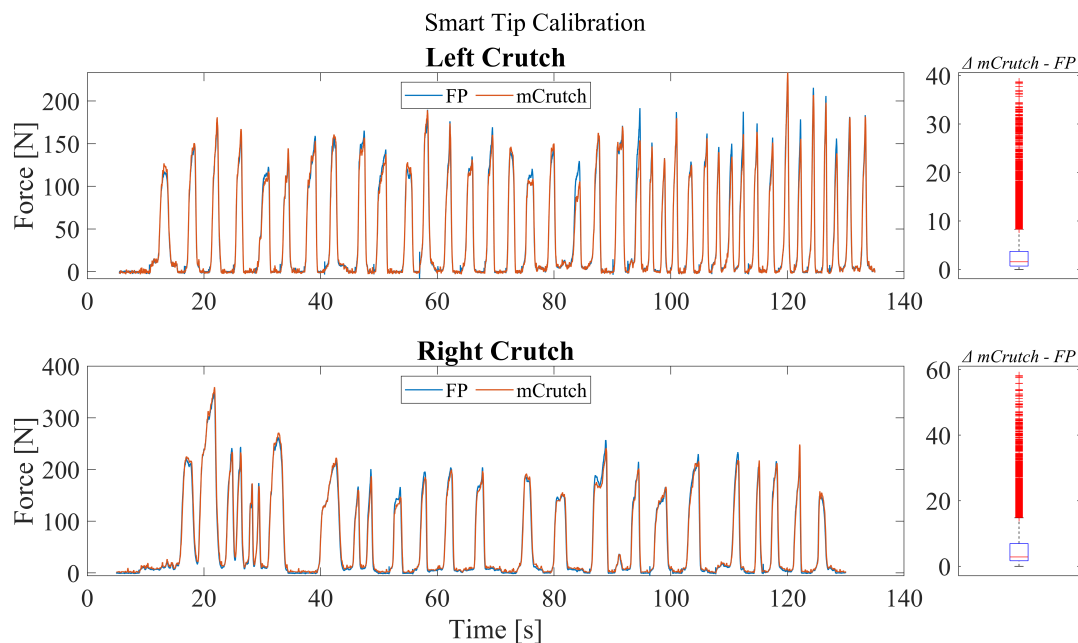


Figure 2.15: Smart tip calibration performance and distribution of the difference between FP and mCrutch.

In the example, after the calibration, the measured force \hat{F} shows, for the right crutch, an RMSE (root mean square error) < 10 N and a median difference of 2.8 N with an applied force range of approximately 400 N, while for the left crutch, it shows an RMSE < 5 N and a median difference of 1.6 N with an applied force range of approximately 200 N. Regarding the roll and pitch angles of the crutches, Figure 2.16 shows an example of rotations around the anterior–posterior (AP) and medio–lateral (ML) axes of the crutch

after the calibration with the SVD method. The accuracy in dynamic conditions shows an RMSE $< 5^\circ$ for rotations about the ML axis and an RMSE $< 4^\circ$ for rotations about the AP axis.

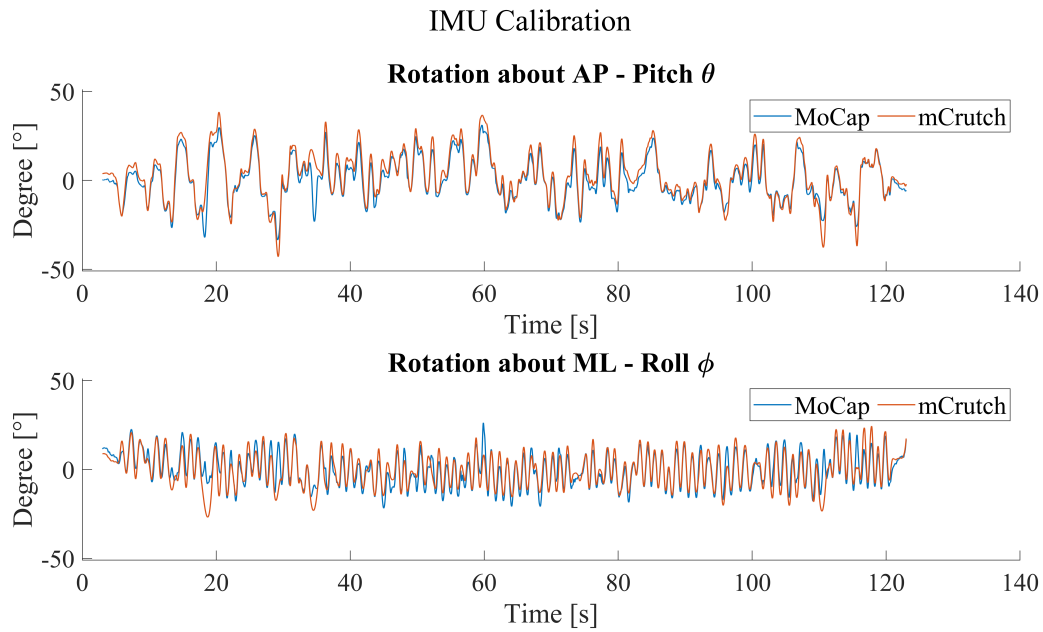


Figure 2.16: Smart tip calibration performance and distribution of the difference between FP and mCrutch.

2.3 Smart wearable system for chest and lung auscultation

The auscultation of a patient's chest is a safe, non-invasive, and inexpensive diagnostic techniques used by clinicians to diagnose various pulmonary and heart diseases. It is an important part of the patient examination and is considered an essential part of clinical diagnosis, even nowadays despite the broad range of available diagnostic technologies. The auscultation can be used to evaluate the airflow through the tracheobronchial tree distinguishing normal respiratory sounds from abnormal ones (e.g. wheezes, pleural friction rub and crackles) [72], or to assess heart sounds (valve opening and closure) or murmurs (blood flow turbulence) looking for cardiovascular disorder [73].

The design of a digital auscultation device requires a careful evaluation of the sounds occurring in the human body chest, mainly tones generated by lungs and heart. The heart sounds are the result of the blood flow which produces several different sounds, usually referred to as S1, S2, S3 and S4 [73, 74]. In a healthy patient, the most important heart sounds are S1 and S2: S1 is produced by mitral and tricuspid valve closure, S2 is due by aortic and pulmonic valve closure. Conversely, S3 is generated when a rapid reduction of blood supply from the left atrium to ventricle occurs, and S4 is related to a failure of heart in the diastolic period. In addition, murmurs generated by the whooshing made by rapid and turbulent blood flow can be acquired. Each of these sounds is characterized by specific frequency ranges: S1 50-60 Hz, S2 80-90 Hz, S3 20-30 Hz, S4 <20 Hz and murmurs 200-600 Hz [75, 76].

Lung sounds are produced during breathing. Similarly to what happens for the heart beating, respiratory tones audible from the chest can be divided into normal and abnormal [77]. Normal sounds and the relative frequency ranges are the following: bronchial 60-700 Hz [78] and vesicular 100-1000 Hz [77]. While abnormal noises and their frequency bands are [77]: wheeze 100-5000 Hz, stridor >500 Hz, rhonchus around 150 Hz, fine crackle around 650 Hz, coarse crackle about 350 Hz, pleural friction rub <350 Hz and squawk 200-300 Hz.

In this work, a signal conditioning circuit for analog microphones tuned on chest sounds frequencies is reported. The focus will be precisely on choosing the best microphone technology for the auscultation practice. In literature, there are many examples of microphone technologies comparison [79, 80], in a large number of applications, including human body auscultation [81, 82]. Nevertheless, the works about contact mics are quite old [81], [83], and they do not take advantage of the advancements of the MEMS mic

manufacturing technologies [82]. Regarding the practical usage of MEMS microphones in digital auscultation, some preliminary evaluations have been conducted [84, 85], and few auscultation devices were presented [86, 87], but there is a lack of comparison studies among the different microphone technologies.

Indeed, four mic manufacturing technologies were comparatively evaluated in this work: thin-disk piezoelectric diaphragms [88], electret condensers [89], analog MEMS [90] and digital MEMS [90]. These electro-acoustic transducers are the main ones that enable the design and realization of electronic stethoscopes [91, 92, 93].

Although digital stethoscopes have attracted the attention of researchers [93, 94, 95], and products are available on the market [96, 97], these new devices seem to be not yet widely adopted for biomedical purposes, regardless of many validations [98, 92, 99]. Besides, digital stethoscopes have superior performances w.r.t. acoustic ones in patient diagnosis, because of the ability to record and visualize, as well as to condition and amplify the signal giving acoustic feedback not audible with classical methods [87, 91].

Therefore, the intent of this work is to present a technologies comparison including MEMS solutions. Auscultation device testing is still in its infancy and no standard is available [100], a possible approach consists in using phantoms, either air coupled [101], or gel-based [102]. In this work, we adopted a solution similar to the one proposed in [103], based on a water-filled polymer ball.

Tests will focus on frequencies up to 5 KHz, since the coverage of all the chest sounds described above requires a frequency band in the range of 10 Hz-5 KHz. The audio benchmarks taken in account for each microphone are: frequency range, Signal-to-Noise Ratio (SNR) and the average power in the 10 Hz-5 KHz frequency range.

2.3.1 Microphones

The microphone is an electroacoustic transducer that converts sound waves into electrical signal. A mechanical system set into oscillations by sound fields is in charge of the conversion, usually via a diaphragm. The diaphragm vibrates when it is hit by acoustic energy, this vibration is then converted into an electrical signal by different sort of electromechanical coupling solutions.

Microphones are categorized by their transducer technology (for example dynamic, condenser, etc.), and by several characteristics such as those listed in Table 2.2: SNR, Sensitivity and Acoustic Overload Point (AOP) and Frequency response. The SNR is calculated with a reference acoustic level of 1 Pascal, which is standardized as a 94 dB Sound Pressure Level (SPL) 1 kHz tone at the microphone's capsule. The same acoustic reference is used to evaluate Sensitivity as well, which is the microphone signal output

magnitude when its capsule is exposed to a standard pressure level. AOP is the SPL value when the harmonic distortion present in a signal is equal to 10%. If the SPL value is higher than AOP, the harmonic distortion will be higher than 10%. Those main features are shown in Table 2.2 to provide an overview of the four chosen microphones and more details are provided in following Sections. The reported list is the result of a careful selection of the best-in-class sensors with the focus not only on performances but also on constructive approach, size, and cost to address auscultation. Therefore, we have chosen piezoelectric diaphragms by Murata, two STMicroelectronics MEMS microphones (one Analog, the other digital), and an high quality electret condenser mic.

Table 2.2: Microphones.

Model	Manufacturer	Technology	Size [mm]	SNR [dBA]	Sensitivity	AOP [dB SPL]
7BB-35-3L0 [104]	Murata	Piezoelectric diaphragms	35 \emptyset	-	-	-
EM272Z1 [105]	Primo	Electret Condenser	10 \emptyset x 4.5	80 ¹	-28 \pm 3 dB ³	119
MP23ABS1 [106]	STM	Analog MEMS	3.5 x 2.65 x 0.98	64 ¹	-38 \pm 1 dBV ²	130
IMP34DT05 [107]	STM	Digital MEMS	3 x 4 x 1	64 ¹	-26 \pm 3 dBFS	122.5

¹ A-weighted @ 1 KHz, 94 dBSPL.

² 0 dB = 1 V/Pa, VCC = 3 V, RL = 2.7 K Ω .

³ @ 1 KHz, 94 dBSPL.

It is worth noting that, in Table 2.2, SNR, Sensitivity, and AOP values for the mic “7BB-35-3L0” are missing because this component is used for general applications (vibration monitoring, sound detection, buzzer, haptic feedback, etc.) both as a sensor and as an actuator, so it’s not specifically characterized for audio applications. More details are in the following Subsections.

Piezoelectric Diaphragms 7BB-35-3L0

The Murata “7BB-35-3L0” (Fig.2.17) is a lightweight, ultra thin (0.53 mm) and circular piezoelectric diaphragms. It is based on piezoelectric effect and it is widely used in applications where contact is a requirement. Such sensor has already been applied in murmurs detection[108].



Figure 2.17: Murata Piezoelectric Diaphragms 7BB-35-3L0.

Electret Condenser Primo EM272Z1

The EM272Z1 (Fig.2.18) is an omnidirectional microphone capsule with solder pads for two wires connection. It is based on a Field Effect Transistor and an electret (crasis of ‘electricity’ and ‘magnet’), a dielectric material with a permanently dipole polarisation removing the need for a polarizing power supply. This microphone is characterized by SNR of 80 dB, -28 ± 3 dB and a maximum input sound pressure level of 119 dB. The manufacturer recommends their mic for recording natural sounds, backgrounds, and ambience thanks to the low noise and high sensitivity characteristics.



Figure 2.18: Primo Electret Condenser Microphone EM272Z1.

Analog MEMS MP23ABS1

MEMS microphones have a capacitive sensing element realized with specialized silicon micromachining processes. The MP23ABS1 (Fig.2.19(a)) by STMicroelectronics is a low-power (maximum $150 \mu\text{A}$) and compact device ($3.5 \times 2.65 \times 0.98$ mm) with a 64 dB SNR, an omnidirectional Sensitivity of -38 ± 1 dBV (at 94 dB SPL, 1 KHz), a 130 dB SPL AOP and a flat frequency response up to 15 KHz. This device comes with a metal casing to improve product robustness and reliability. Moreover, the substrate embeds capacitance plating to improve RF immunity and the base is provided with a sound pickup hole. The applications are wearables, hearables and smart speakers.

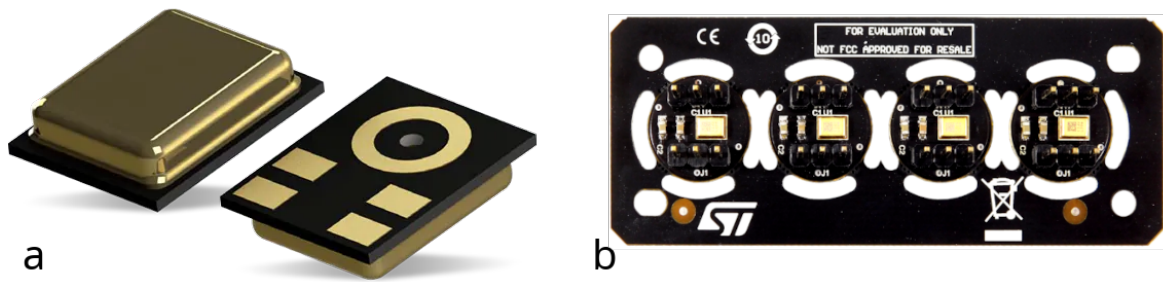


Figure 2.19: STMicroelectronics Analog MEMS microphone MP23ABS1: (a) device, (b) STEVAL-MIC004V1 evaluation board.

The testing of the MP23ABS1 mic was performed with an evaluation board, namely the STEVAL-MIC004V1 (Fig.2.19(b)). It is a daughterboard containing four single-coupon boards hosting each one a MP23ABS1 and a double three-pin header (2.54 mm pitch).

Digital MEMS IMP34DT05

In the STMicroelectronics product portfolio, there are not also digital output MEMS. The IMP34DT05 (Fig.2.20(a)) is a digital microphone that includes in a small form factor (3 x 4 x 1 mm) a dedicated circuit to provide a digital signal encoded with a Pulse Density Modulation (PDM). In addition, it offers a low-power consumption (650 μ A), omnidirectional directivity, a 64 dB Signal-to-Noise Ratio, -26 ± 3 dBFS Sensitivity and AOP of 122.5 dB SPL. The device's package is made of plastic with a ground ring around the sound pickup hole to enhance electrostatic discharges protection.

Some recommended applications are: sound detection, noise canceling, predictive maintenance, and vibration monitoring.

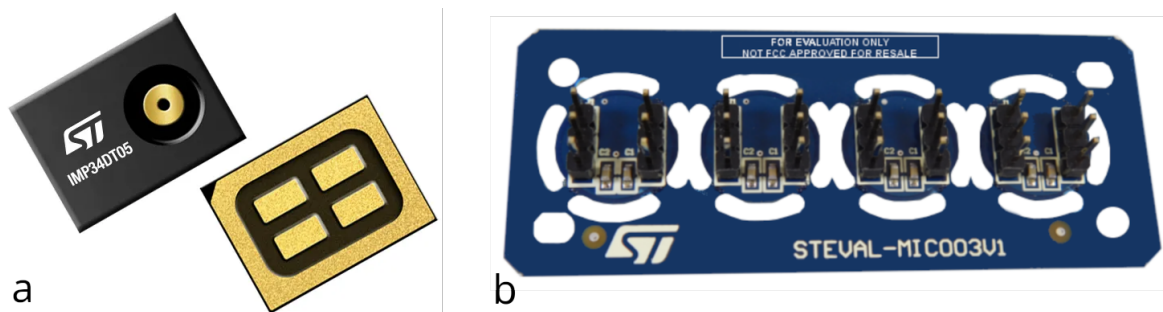


Figure 2.20: STMicroelectronics Digital MEMS microphone IMP34DT05: (a) device, (b) STEVAL-MIC003V1 evaluation board.

For the testing of IMP34DT05 we have used the STEVAL-MIC003V1 (Fig.2.20(b)), which features four coupon board in order to easily interface the digital mic to our acquisition board.

2.3.2 Gold Standard

For the selection of the transducer most suited for chest auscultation, a gold standard benchmark is needed. To this aim, we have chosen two of the most used digital stethoscope: Thinklabs One and eKuore. These were used in the test setup (Section 2.3.5) together with the chosen microphones, to enable a comparison in terms of sensitive frequency band and floor noise analysis.

Thinklabs One

Thinklabs One [97] (Fig.2.21) is a digital stethoscope that features multiple filter choices and can be used to acquire sounds from the heart, lungs, and other parts of the body. Unlike traditional devices, electronic amplification of sound is regulated through volume control. Volume and filtering controls can be used via buttons located on the device itself. The user can auscultate body sounds via external earphones, or record via device with on-board device (laptop, smartphone, etc. . .) connected via a 3.5 mm audio jack to the device.



Figure 2.21: Thinklabs One, digital stethoscope.

Briefly, some characteristics:

- Audio transmission: 3.5 mm audio jack;
- Audio amplification: 40 dB;
- Audio filters: 5 selectable bandpass filters;
- Display: Volume, filter, battery;
- Power supply: 5 V DC (compatible for USB charging) - internal lithium-ion battery;
- Battery life: 4 hours;

- Dimensions: 46 mm x 28 mm;
- Weight: 50 g;

About One's bandpass filters in our test, we used the wide band mode filter. The filters are:

1. 30-500 Hz, heart sounds, especially S3.
2. 60-500 Hz, heart sounds, whether filter 1 is too intense.
3. 80-500 Hz, lung sounds and heart valve clicks, S2 splits.
4. 100-1000 Hz, lung sounds.
5. 20-2000 Hz, wide band mode.

eKuore

eKuore (Fig.2.22) is a stethoscope that exploits a Wi-Fi connection to communicate with any smartphone or tablet via a free dedicated App. On those devices, the phonocardiograms of the heart and lungs can be recorded and viewed in real time, or shared with remote users. In addition, the auscultations can be performed using a headphone set thanks to device 3.5 mm jack connector.



Figure 2.22: eKuore, digital stethoscope.

Few features:

- Audio transmission: Wireless IEEE 802.11b/g and 3.5 mm audio jack;
- Audio amplification: 10 dB;
- Audio filters: 3 selectable bandpass filters;
- Display: Volume, filter, battery;
- Power supply: 5 V DC (compatible for USB charging) - internal lithium-ion battery;
- Battery life: 7 hours;
- Dimensions: 130 mm x 50 mm x 30 mm (WxDxH);
- Weight: 85 g;

Concerning on-board filters, for the test, we used the eKuore widest band filter, as we did for the Thinklabs One stethoscope. The three filters are:

1. 50-150 Hz, cardiac mode.
2. 50-500 Hz, lung mode.
3. 40-600 Hz, wide mode.

2.3.3 Chestpiece

An important element of the stethoscope (illustrated in Fig. 2.23) is the chestpiece. For this reason, in the characterization of the device performances, we have considered how this component may affect the results evaluating different solutions to house the mics, following the approach reported in [109]. More specifically, a chestpiece consists in two parts, a front side and back side (see Fig. 2.23), usually referred to as *bell and diaphragm*. The diaphragm may have a large diameter and is specially relevant for high-frequency sounds, such as those produced by breathing. While the bell impacts the quality of low-frequency sounds acquisitions, such as heart murmurs or breath sounds of pediatric patients who are smaller in size. Usually the diaphragm is made by a base metal drum, or cup, and by a rigid, flat, thin plastic disc of bakelite or epoxy-fiberglass compound, whereas the bell is a simple metal elongated cup. The noises generated by the human body cause the plastic disc vibration (when it is in contact with the patient's skin), which then generates the sounds heard when using the stethoscope chestpiece.



Figure 2.23: Stethoscope parts [110].

We realized five chestpiece models for the four microphones: for the piezoelectric diaphragm, a single size drum (Fig. 2.24) was realized; for the electret condenser and MEMS solutions, two chestpieces each were developed, the difference being in the small (Fig. 2.25 and Fig. 2.27) or large (Fig. 2.26 and Fig. 2.28) dimensions. The piezo diaphragm size was fixed, so it was not possible to have two different cups for it, while, for the other solutions, two different cup sizes were analyzed in order to test the different responses.

All the cups were 3D printed with a PLA plastic filament. In the following pictures, the designs obtained using the web app for 3D design Thinkercad [111] are depicted. The cups dimensions are suitable to host the diaphragm plastic disc. More specifically, the “3M™ Littmann® Stethoscope Spare Parts Kit Classic III™ Cardiology IV™ and CORE, 40016, Black, 10 Kit/Case” [112] was purchased, a kit with two plastic diaphragms (one shown in Fig. 2.31) suitable for the various cups and for large and small sizes.

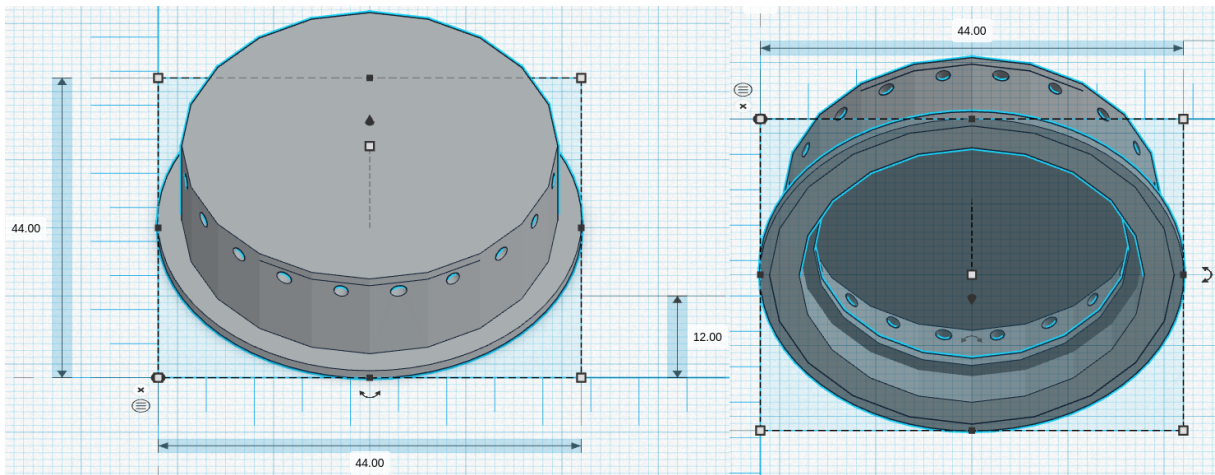


Figure 2.24: Cup for piezoelectric diaphragm.

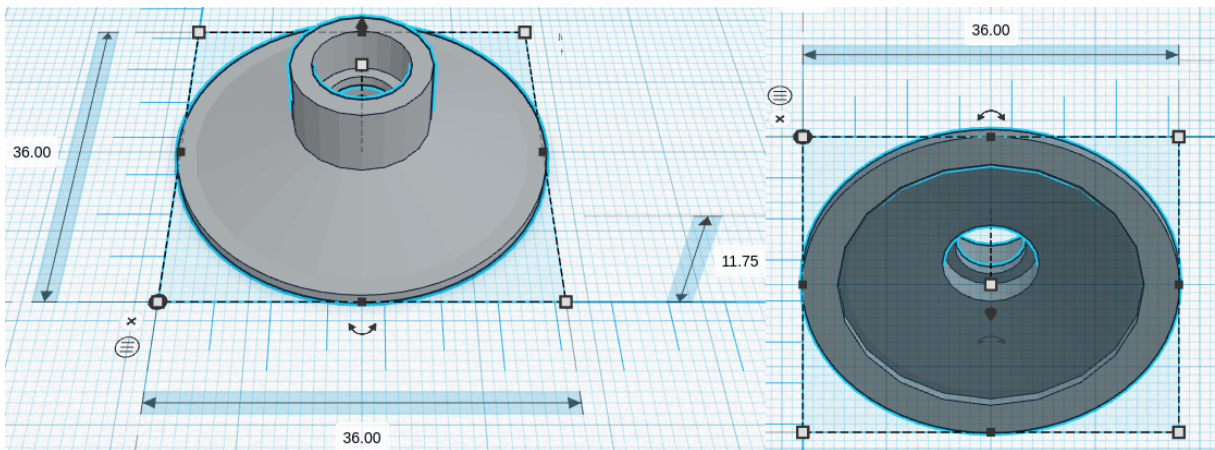


Figure 2.25: Cup size small, for electret condenser mic.

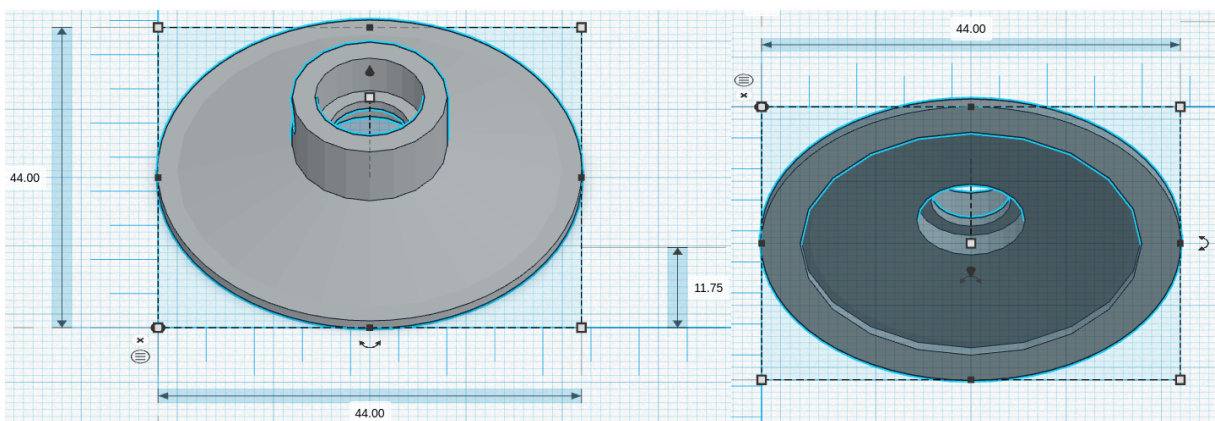


Figure 2.26: Cup size big, for electret condenser mic.

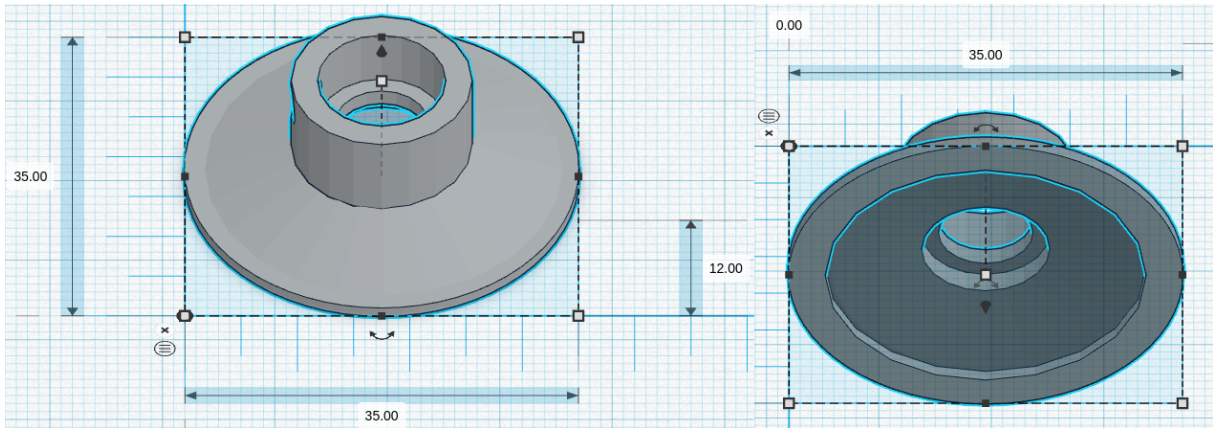


Figure 2.27: Cup size small, for MEMS mics.

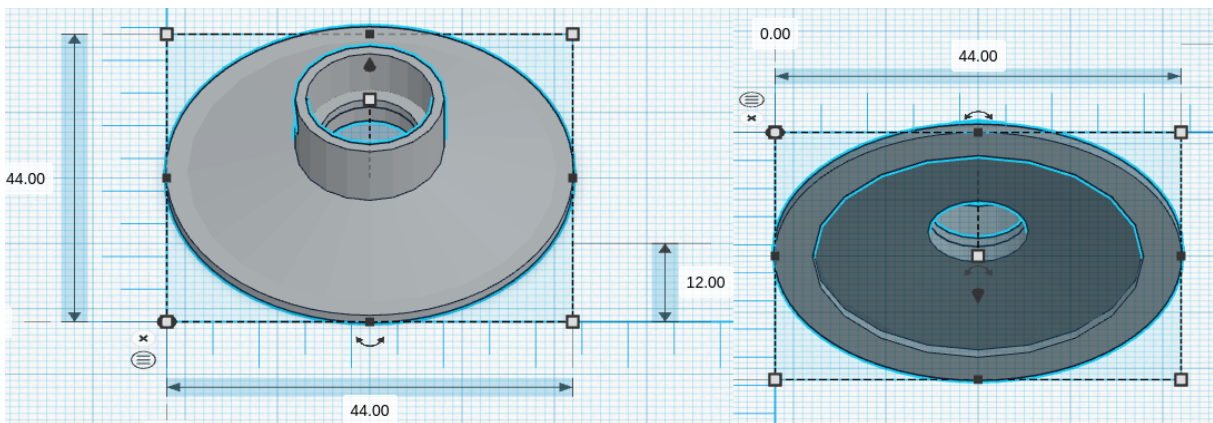


Figure 2.28: Cup size big, for MEMS mics.

2.3.4 Electronic prototype

The aim of this research is the comparison between microphone technologies suitable for patients auscultation. Since the target of those technologies is intended for electronic stethoscope application, we have developed a digital acquisition system to evaluate the mics using a plausible acquisition chain. The electronic prototype has been developed as a modular system to support both digital and analog microphones, and a dedicated board for signal measurement and transmission. In particular, the following components have been used:

- The “Data acquisition and transmission board” hosts the Microcontroller Unit for data acquisition feature and acts as USB PC peripheral for data transfer to a Personal Computer for data post-processing.

The main component, a STM32 MCU, is a high-performance STM32L552RE, which integrates an ARM Cortex-M33 core operating at a frequency up to 110 MHz, with a single-precision Floating Point Unit, a Digital Signal Processing instruction set,

256 KiB of SRAM and 512 KiB of Flash memory. It embeds two fast (5 Mbps) 12-bit Analog-to-Digital Converter (ADC), four digital filters for external sigma delta modulators (Digital Filter for Sigma-Delta Modulator peripheral - DFSDM) and various communication interfaces: Full-speed USB, SPI, UART, etc.;

- The “Piezoelectric preamplifier board” is the interface for piezoelectric diaphragms, it embeds two precision dual-channel operational amplifiers (op-amp) in inverting configuration with an overall gain around 22 dB in about 1 Hz-20 KHz band and a noise voltage level of 12 μ V.

The op-amps are from Texas Instrument, the OPA2197 [113] a low-noise ($5.5 \text{ nV}/\sqrt{\text{Hz}}$ at 1 KHz) and wide bandwidth (10 MHz) dual-channel Op-amp with low-offset voltage of $\pm 100 \mu\text{V}$ and low-bias current of $\pm 5 \text{ pA}$. Electronic schematic in Figure 2.29;

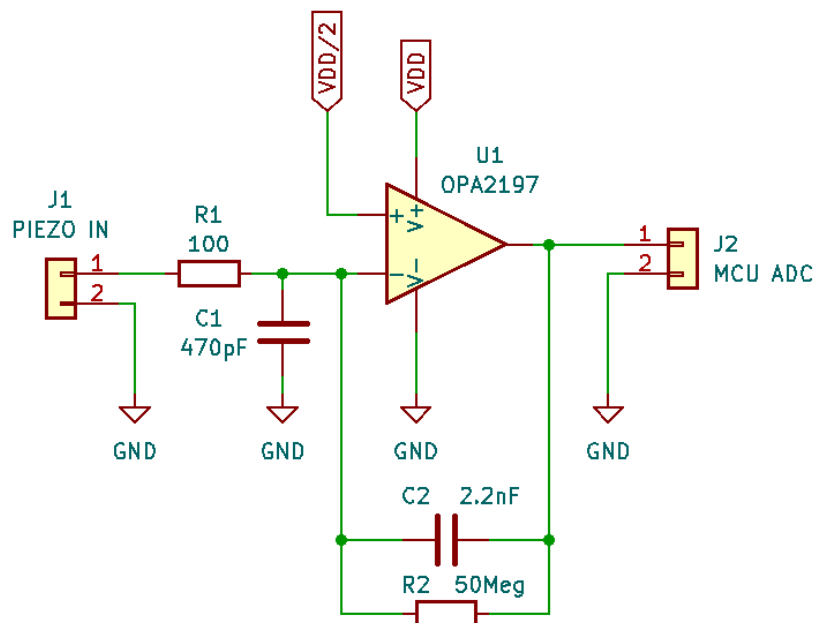


Figure 2.29: “Piezoelectric preamplifier board” electronic schematic.

- The “Analog preamplifier board” is suitable for MEMS and condenser analog microphones.

As the “Piezoelectric preamplifier”, it is based on OPA2197, but with a different configuration: a non-inverting circuit with resistive feedback. The gain is around 23 dB in a frequency band of 1 Hz-20 KHz. The schematic is shown in Figure 2.30;

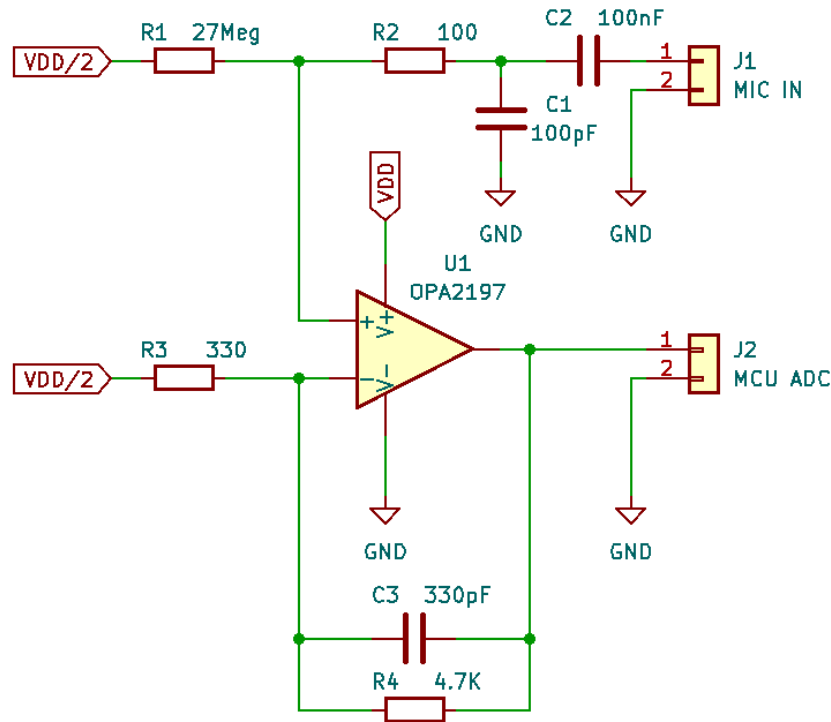


Figure 2.30: “Analog preamplifier board” electronic schematic.

In Figure 2.31, the Printed Circuit Boards of the above-mentioned components are depicted together with a top and bottom view of a couple of chestpieces realized to test the various microphones discussed in Section 2.3.1. Moreover, it worth noting that it was implemented a flexible stacking architecture so that the “Data acquisition and transmission board” can host both “Analog preamplifier board” and “Piezoelectric preamplifier board” to interface MCU ADC channels to analog microphones and piezoelectric solution. While the digital mic can be connect directly to the MCU DFSDM peripheral employing the “connectors to upper layer” without any additional board, or adapter. A programmer connector for code loading and debug purposes is included in the data acquisition board, together with a USB port to use the device as a serial PC peripheral. Currently, the device is not used as a standalone system, but rather as a test bench for the mics characterization. Therefore, it is connected via USB to a laptop and it is controlled by a MATLAB® 2021b interface-script; the acquisition starts when a “Start” command is received by the MCU Layer. A multi-thread buffer strategy allows data to be sent to the host by continuously recording signals without any data loss. Similarly, the acquisition ends when the “Stop” command is received by the MCU Layer. At this stage, the device is powered by the laptop battery itself. The Matlab software saves the audio signals and transmit them to the audio output of the PC for real-time listening. In order to perform a high-quality acquisition, the system features an enhanced dynamic range to obtain a best-in-class digital conversion with a sampling frequency of 44 Ksample/second/channel

at a 12 bits resolution for the analog signals. For the digital mic, the MCU DFSDM interface performs sampling at a frequency of 44 Ksample/second/channel at 16 bits. The different board configurations have the capability of acquiring up to 4 different channels simultaneously.

The main features are listed here:

- Audio transmission: Full-speed USB;
- Audio amplification: 22-23 dB;
- Audio filters: Custom on Matlab;
- Power supply: 5 V DC;
- Dimensions: 40 mm x 48 mm x 25 mm (WxDxH);

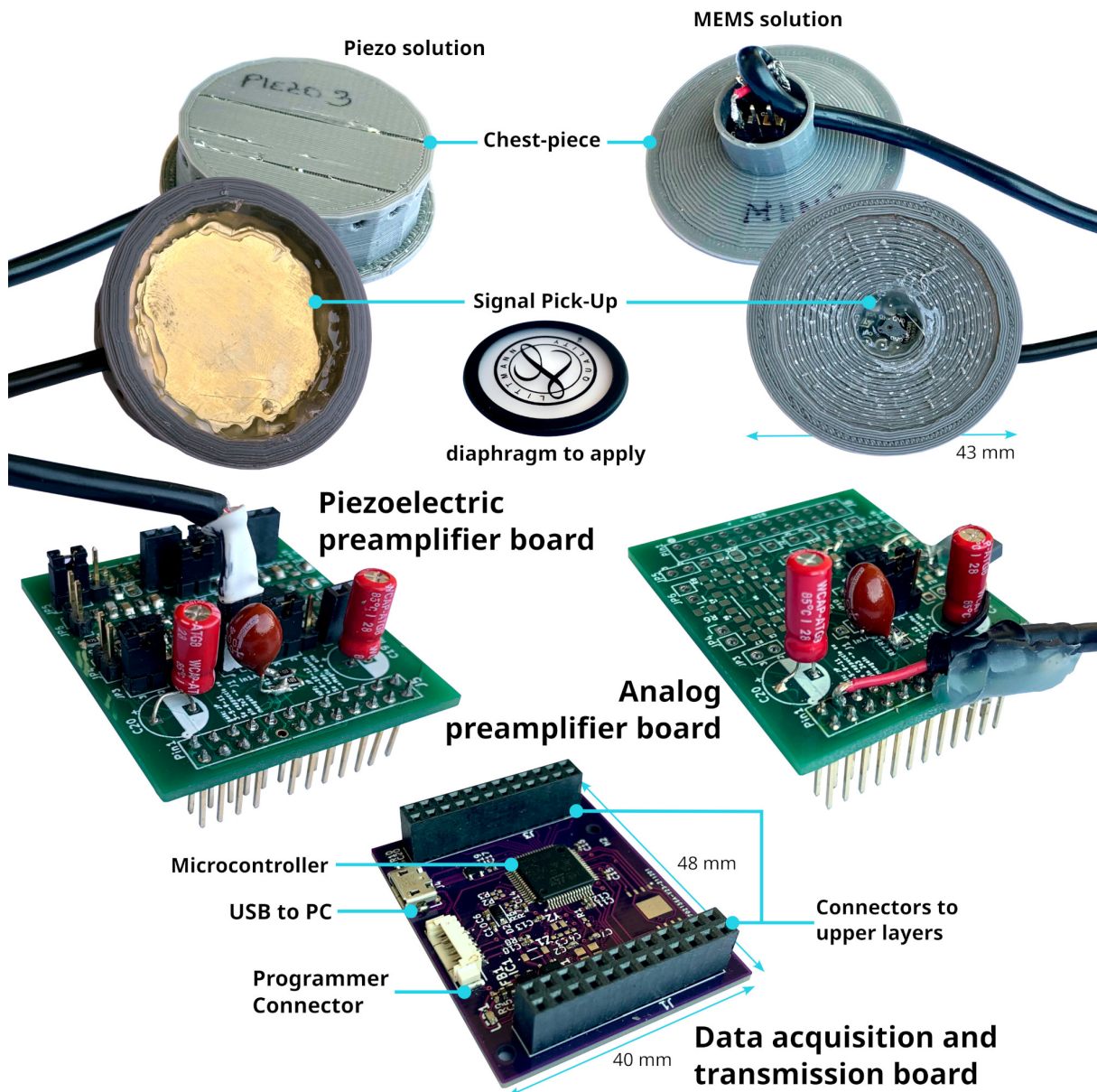


Figure 2.31: The developed auscultation device prototype components.

2.3.5 Setup

It is worth noting that, even if many experimental setups have been proposed in literature [102, 114], no standard procedure to characterize the auscultation devices performances has been developed [115, 103]. In this work, the tests of the various microphones introduced in Section 2.3.1 were performed with the setup illustrated in Figures 2.32, 2.33 and 2.34. In particular, the setup is made by a laminated plywood board in which it is housed a full range loudspeaker LG 6400GSMC01A (Fig. 2.32 - 70 mm diameter, 25 W, 6ohm impedance) and a latex rubber balloon filled with water. The transducers were placed in different measurement positions, i.e. Position 1 and 2 in Fig. 2.33, in order

to verify whether the acquisition performances are influenced by the wave direction of arrival. In detail, the balloon is a standard 26 cm party balloon and its full water weight is 1.9 Kg, while the green elastic band which holds the microphones in their position (see Fig. 2.32 and Fig. 2.33) is a standard No 33 [116] band size (90 mm x 3.0 mm).



Figure 2.32: Laminated plywood board, part of the auscultation phantom setup to test microphone technologies.

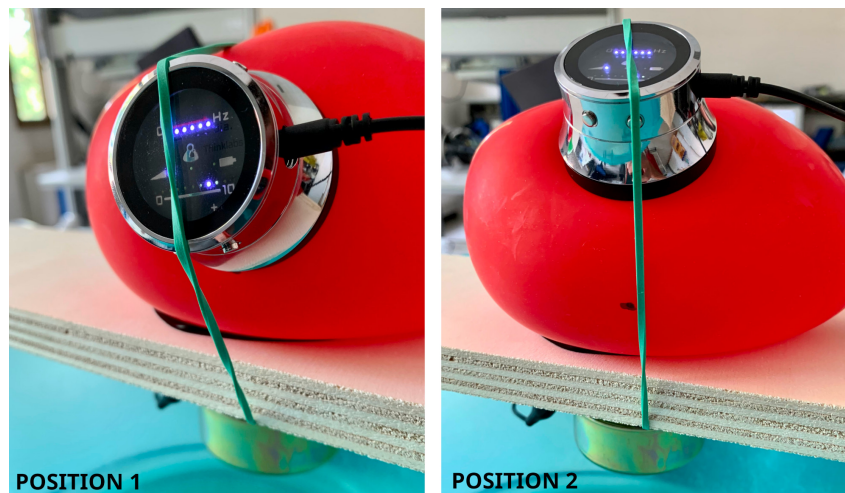


Figure 2.33: Auscultation phantom setup, on left side the Position 1, on right one Position 2.

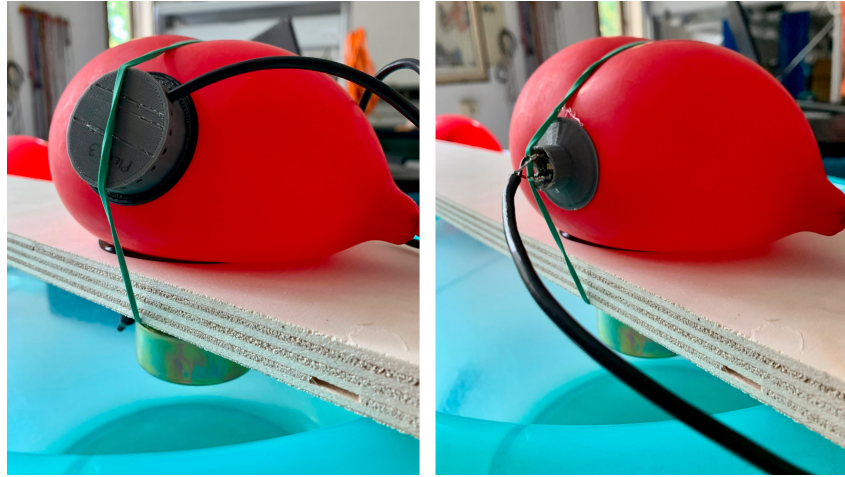


Figure 2.34: Test of piezoelectric diaphragm (left) and digital MEMS (right).

The realized test bench is meant to mimic the sound propagation in a medium with human body-like density (around 985 Kg/m^3). For this reason, the balloon was filled with water (density equal to 997 Kg/m^3). In the following, the list of the mics and the related acquisition board configurations is provided:

- Piezoelectric Diaphragms 7BB-35-3L0, “*Data acquisition and transmission board*” and “*Piezoelectric preamplifier board*”, with a firmware for ADC input.
- Electret Condenser Primo EM272Z1 and analog MEMS MP23ABS1, “*Data acquisition and transmission board*” and “*Analog preamplifier board*”, with a firmware for ADC input.
- Digital MEMS IMP34DT05, “*Data acquisition and transmission board*”, with a firmware for DFSDM.

The two measurements positions where we applied the microphones on the balloon are marked by a black marker and for each one we have performed two measures: one generating by the loudspeaker white noise, the other one in total silence. The white noise was generated by connecting the setup speaker to a PC sound card and featuring “RDNet” 4 software by RCF [117]. In Figure 2.35 the setting of RDNet. The purpose of the silent mode test is mainly to evaluate noise rejection in addition to operational bandwidth, while the white noise mode test focuses on evaluating the frequency response of the whole system.

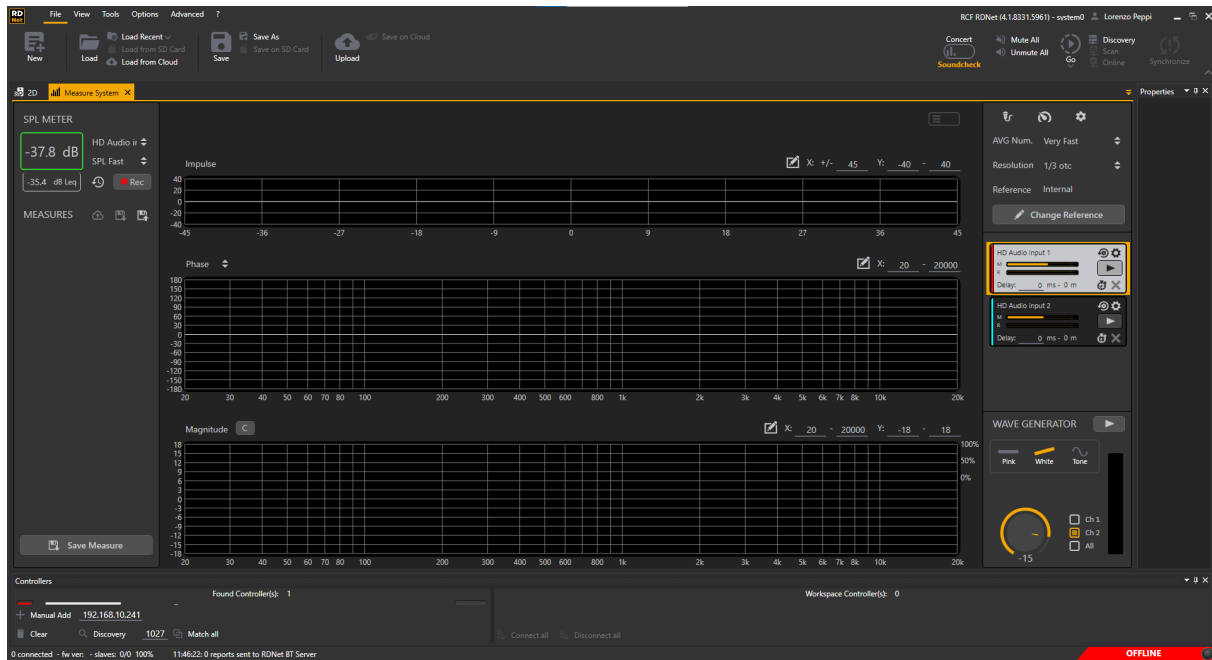


Figure 2.35: RDNet settings for white noise generation.

2.3.6 Results

As anticipated, chest sound components are generated by different sources in different bands. The following list summarized the frequency bands of interest, whose details are provided in the introduction:

- Band 1: 8 – 100 Hz, related to mechanical cardiac events and containing information about valve functionalities and cardiac muscle contractility [118].
- Band 2: 20 – 1000 Hz, related to the opening and closing of the heart valves, along with pumping of blood into the arteries and veins [119].
- Band 3: 20 – 200 Hz, heart sounds [119].
- Band 4: < 100 Hz, seismocardiography, defined as the micromovements of the chest wall in response to pumping of blood at every heartbeat [120].
- Band 5: 60 – 5000 Hz, respiratory sounds [78, 77].

In order to obtain the evaluation of a device capable of operating in both the cardiac and respiratory bands, the effective band of interest by joining the above bands is between 8 Hz and 5000 Hz. Therefore, a Power Spectral Density (PSD) up to 10 KHz was analyzed for each microphone. More specifically, each signal (x) has been processed in three steps: i) calculation of the Root Mean Square (RMS) value (Eq. 2.7), ii) normalization (Eq. 2.8), iii) PSD estimation with the Welch periodogram (Eq. 2.9). In the step iii), the PSD was

estimated with the longest possible segmentation to achieve high-frequency resolution: the signal was subdivided into 8 segments with 50% overlap and each one was windowed with Hamming windows. In Equation 2.9, the m th $w(m)$ is the Hamming window of the m -th segment, R is defined as the window hop size, and K denotes the number of available frames (8 by “pwelch” Matlab function). Then, the PSD signal is just an average of \hat{x}_m periodograms across time.

$$RMS = \sqrt{\frac{1}{N} \sum_{i=1}^N |x_i|^2} \quad (2.7)$$

$$\hat{x} = \frac{x}{RMS} \quad (2.8)$$

$$\begin{aligned} \hat{x}_m(n) &= w(m)x(n + mR), n = 0, 1, \dots, M - 1, m = 0, 1, \dots, K - 1, K = 8 \\ \hat{S}_{\hat{x}}^W(\omega_k) &= \frac{1}{K} \sum_{m=0}^{K-1} P_{\hat{x}_m, M}(\omega_k) \end{aligned} \quad (2.9)$$

In the following graphs, the results for the selected transducers (Section 2.3.1) and the gold standards (Section 2.3.2) are presented for Position 1 and Position 2. For each position, measurements in silence mode and in white noise loudspeaker playback mode were performed. Furthermore, the spectral coefficients were filtered with the 1/3-Octave smoothing filter [121, 122], as typically done for audio PSDs graphing improvement. In the plots, the spectrum for each mic or commercial stethoscope is displayed, labeled as:

- “*EMic_bChp*”: Electret Condenser EM272Z1, with chestpiece size “big”.
- “*EMic_sChp*”: Electret Condenser EM272Z1, with chestpiece size “small”.
- “*Man_bChp*”: analog MEMS MP23ABS1, with chestpiece size “big”.
- “*Man_sChp*”: analog MEMS MP23ABS1, with chestpiece size “small”.
- “*Mdig_bChp*”: digital MEMS IMP34DT05, with chestpiece size “big”.
- “*Mdig_sChp*”: digital MEMS IMP34DT05, with chestpiece size “small”.
- “*PiezoDiaph*”: Piezoelectric Diaphragms 7BB-35-3L0.
- “*TOne*”: gold standard digital stethoscope Thinklabs One.
- “*eKuore*”: gold standard digital stethoscope eKuore.

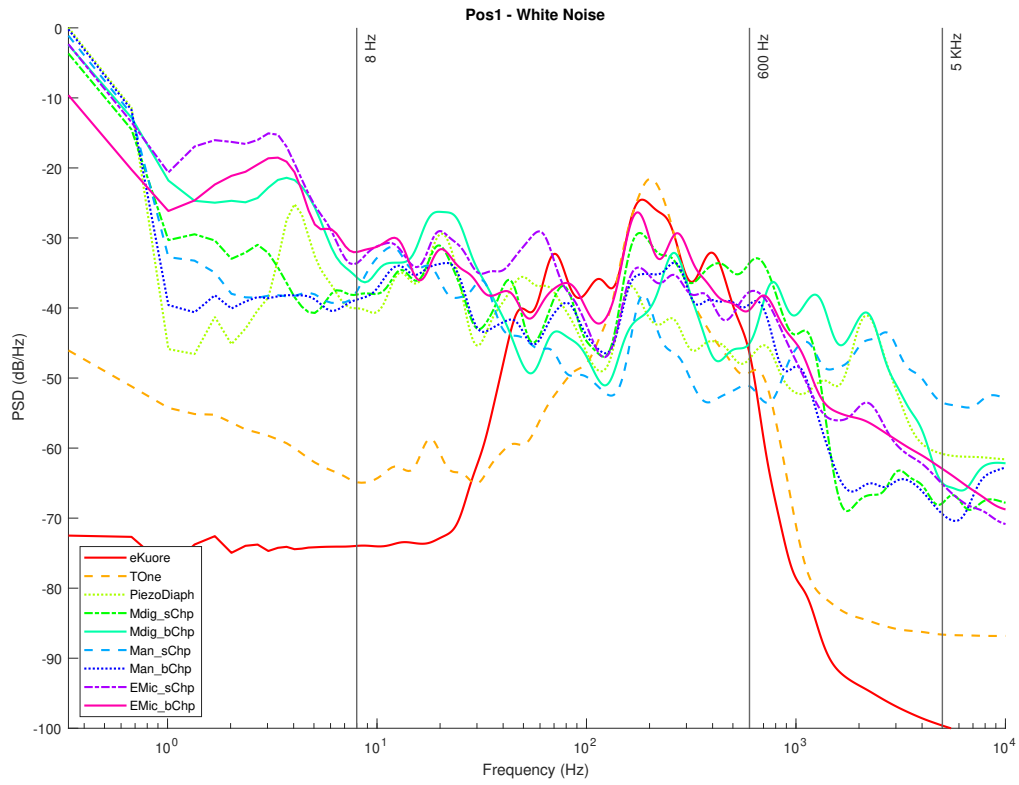


Figure 2.36: Position 1, normalized PSD microphones acquisitions with white noise.

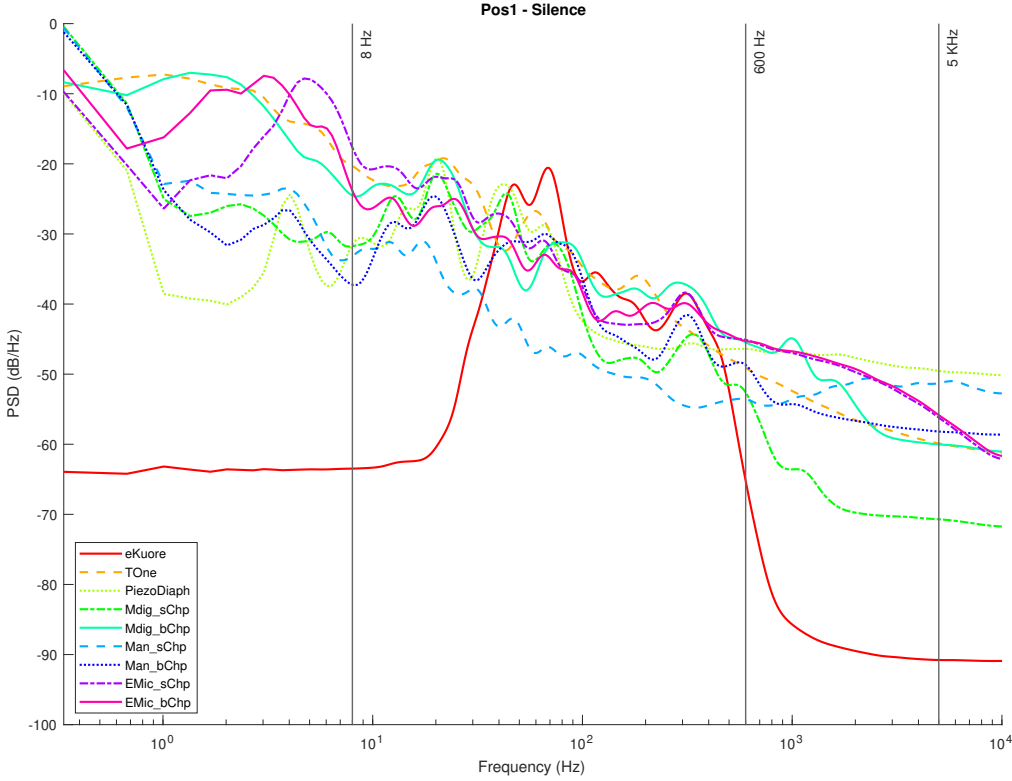


Figure 2.37: Position 1, normalized PSD microphones acquisitions in total silence.

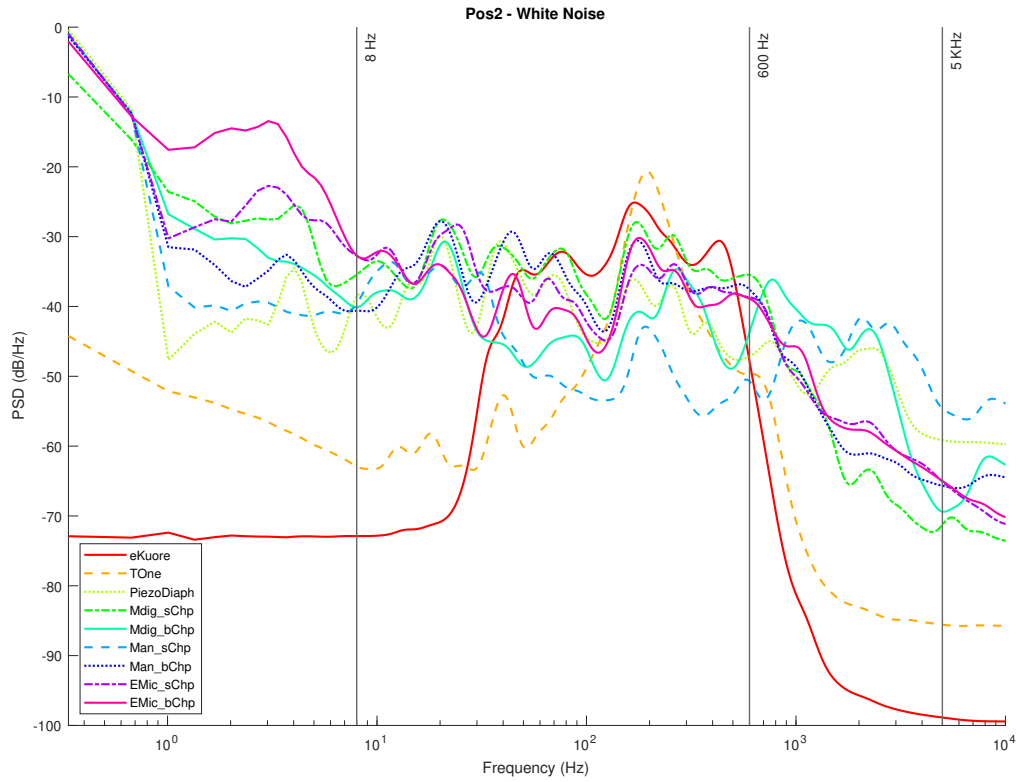


Figure 2.38: Position 2, normalized PSD microphones acquisitions with white noise.

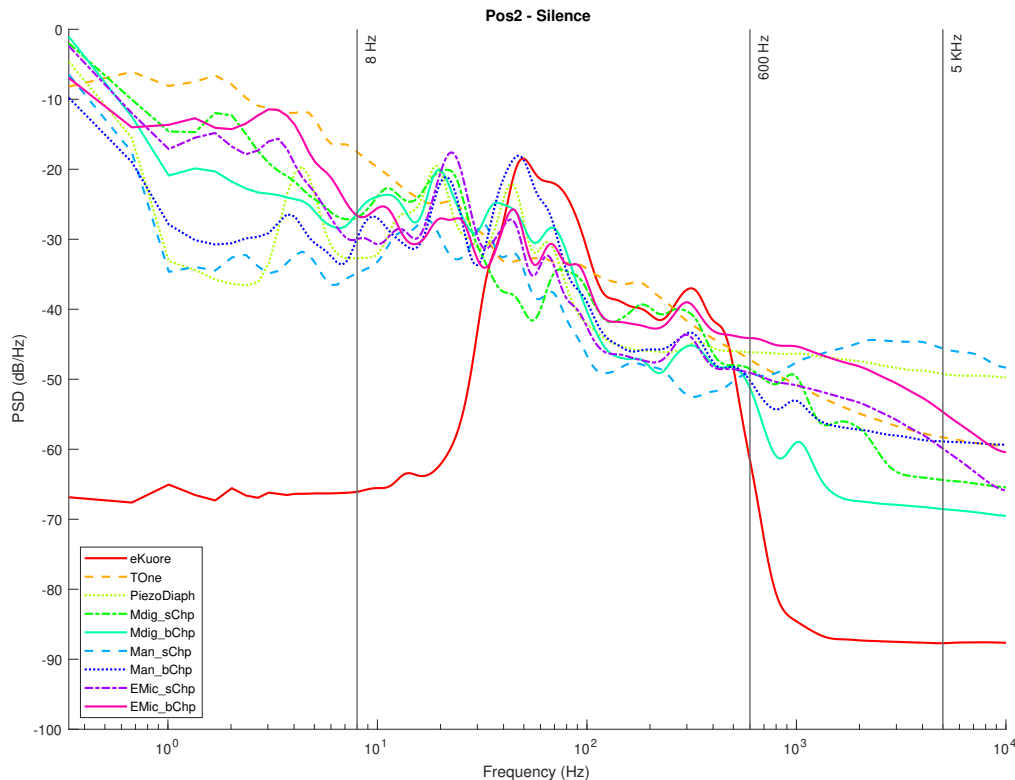


Figure 2.39: Position 2, normalized PSD microphones acquisitions in total silence.

From the PSD graphs, it is noticeable the effect of the on-board bandpass filter in the two commercial solutions, Thinklabs One and eKuore. In particular, in the plots related to white noise acquisitions (Fig. 2.36 and Fig. 2.38), it is possible to give a qualitative evaluation of the transducers bandwidth, and the best solutions are the analog MEMS with a small cup, the digital MEMS solution with a big cup and the piezoelectric diaphragm. Table 2.3 summarized the results of the upper graphs in terms of upper cutoff frequency at -50 dB/Hz.

Table 2.3: Upper cutoff frequencies (Hz): Position 1 in first row, Position 2 in second row.

	EMic_bChp	EMic_sChp	Man_bChp	Man_sChp	Mdig_bChp	Mdig_sChp	PiezoDiaph	TOne	eKuore
P1	1198	1099	1118	3996	3008	1298	2937	705	633
P2	1192	1007	1074	4173	2808	1068	2886	663	618

To provide a more accurate assessment of the operating frequency band, we calculated the average power for PSDs between 8 and 5000 Hz (see the discussion on the frequency band of interest in the Introduction, and at the beginning of Section 2.3.6). Then, it was calculated the SNR, in order to assess the noise rejection capabilities of each transducer

on the frequency band mentioned above. The average power (POW_{avg}) is computed by integrating the PSDs, using the rectangle method (Equation 2.10), while the SNR values are the ratios between the POW_{avg} (computed when white noise (POW_{avg-wn} was applied) and the average power estimated during silence mode tests ($POW_{avg-sil}$).

$$POW_{avg} = \frac{1}{n} \sum_{i=1}^n (\omega_{i-1} - \omega_i) \left(\frac{\hat{S}_{\hat{x}}^W(\omega_{i-1}) + \hat{S}_{\hat{x}}^W(\omega_i)}{2} \right) \quad (2.10)$$

$$SNR = 10 \log_{10} \left(\frac{POW_{avg-wn}}{POW_{avg-sil}} \right) \quad (2.11)$$

The results of the above benchmark are reported in Table 2.4.

Table 2.4: SNR evaluation (dB): Position 1 in first row, Position 2 in second row.

	EMic_bChp	EMic_sChp	Man_bChp	Man_sChp	Mdig_bChp	Mdig_sChp	PiezoDiaph	TOne	eKuore
P1	11.37	9.14	13.52	8.14	15.99	7.38	6.64	13.65	11.80
P2	9.14	4.21	4.18	4.17	9.67	7.64	7.01	16.10	11.92

The gold standards show better performances than the chosen technologies, this is due to the fact that the on-board signal condition plays a key role in improving performance, while on our solution we preferred to focus on the comparison of raw data acquisitions. Among the mics technologies, it can be concluded that the best solution in terms of SNR is the digital MEMS application.

To summarize the results, we have performed four audio recordings for each transducer considering two different acquisition positions and two type of acquired sounds: white noise and complete silence. We selected two different acquisition locations to check distinct sound propagation in the phantom setup. While the two kinds of sounds were imposed to compare the microphones sensitivity: i) random signal with equal intensity at different frequencies reproducing from the setup's speaker a white noise track, ii) complete silence. The sounds recorded by the microphones and the designed acquisition system have been post-processed to extract multiple features: PSD, PSD with octave filter, and average power in 8-5000 Hz band from which the SNR can be calculated. Specifically, from the filtered PSD, the devices' bandwidth can be estimated, while the SNR parameter illustrates the noise immunity. From the achieved results, the best performing technology is considered to be the digital MEMS-based technology, both for the large bandwidth (see Fig. 2.36, 2.38 and Table 2.3) and the high SNR level (up to 15.99 dB, see Table 2.4).

Besides the quantitative assessment reported so far, we conducted a preliminary qualitative assessment involving four trained cardiologists at the Department of Medical and

Surgical Sciences of the University of Bologna. All physicians reported a higher-sound quality of digital MEMS microphone with respect to the other technologies.

2.4 Conclusions

This Chapter presented three activities related to the bioengineering field.

The first activity is related to a new flow phantom set-up that overcomes problems such as cost, size and usability of the commercial solutions. To minimize size, 3D printing techniques were used to fit the hydraulic and control components in a very compact case. The developed flow phantom setup is a low-cost device, thanks to the introduction of a calibration phase based on a ARX model which overcomes the sample rate limitations of low cost flowmeters. The reported performances showed that a carotid physiological flow has been reliably generated, with minimal deviation of the achieved flow values with respect to the targeted ones. Finally, to enhance usability, it has been developed a dedicated GUI.

The second activity was related to the development of a gait monitoring device, i.e. the sensorized crutches shown in Section 2.2. In particular, this study aimed to present mCrutch, a low-cost smart device suitable for mobile health applications in the continuity of care scenarios. The system is composed of a set of instrumented crutches and a smartphone app and allows the collecting and processing in real-time orientation angles and applied loads. The current prototype shows an accuracy of approximately 10 N RMSE for the applied force and 5° for pitch and roll angles which allows bio-feedback and telemonitoring applications that require relatively low resolution, although clinically useful thresholds are yet to be established. Current and expected manufacturing costs for mCrutch are reasonable for a personal device, such as a walking aid. The suitability and clinical validity of mCrutch will be investigated in future studies for specific target populations and settings.

The third activity led to the creation of a device for chest auscultation that uses digital MEMS microphones, starting with the investigation of the suitability of different microphones technologies for auscultation. The selected transducers are based on various manufacturing approaches: piezoelectric diaphragm, electret condenser, analog MEMS and digital MEMS. The performances of the such solutions were compared with the ones achieved by using two commercial digital stethoscopes: Thinklabs One and eKuore. The comparison was based on the analysis of the parameters which are typically evaluated in studies related to auscultation sounds acquisition methods. However, this work did not focus only on testing the microphones performances, but also on developing i) an electronic digital acquisition device to be used as PC peripheral and ii) purposely designed transducers housing i.e. the 3D-printed chestpieces. The aim is to understand how close are the performances achievable with low cost-low power devices w.r.t. those achievable with commercial devices unsuited for prolonged use in wearable setups. Finally, we have

realized an ad-hoc phantom setup to perform acoustic tests simulating auscultation, but with an appropriate sound playback such as a white noise track. The results show how the MEMS technology can be reasonably considered for the auscultation of a patient, particularly the digital MEMS-based microphone solution. Furthermore, the application of this technology opens the possibility to auscultate sounds in a wider band, enabling a more precise patient diagnosis with low cost devices.

Chapter 3

Automotive

Abstract

One of the most compelling challenges that I faced during my PhD concerned the development of a sensing device for the automotive sector. Besides the integrability issues already tackled in the studies described in the previous chapters, the design task presented was complicated by strong environmental stress due to high speed rotation and temperature. This project was the result of a collaboration with HPE COXA, a company located in Modena which provides engineering solutions for automotive, motorsport, off-highway vehicle, automation solution and defence sectors. The objective of the research team I supervised was to develop an embedded system devoted to monitor internal temperature in electric motor.

Introduction

Temperature variations are a very important aspect in electric motors, because they can affect performance [123] or even cause irreversible damage such as magnet demagnetization [124] or stator windings deterioration [125].

Operating at high temperatures without incurring in the previously mentioned problems is a challenge that can be facilitated by operating the real-time measurement of inner motor temperatures [126]. There are many application domains in which performing such measurement is of the utmost importance. For example, studies have been carried out in the motor racing [127], robot application [128] and general industrial utilization [126, 129] fields.

Over the past 20 years, many studies have been conducted involving the measurement of temperatures in electric motors [130, 131, 132, 133]. However, all of the reported tests were performed at relatively low speed (< 4500 rpm) and with bulky instruments incompatible with permanent installations. The objective of the measuring device described in this research is to ensure temperature acquisition at speeds above 20 000 rpm from both

the stator, through the so called Station Board (Fig. 3.1), and the rotor of an Interior Permanent Magnet (IPM) motor via a purposely designed Sensing Board (Fig. 3.1).

It is evident that the stator temperature acquisition has no difficulty. In case of rotor measurements, conversely, it is also necessary to deal with the transmission of data from the rotating part to the static part. Due to rotation, the only alternative to sliding contacts is wireless data transmission. This thesis presents two prototypes that use the Bluetooth Low Energy (BLE) wireless protocol. Using the BLE protocol, it is possible to reduce the consumption to the point of obtaining a system capable of acquiring data continuously for an entire day of testing without the need to recharge the battery.

In the early part of this chapter is introduced the design, installation and test of a first acquisition system prototype, then the same steps are explained for an advanced version taking advantage of the experience on the first one. Few details on the electric motor used are provided, because a patent is pending.

The content of this Chapter is based upon the research works [P6] and [P7]:

- “A Wireless System for inner Temperature Measurement of High Speed Electric Motors” by Valič I., Zauli M., Matteazzi N., Foffano G. and De Marchi L. in 2021 IEEE International Workshop on Metrology for Automotive (MetroAutomotive), pp. 248–253, 2021. ©2021 IEEE.
- “A Wirelessly-Powered Embedded System for Temperature Measurements of a High Performance Electric Motor Rotor” by Nerone M., Valič I., Zauli M., Leonardi A., Matteazzi N. and De Marchi L. in 2022 IEEE International Workshop on Metrology for Automotive (MetroAutomotive), pp. 6–11, 2022. ©2022 IEEE.

From which part of the text is drawn. The first prototype was totally designed and developed by me and I supervised the realization of the second generation of the device.

3.1 First prototype

In Figure 3.1, it is shown the first solution designed and developed to handle the inner temperature measurement in an IPM motor. It's noticeable that the Station Board handles not only temperature acquisition and BLE communication with the Sensing Board, but also serial communication with a terminal (user interface).

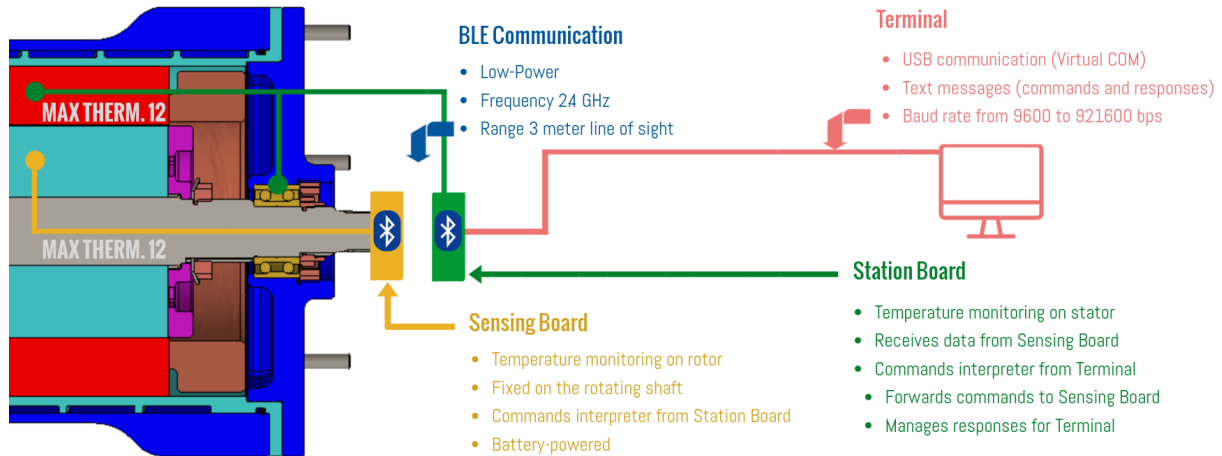


Figure 3.1: Architecture scheme of the described system. [©2021 IEEE]

3.1.1 Design

The realized acquisition system is divided into two main PCBs that are described below and shown in Figure 3.1. In this work, the two PCBs will be referred to as Sensing Board and Station Board, respectively.

- Sensing Board

This board is attached to the rotor rotating up to 20 000 rpm. It is battery-powered and its functions are summarized in Fig. 3.1.

- Station Board

This one is not connected to any rotating component and is linked via USB cable to the test bench for transferring both power and data. The functions it has to perform are briefly introduced in Fig. 3.1.

The Station Board, being stationary and easily accessible, is connected directly to the test bench. Clearly, this is not the case of the Sensing Board, which cannot be simply connected to the test bench since it is rotating at a very high speed. Consequently, a 500 mAh Lithium-Polymer battery was selected for providing energy through a boost DC-DC converter to the Sensing Board.

Despite this difference both boards have many common subcomponents: a MCU, a transceiver for BLE communication, an antenna, the connectors for the thermocouples and the thermocouple-to-digital converters for the thermocouples interfacing with the MCU. Thanks to this similarity, it was possible to develop only one PCB layout for both boards in order to speed up design and production. Just a minor modification was necessary for the Sensing Board because it should host the battery management circuit.

The main components used on each PCB are:

- NINA-B306 module which integrates the Bluetooth 5.2 System on Chip (SoC) nRF52840 from Nordic Semiconductor and a PCB antenna. The SoC is composed of several parts. Among these, the Arm Cortex-M4 MCU and the multiprotocol transceiver should be highlighted. This module handles acquisition, processing and transmission.
- 12 K-type thermocouples with a wires size of 41 AWG.
- 12 MAX31850 thermocouple-to-digital converters, each of which allows a resolution of 0.25° (14-bit) and integrates a cold-junction compensation. The communication is performed over a 1-Wire interface with the microcontroller.
- 6 Molex Pico-Blade 4-pin connectors for the connection of the thermocouples to the PCB, up to two for each connector.
- MCP73831T which is a charge management controller for single cell Lithium-Ion, or Lithium-Polymer battery.

In Figure 3.2 all the components of the Station Board are illustrated, while in Figure 3.3 the Sensing Board elements are shown.

The transmission BLE protocol was chosen because it is characterized by a high operating frequency (2.4 GHz). Especially, at the beginning of this project it was evaluated the use of Near Field Communication (NFC) wireless technology, but an Electromagnetic Compatibility test on this kind of motor shown high emissions in the band 10-300 MHz, up to $70 \frac{\text{dBuV}}{\text{m}}$ at 15 MHz. Noises given principally by the inverter to power the electric motor at the engine test bed, the main place of use of the presented measuring system. Accordingly, to prevent Radio-Frequency Interference it was chosen a higher frequency transmission, so the BLE at 2.4 GHz. Furthermore, such protocol features low power consumption (in this project up to 35 mA) and a relatively high data rate (up to 1.4 Mbps) thanks to the NINA-B306 module. About the wireless transmission correlated with the rotation, a doppler effect is not presumed, since the transmitter and the receiver are facing each other as shown in Fig. 3.1.

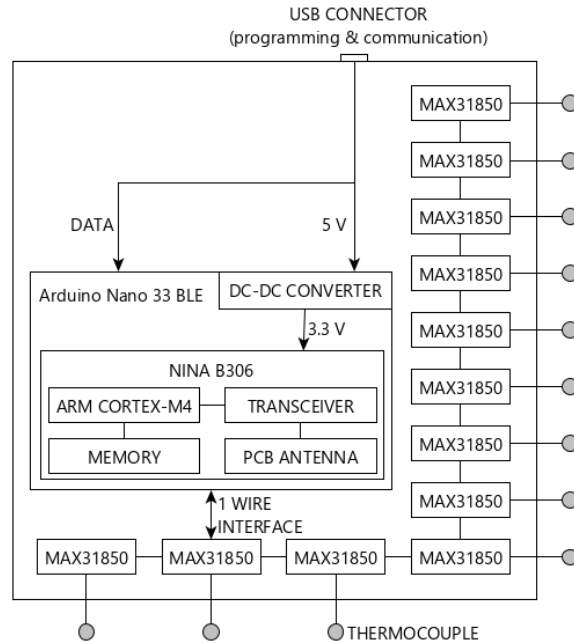


Figure 3.2: Station board architecture scheme. [©2021 IEEE]

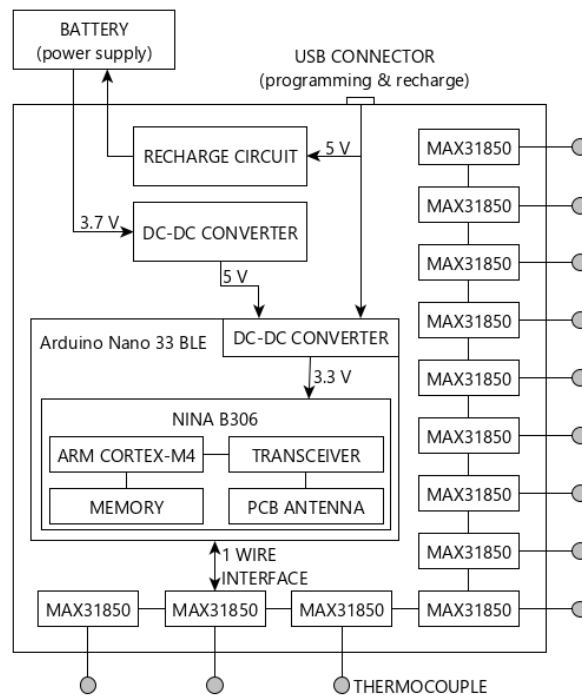


Figure 3.3: Sensing board architecture scheme. [©2021 IEEE]

Considering the high rotating speed, it is very important to ensure a proper attachment of the Sensing Board to the rotor. This is guaranteed by a properly designed mechanical support (see Fig. 3.4), which has to be balanced after the assembly phase to prevent unwanted vibrations. It is clear that, after the balancing process is performed, additional

mechanical alterations (such as replacing the battery) have to be avoided. Consequently, the Sensing Board also integrates a battery recharge circuit basing on MCP73831T, that allows to perform a charging cycle by simply plugging in a USB cable.

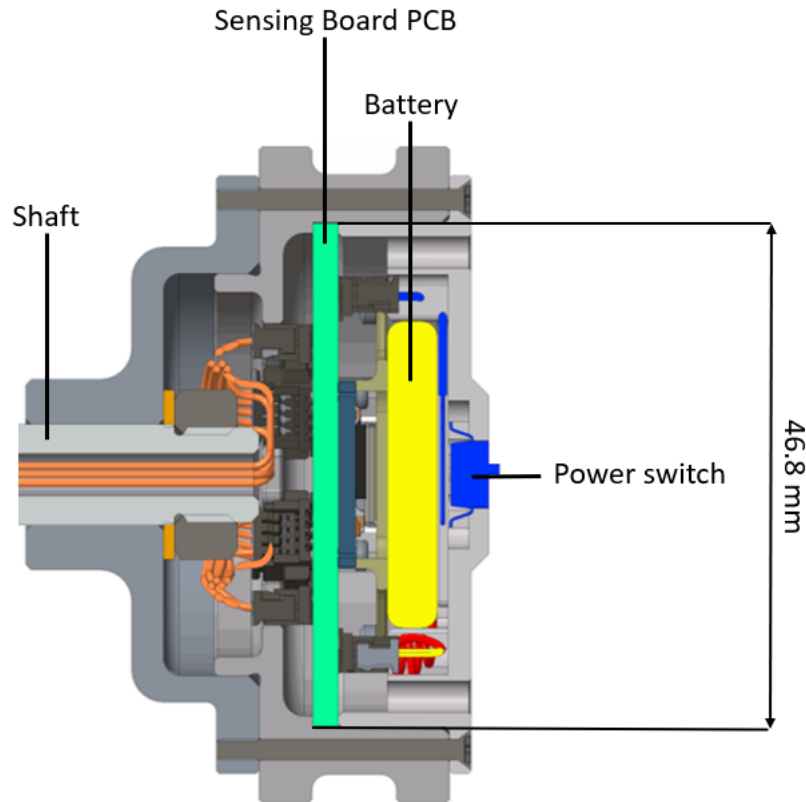


Figure 3.4: The mechanical system that anchors the Sensing Board to the shaft. [©2021 IEEE]

Regarding the use of an intermediate material between the thermocouple wire terminals and the PCB copper trace, in this case it doesn't introduce any Electromotive Force (EMF), therefore any temperature noises are introduced. In particular the intermediate metal is given by the 6 Molex Pico-Blade, specifically by the female and male crimp terminals made by tin. For these metal connectors there aren't EMF contribution because the junctions of the third metal are supposed at the same temperature and that is explained by thermocouple law of intermediate metals [134]. Moreover, the cold-junction compensation integrated in the MAX31850 helps to realize an accurate measuring system with the monitoring of the reference junction, or "cold" junction, the point of the Pico-Blade connectors placed close as possible to the corresponding thermocouple interface.

Summarizing, in table 3.1 are listed the features of the measurement system realized. Currently the temperature acquisitions have been calibrated using thermocouple type K, but the system also support J-, N-, T-, S-, R-, or E-type and different measuring range.

Table 3.1: Temperature measuring system specifications.

Feature	Station	Sensing
	Value	
Temperature Sensor	Thermocouple Type K	
Measuring range	0 – 250 °C	
Resolution	0.25 °C	
Channel	12	12
Connectivity	USB-BLE	BLE
Power supply	USB	Battery Li-Poly 500 mAh

3.1.2 Installation

The proposed measurement system was installed on an Interior Permanent Magnet Synchronous Motor (IPMSM) whose geometrical dimensions are 170 mm (diameter) x 270 mm (length) and it is designed by HPE COXA in Modena. The main goal is to measure the temperatures with the aim of predicting and preventing in particular the phenomenon of demagnetization.

One of the most critical procedures of the entire project is the installation of the thermocouples in the rotor. For this purpose the shaft has been modified to accommodate the thermocouple wires in a special hole along the axis of rotation. From this central hole, there are branches that allow access to the measurement points (Fig. 3.5), which are: the inner and outer faces of the magnets, the bearings and the rotor-shaft interface.

As far as the rotor is concerned, the main measurement points are the conductor holes slot, the stator end windings and the interface between stator and the water jacket.

Another point of measurement is also the bearing since it can be a critical part at very high speed.

Once installed, the thermocouples have to be connected to the PCBs. This is obtained through 6 Molex Pico-Blade connectors, each one can host two thermocouples.

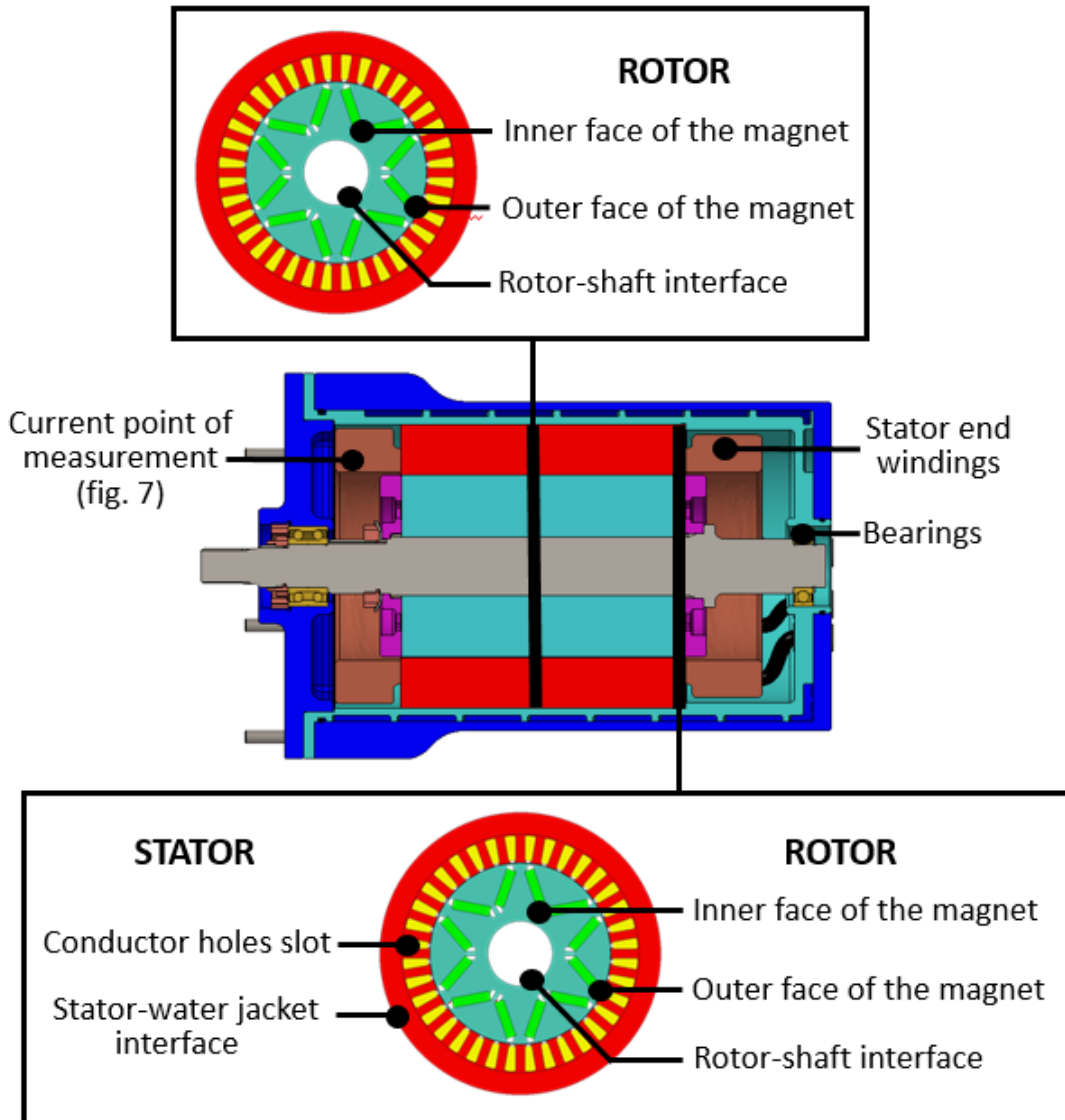


Figure 3.5: Position of the main installed thermocouples. [©2021 IEEE]

3.1.3 Development and test

The first prototype was developed with the goal of meeting the needs of the Sensing Board since it is the critical one in terms of dimensions, shape and behavior at very high speed.

In order to minimize the vibrations introduced by the board rotation, everything was developed trying to keep it symmetrical. This is clearly visible in Fig. 3.6, looking for example at the shape of the board or the position of the connectors. The final result is a circular PCB with a diameter of 46.8 mm. As anticipated, this PCB has been used as ground basis for the design of the Station Board too.

As far as the Station Board is concerned, it's all simpler since there are no problems introduced by rotation and spatial constraints. For this reason the Station Board is just

the Sensing Board with no battery management circuit mounted.

Furthermore, to make the development process faster an Arduino Nano 33 BLE board was integrated on the custom PCB. The Arduino board embeds the Nina B306 module.

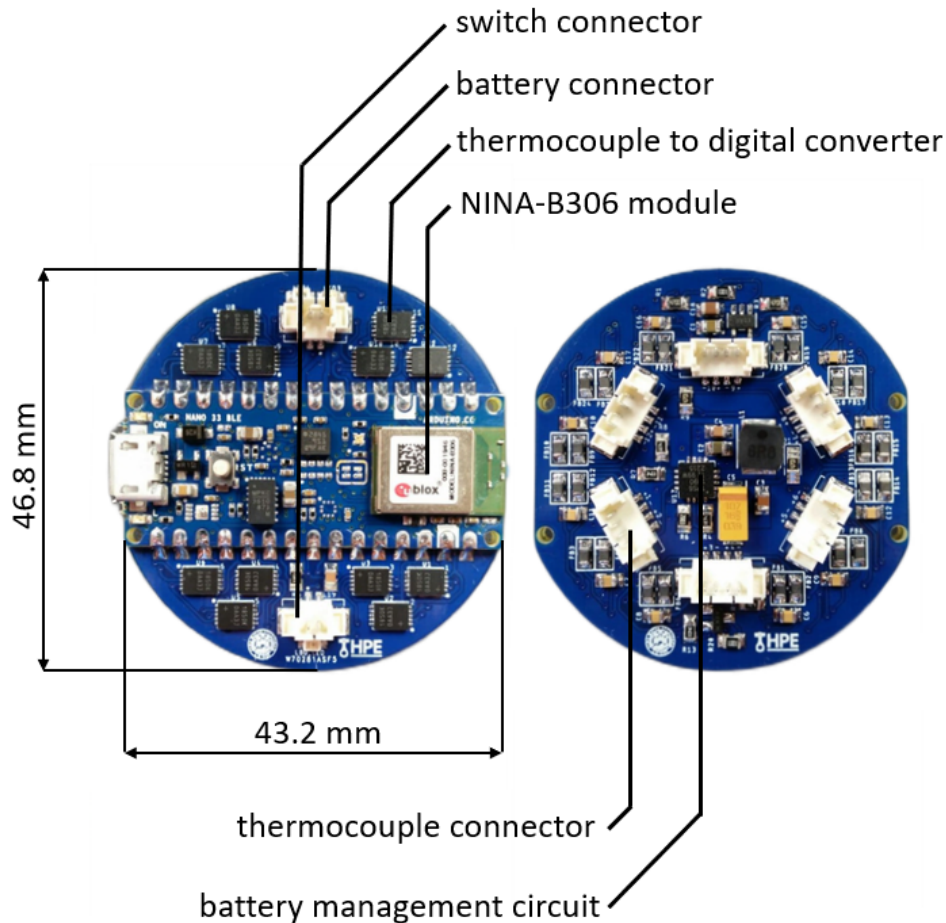


Figure 3.6: Top and bottom side of the first prototype. [©2021 IEEE]

In order to validate the prototype, several tests were performed. The first one, carried out in a Galli Genviro 060 climatic chamber [28], was the validation of the accuracy of the system. The result obtained from 12 connected thermocouples (Fig. 3.7) respects the accuracy declared ($\pm 2^\circ\text{C}$) in the MAX31850 thermocouple to digital converter datasheet. However, considering that the climatic chamber used doesn't reach temperatures above 180°C , a second test was performed (Fig. 3.8) in order to validate a characterisation of the system up to 250°C (a temperature that has to be handled by the measuring device since it is built for an electric motor). The second test was carried out in a Carbolite Gero AX 30 laboratory oven [135]. The measurement system was tested at different temperatures in the range from 40°C up to 250°C . The Fig. 3.8 shows the result performed at incremental temperatures from 150°C to 250°C . From the figure it seems that the accuracy is lower, but this is mainly due to the oven performances, that guarantee (from documentation) a

temperature uniformity of 5°C at 250°C .

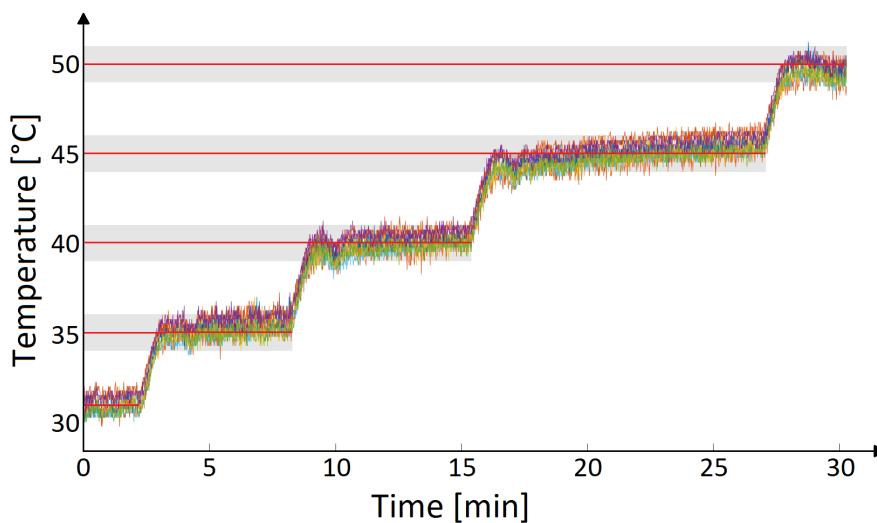


Figure 3.7: The climate chamber accuracy test. Red line, climate chamber target temperature. Grey band, $\pm 1^{\circ}\text{C}$ than target. [©2021 IEEE]

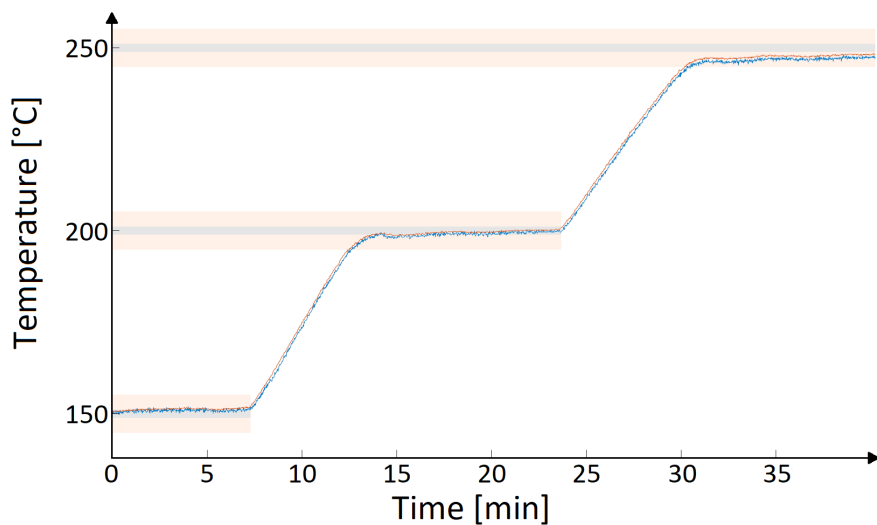


Figure 3.8: The high temperature validation test performed in a Carbolite Gero AX 30 laboratory oven (with a temperature uniformity of 5°C at 250°C). Grey band, $\pm 1^{\circ}\text{C}$ than target. Orange band, $\pm 5^{\circ}\text{C}$ than target. [©2021 IEEE]

Following the precision and accuracy analysis, the main objective was to understand if the system is able to dynamically follow a typical temperature trend during the electric motor test. More specifically, a winding heating and cooling cycle, similar to the ones obtained from simulations based on a concentrated parameter model implemented in Simulink and experimental tests provided by HPE COXA (as shown in the upper plot in Fig. 3.9), was emulated and the temperature measured with the proposed system (lower

plot in the figure Fig. 3.9). It is clear that the system correctly tracks temperature in the whole temperature range.

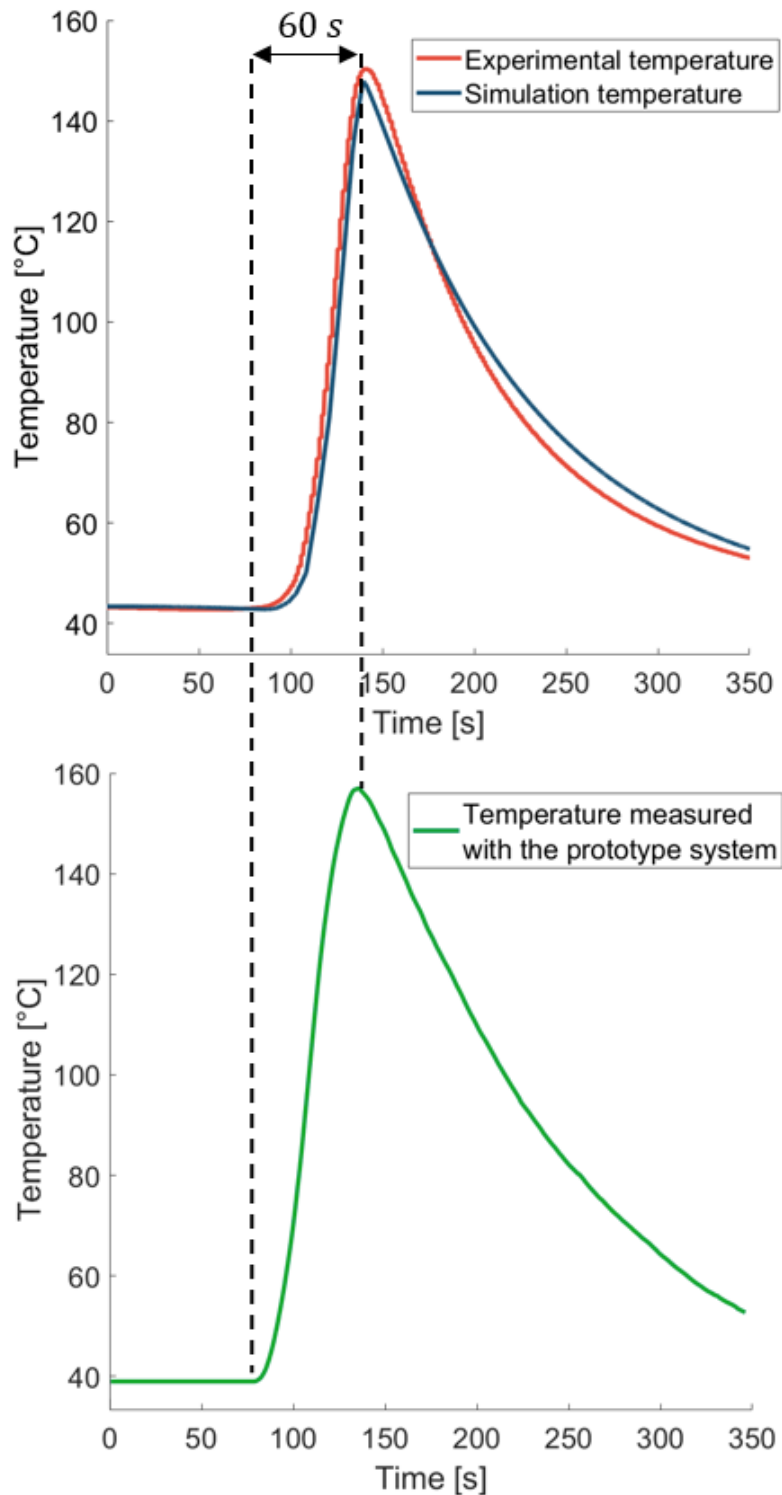


Figure 3.9: Upper plot, typical temperature trends obtained from simulations (blue line) and from experiments (red line). In the bottom plot, a sample acquisition of the temperature profile performed with the novel system is displayed (green line). [©2021 IEEE]

It is interesting to observe how fast the temperature growth is in the graphs. This is

due to the fact that the measurement point is in direct contact with the end windings, while there is no direct contact with the cooling circuit, as indicated in the Fig. 3.10.

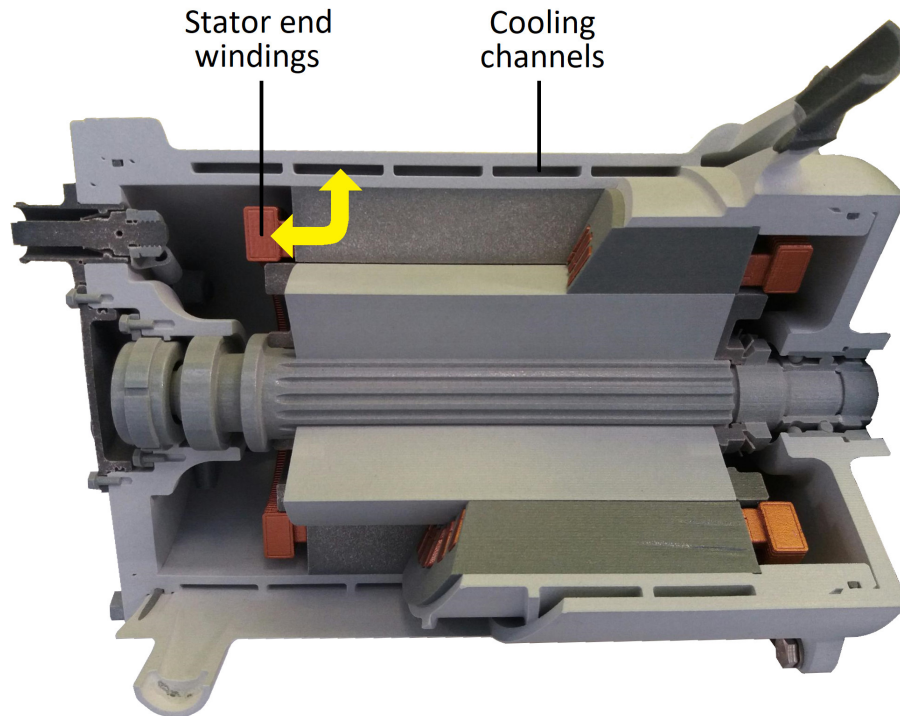


Figure 3.10: A 1:1 scale 3D printed motor model where is clear that the end windings are not in direct contact with the cooling circuit (as one might mistakenly conclude looking only at Fig. 3.5). [©2021 IEEE]

Regarding the sampling rate, the choice was 1 Hz. This was dictated by requests from the company's computing departments. Besides this, the MAX31850 interfaces [136] are also relatively slow. The datasheet gives a typical conversion time of 72 ms with maximum values up to 100 ms). These high conversion times are justified by the fact that the interface performs three actions at each measurement: temperature measurement at the hot junction, temperature measurement at the cold junction and error analysis. For 12 thermocouples this would mean that even a sampling rate of 1 Hz would be difficult to achieve, since $12 \cdot 72 \text{ ms} = 864 \text{ ms}$. Fortunately, it was noted from the experimental measurements that the situation changes if the command is sent in broadcast over the 1-Wire bus to a number of thermocouples greater than 1. In this case the total time taken is not 864 ms as mentioned above, but around 170 ms for 12 thermocouples, as shown in Fig. 3.11.

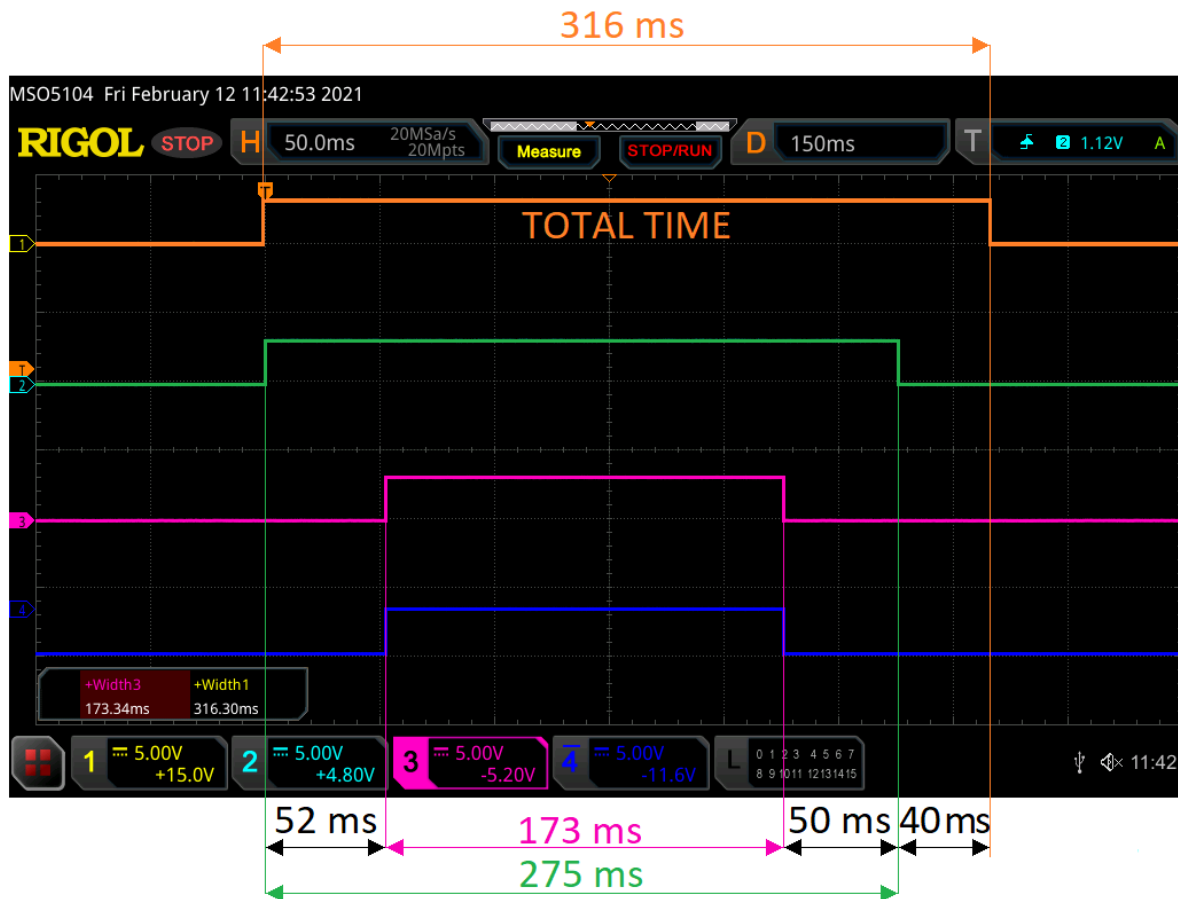


Figure 3.11: Digital timing diagram of the presented system, from top to bottom:

- orange line is high when the Terminal (see Fig.3.1) command arrives on the Station Board VCOM and low when the answer is sent back to the Terminal,
- green line is high when the Station Board forwards the command via BLE to the Sensing Board and low when the Station Board receives the response from the Sensing Board via BLE,
- pink line is high when the Sensing Board receives the command via BLE and low when the Sensing Board sends the response via BLE,
- blue line is high when the sensing board starts acquiring from thermocouples and low when the sensing board stops acquiring from the thermocouples. [©2021 IEEE]

3.1.4 Considerations

Thanks to the test aforementioned the prototype was validated and its use at the test bench started. This use permitted to analyze the strength of the Sensing Board up to 20 000 rpm, without any problem so approving the symmetrical circuit design and its case anchored to the motor shaft. Moreover, at the test bench this measurement system started to help HPE COXA in further development of a new kind of electric motor.

Meanwhile, with HPE we started to think to an advanced version. The intent was to bring the electronic inside the motor to benefit of the temperature monitoring not only in motor development phase (*e.g.* at test bench), but in real-time during its normal operation too. This new design is explained in the next section.

3.2 Final design

In the vast majority of solutions proposed in literature, the data acquisition system was placed outside the shaft so as not to affect the design of the internal parts of the motor. Conversely, the approach presented in this paper consists in including the rotor electronics inside the shaft. This solution provides several advantages along with some additional complications in the design phase.

- Advantages:
 - System compactness;
 - The displacement of all masses related to the PCB within the bearings, making the solution much more stable and robust both statically and dynamically;
 - No need of designing an additional external structure that holds the PCB.
- Drawbacks:
 - Difficulty in accessing the PCB after motor assembly;
 - Considerably higher operating temperatures for the PCB;
 - More difficult wireless data transmission;
 - Battery usage is not recommended.

Considering the specific use case, involving a compact high-performance motor with rotational speeds above 20 000 rpm, the advantages of the completely embedded solution are remarkable.

Furthermore, the project described in this paper also aims to develop a basic Acquisition Board (former Sensing Board) that will enable sensorization to be integrated into any motor developed by HPE COXA in the future. These necessities lead to:

- The need to easily change the number and type of sensors installed;
- The ability to perform real-time processing to avoid the problems associated with bandwidth limitations at high acquisition frequencies.

The requirements just mentioned can be summarized in the need for great flexibility in terms of available power.

3.2.1 Design

The architecture of the acquisition system changed a little bit than the previous version and is composed by two main parts, an Acquisition Board (former Sensing Board) and a Communication Board (former Station Board) as shown in Fig. 3.12. The Acquisition Board is placed inside the rotor, as shown in Fig. 3.13, while the Communication Board is mounted outside of it. Other remarkable changes regard the power supply for the motor side board (no battery, but Wireless Power Transfer), 6 thermocouples instead of 12 (by the first prototype analysis 6 measuring points are enough), CAN bus communication and new electronic components for the following reasons.

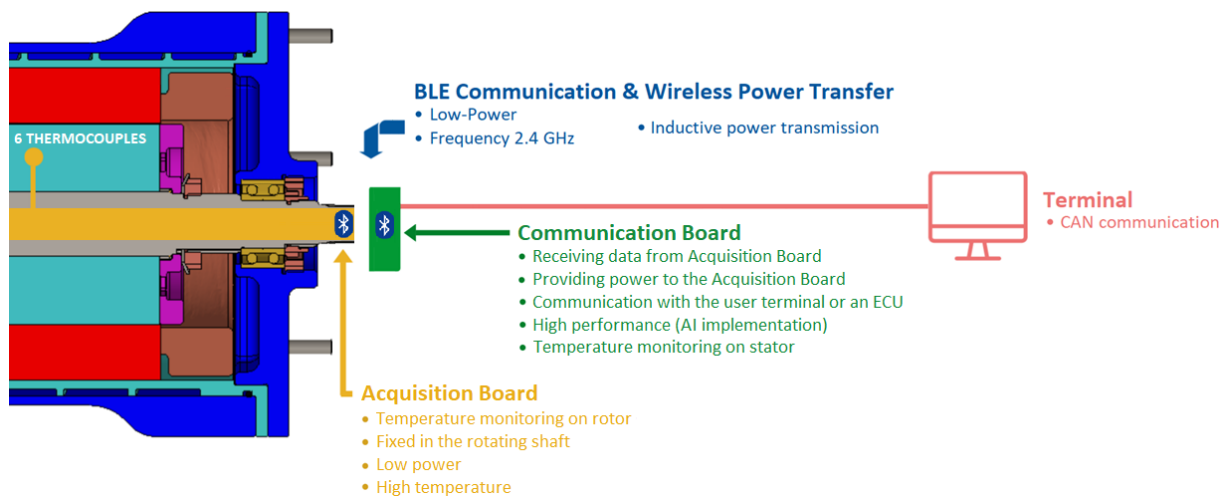


Figure 3.12: New architecture proposed. [©2022 IEEE]

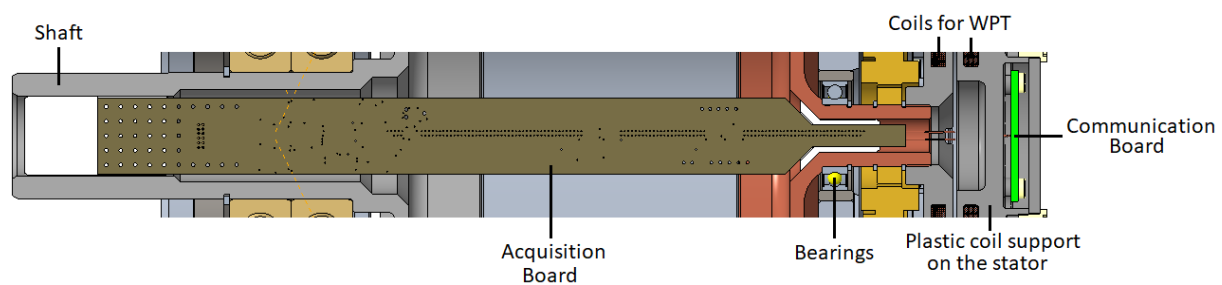


Figure 3.13: The integration of the PCB into the shaft. [©2022 IEEE]

By placing part of the electronics inside the rotor, there are two important issues that need to be addressed: the communication between the boards and the power supply of the rotating one. The data over power technology may solve both problems at once. In this perspective, the NFC protocol was tested overcoming the doubts raised in the first design due frequency range and highlighting limitations related to the flexibility of the designed system. However, the flexibility of the system is a key parameter of this project, since it must be:

- Easily adaptable to all motors produced by HPE COXA (limited design changes such as the shape of the PCBs);
- Able to accommodate various sensors on board.

The NFC protocol does not provide the same amount of transmitted power as a dedicated WPT system, leading to a limitation in the choice of electronic devices (*e.g.*, microcontroller, sensors) on the Acquisition Board. In addition, the data throughput of the NFC protocol is much lower than that of BLE, and this could become a limit when choosing to mount sensors different from thermocouples. All these considerations led to a final choice: a system that will still use the Bluetooth Low Energy protocol for communication and an inductive power transfer system for power supply.

The selected power supply system is capable to provide more than 300mA @ 3.3V. This is enough to power up a STM32WB35CE Microcontroller Unit (substitute for module NINA-B306), which is placed on the Acquisition Board and coordinates the rotor temperatures acquisition along with the transmission of such data to the Communication Board. This STM MCU is a dual processor solution, that embeds a powerful Arm-Cortex-M4 (for data acquisition and data analysis) along with an Arm-Cortex-M0+ dedicated to the BLE communication. In addition, as outlined in Figure 3.14 and shown in Figure 3.15 the Acquisition Board also integrates:

- 6 K-type twisted PFA insulated thermocouples with a temperature range from -75°C to 250°C and a conductor diameter of 0.2 mm;
- 6 MCP96L01 thermocouple-to-temperature converters with a typical accuracy of $\pm 2^{\circ}\text{C}$ that integrates cold-junction compensation as well as an open-circuit and short-circuit detection. The communication between the converter and the microcontroller is based on the I²C protocol and not a 1-Wire link;
- 1 MAX31889ALT+ temperature sensor (with an accuracy of $\pm 0.65^{\circ}\text{C}$ from -40°C to 125°C) for PCB and other components temperature monitoring;
- 2 LM95071-Q1 temperature sensors (with an accuracy of $\pm 2^{\circ}\text{C}$ from -40°C to 150°C) for PCB temperature monitoring and heat dissipation research activity;
- 1 Harwin Gecko connector for thermocouples connection;
- 1 MAX25231 switching voltage regulator for 3.3V that is necessary for the power supply.

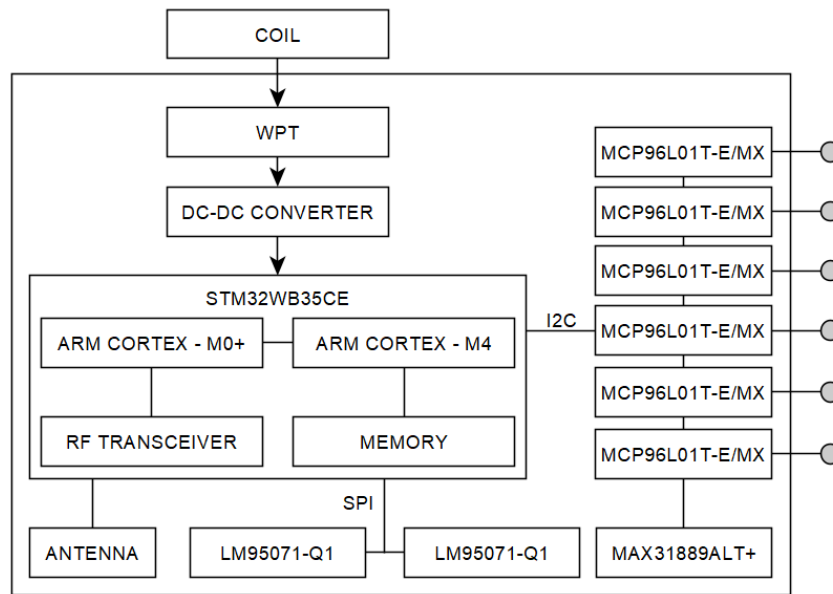


Figure 3.14: Acquisition Board architecture scheme. [©2022 IEEE]

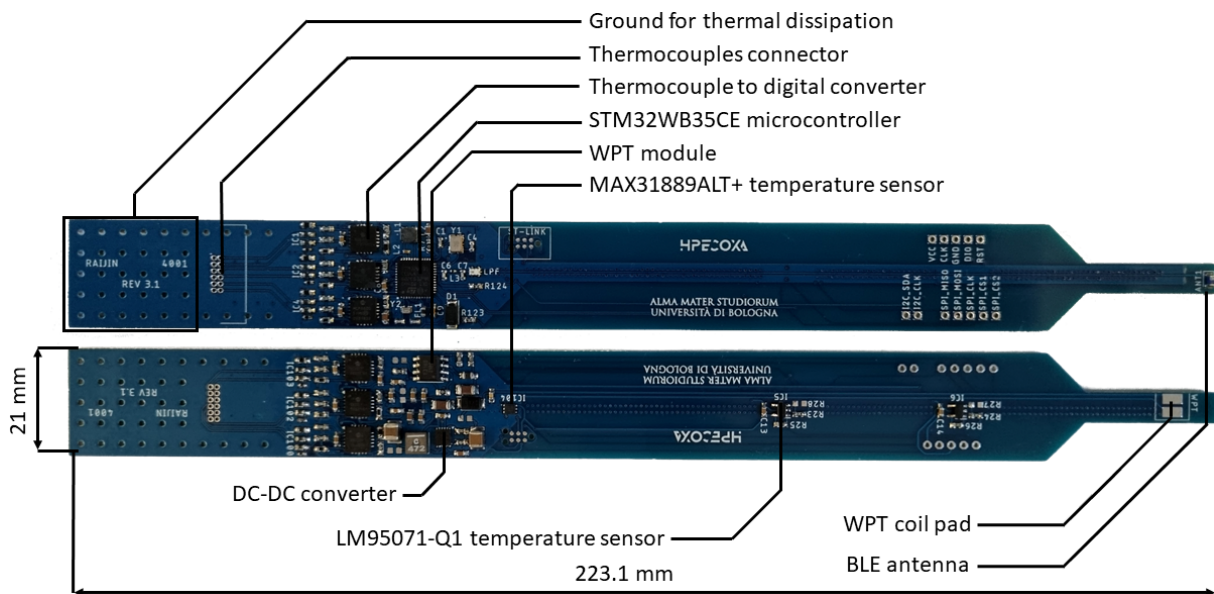


Figure 3.15: Top and bottom side of the first prototype of the Acquisition Board. [©2022 IEEE]

The Communication Board features some similarities and differences with the Acquisition Board. The MCU, the thermocouple-to-temperature converters, the MAX31889ALT+ temperature sensor and the RF parts are hosted in both boards since they share some tasks, such as temperature measurement and BLE communication. Despite this, there are also some differences related mainly to the fact that the Communication Board must also manage the communication with the test bench. For this purpose the board integrates the MCP2518FD CAN FD controller with SPI interface and the ATA6562/3 transceiver as

shown in Fig. 3.16. Furthermore, in order to provide the power supply to the Acquisition Board, the Communication Board incorporates also the Wireless Power Transfer module.

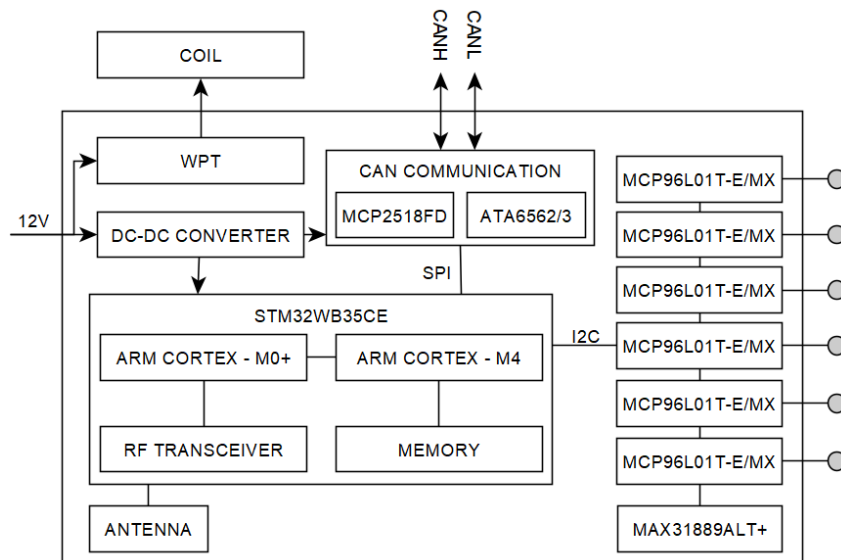


Figure 3.16: Communication Board architecture scheme. [©2022 IEEE]

The following table 3.2 summarizes the main features of the new realized system. It is worth noting that even if this system has been realized for the acquisition of temperatures only, additional sensors (*e.g.*, strain gauges) could be integrated as well.

Table 3.2: Measuring system specifications.

Feature	Communication	Acquisition
	Value	
Temperature Sensor	Thermocouple Type K	
Measuring range	0 – 250 °C	
Resolution	0.0625 °C	
Accuracy	±2 °C (typ.) and ±4 °C (max.)	
Channel	6	6
Connectivity	CAN FD	BLE
Power supply	12 V	WPT

3.2.2 Installation

The acquisition system illustrated in this paper was installed on a high performance IPM motor designed and mounted by HPE Coxa in Modena. It's a new varian than

the one used for the previous monitoring system and suitable to host in motor shaft the Acquisition Board (see Fig. 3.13). During the design and installation of the electronics we needed to reassess several critical aspects due by new board shape and different location:

- **High rotational speed:**

The rotor can reach speeds above 20 000 rpm and so unwanted vibrations need to be avoided. For this reason, the Acquisition Board was designed to be as symmetrical as possible. The electronic components have been placed close to the rotational axis to reduce the rotational stress to which they will be exposed. Moreover, a resin treatment has been done in order to limit the vibrational stress of the components. Also, the first prototype has been tested up to 20 000 rpm, proving the reliability of the BLE protocol up to these rotational speeds.

- **High operating temperature:**

Although there are no heating sources in proximity of the board, it is still affected by the high temperatures reached in the stator windings (over 160 °C) and magnets (over 150 °C). This heat spreads around the motor reaching also the internal part of the rotor, where the Acquisition Board is placed. In the past version an issue not handle, because the electronics was external.

The internal temperatures predicted by simulations under the most extreme conditions¹ (not yet reached experimentally) exceeds 105 °C. These values are already critical for most electronic components. For this reason, the maximum operating temperature of each component was one of the key parameters during the components selection. Additionally, the components that are most susceptible to temperatures has been placed on the colder side of the PCB (*e.g.*, the DC-DC converter is placed in an area that almost never exceeds 120 °C and the component can operate at a junction temperature of 150 °C for 5000 hours ensuring a certain margin of safety), by the simulation reported in Fig. 3.17. In particular, all the components chosen for the board are capable to reach 125 °C, with the only exception of the microcontroller, that is only rated up to 105 °C. The microcontroller choice has been dictated by the current semiconductor crisis, which makes the availability of high temperature packages hard to obtain for most of the components on the market. To reduce the risk of microcontroller wearing, the Communication Board has the possibility to power down the wireless power transfer (when certain temperature thresholds are exceeded), shutting down the Acquisition Board.

- **Unequal temperature distribution in the shaft:**

¹Simulations were performed in an extreme worst case scenario that should not be encountered during the normal operation.

In order to optimize the heat dissipation a thermal simulation was performed. As Fig. 3.17 shows, the temperature distribution is not uniform, highlighting how the left side of the shaft is cooler than the right side. Therefore, to maximize the heat dissipation, the PCB was designed with a large ground plane on the colder side (as indicated in Fig. 3.15). Notice that the simulation result refers to a critical overload out of the motor operating condition. Nevertheless, such a result provides a reference for the maximum theoretical temperature distribution along the PCB.

- **Static and dynamic stability of the system:**

In order to achieve the maximum stability inside the shaft, two plastic supports have been designed with the aim of keeping the board integral with the shaft.



Figure 3.17: Temperature distribution in the shaft in upper limit temperature condition. [©2022 IEEE]

3.2.3 Development and test

The development of the prototype has been carried out keeping in mind the critical issues mentioned above, such as high rotational speed and high operating temperatures. As shown in Fig. 3.15, the shape was chosen in order to minimize the width and maximizing symmetry. Furthermore, plastic supports have been developed to anchor the PCB at both ends, in order to prevent vibrations that can lead to mechanical failures.

To take into account the unequal temperature distribution inside the shaft showed by the simulations, three additional temperature sensors have been placed along the PCB (displayed in Fig. 3.15) in order to validate the simulation seen in Figure 3.17. The collected data are not relevant for analyzing the motor performance, but are very important to understand the operating conditions of electronic components.

Regarding metrological aspects, the system was validated in terms of throughput and accuracy. In particular, experimental evidence showed that it is possible to achieve a sampling time of less than 4 ms with a resolution of 12 bits. Considering that there are 6 thermocouples on the I²C bus, this means that the sampling rate of the whole system is around 24ms. Comparing the results with the previous experiments done with the previous system this represents a 10x improvement (from 316 ms to less than 30 ms).

As far as the accuracy is concerned, it was validated performing two different tests:

- The first test was conducted to ensure the accuracy of the temperature measurements over the whole range of thermocouples operation, which largely exceeds the temperature peaks (estimated by simulations) at the measurement points. The test was performed in a Carbolite Gero AX 30 laboratory oven [135]) (with a temperature uniformity of 5 °C at 250 °C). The temperature measurements were tested in the range from 50 °C up to 250 °C. The Fig. 3.18 shows that the system is able to track temperatures from 50 °C up to 250 °C with an error that never exceeds ± 5 °C, i.e. in the range of the oven temperature accuracy reported by datasheets.

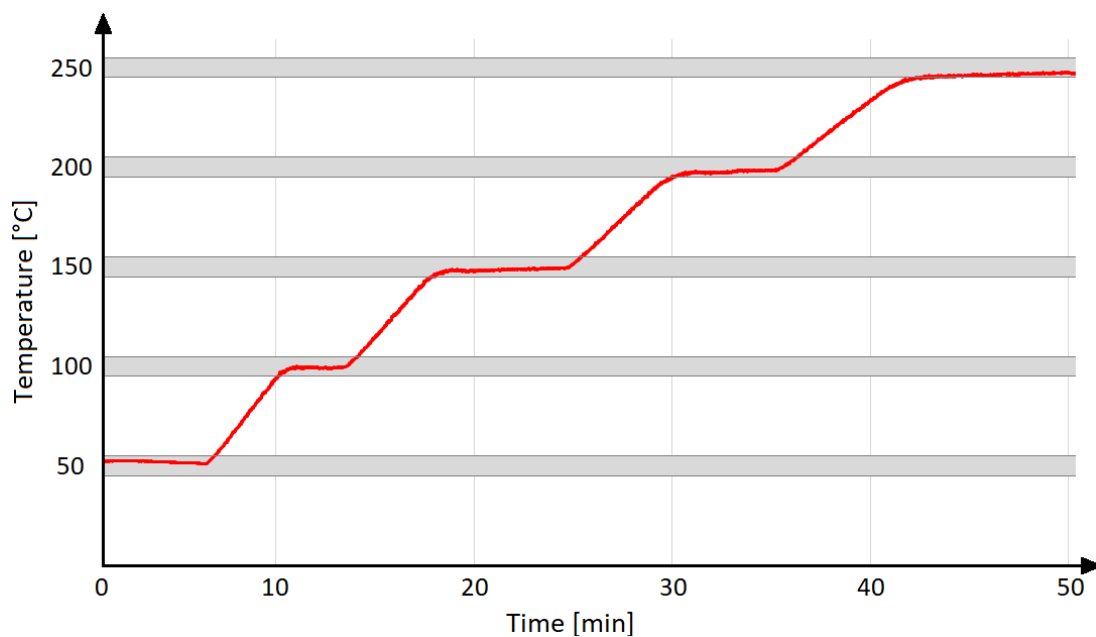


Figure 3.18: The accuracy validation test performed in a Carbolite Gero AX 30 laboratory oven prove that the thermocouples used are accurate from 50 °C up to 250 °C. [©2022 IEEE]

- The second test was performed in order to verify how the measurement is affected by the temperature variations of the PCB with all the electronics. For this purpose the PCB was placed in a climatic chamber [28] keeping the thermocouples outside the chamber at a fixed temperature. From the obtained results (shown in Fig.

3.19) it can be seen how the variations are negligible, and the measurement remains accurate even by varying the temperature of the Acquisition Board.

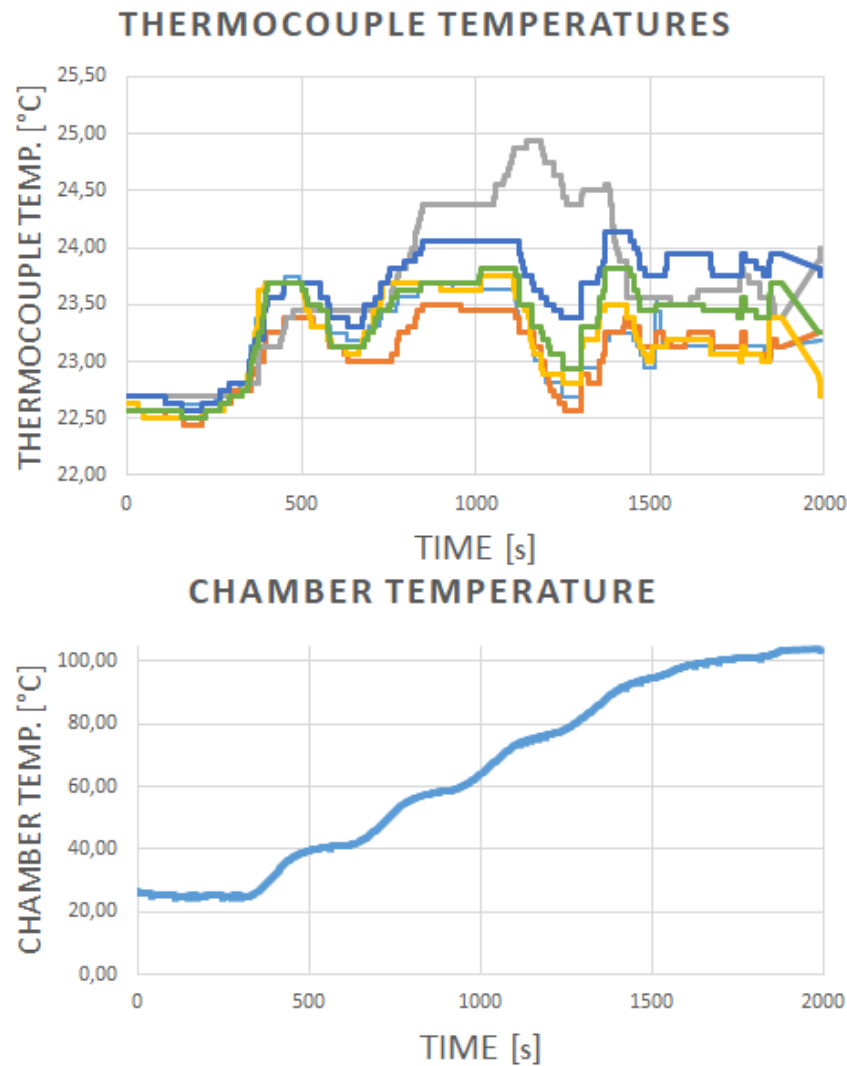


Figure 3.19: Climate Chamber data. The upper plot shows temperatures measured by the thermocouples placed outside the chamber while the electronics was kept inside the chamber at a rising temperature (lower plot). All x-axis are reported in seconds. [©2022 IEEE]

3.3 Conclusions

The presented investigation has led to the study and development of a temperature monitoring system for compact-size and high-rotating-speed electric motors. The conference paper describing such novel technology was awarded with the third place in best paper competition at the IEEE 2022 Metrology for Automotive conference.

The system described represents an embedded data Acquisition Board suitable for heterogeneous sensors. Future developments include the integration and interfacing with other sensors, like strain gauges, in order to perform research activities also on the mechanical parts which are critical in high performance motors.

The cost of the electronic part of the measurement system is relatively low, especially when compared to the cost of the motor itself. Approximately, for both prototypes the cost ratio is around 200€ for the electronic measurement system, over 25.000€ for the HPE electric motor. The main costs associated to the proposed systems are related to the necessity of manufacturing a modified shaft for thermocouples installation. For this reason, future developments include the definition of procedures to infer the rotor temperature from measurements conducted on the stator. In the near future, AI algorithms may be implemented (based on the dataset collected) in the embedded system, since the MCU mounted are powerful enough to perform inference on a neural network. For example, Convolutional Neural Networks can be used to estimate sensors value. This can lead to the removal of sensors that are harder to install (which can reduce the motor costs), or even to predict wear in the system by comparing estimations with actual data.

As anticipated, any further details on IPM motor used can't be disclosed, not even on the electronics housing, because the technology is currently submitted for patent application.

Chapter 4

Structural Health Monitoring

Abstract

This last Chapter is dedicated to the main topic of my PhD. The research in developing increasingly high-performance devices in a field such as Structural Health Monitoring meets great and intriguing challenges. Such challenges must be tackled with cutting-edge technologies. Among these, extreme-edge computing is becoming increasingly appealing for SHM applications because it allows the optimal management of the available processing resources. This fosters the possibility to enhance the responsiveness and ease the power management of the inspection system. However, to implement this near-sensor processing, the design of an optimized hardware is fundamental.

Introduction

Many sensor solutions for SHM applications have been developed in literature, including the Smart Sensor Network (SSN) developed within the Intelligent Sensor Systems Lab of the University of Bologna [137, 138].

One of the critical tasks for these networks is data management. This task became particularly crucial with the development of mesoscale SHM systems, where the periodic gathering of signals from increasingly denser sensor networks made the data management task a primary issue. In the specific context, industrial facilities and aging structure size is one of the most relevant parameters to be taken into account when designing integrity assessment networks; at the same time, the sensor density must be compatible with fine-grained damage localization [139].

Additionally, a crucial point in the deployment of effective Structural Health Monitoring systems concerns the real-time and long-lasting functionality of the underlying sensor network. Indeed, the wide adoption of full-scale monitoring solutions is hampered by factors such as the amount of data to be acquired, the necessity to avoid network congestion

through smart data management and the limited power budget to enable autonomous functionalities.

To account for these constraints, a new SHM paradigm inspired by the Compressed Sensing (CS) theory is investigated in this study. CS allows to implement cost-effective and energy-aware solutions capable to extend the sensors' life-cycle. In particular, CS jointly optimizes data sampling rates, on-board storage requirements, and communication data payloads. Focusing on the vibration-based SHM field, structures in dynamic regime present characteristic frequency patterns [140] where the total structural energy is concentrated in few and highly localized harmonic components. The sparse profile of the recorded signals in the frequency domain makes CS strategies applicable and appealing. Once vibration waveforms have been recovered on the basis of the selected CS implementation, the classical modal analysis procedures can be applied for modal parameter estimation, including the extraction of natural frequencies of vibration and the corresponding modal shapes [141].

In scientific literature, successful on-board vibration diagnostics has already been reported. Among the significant works, a customized version of the Imote2 sensor platform was presented in [142], proving to be effective for the on-line structural assessment of long-span structures. Similarly, authors in [143] employed the Narada wireless sensor as a prototyping board for acceleration compression in the framework of bridge assessment. Moreover, a hardware-oriented alternative was presented in [144], which deals with a distributed and on-line adapted compression approach to better capture the non-stationary response of real use-cases. At the beginning of this chapter, we exploit the SSN made in University of Bologna to implement CS strategies in vibration monitoring. In addition, several examples of compression/decompression stages performed on remote stations or dedicated servers are present in literature; conversely, effective on-board implementations of CS techniques are rarely described. This is why has been interesting deal the practical aspects related to the definition of the most suitable data recovery algorithms. Three different strategies are compared in terms of computation time, memory requirements, and accuracy of the reconstructed vibration signals.

Besides, the SSN used for CS experimentation has also been used for an European Project: Arrowhead Tools [145]. The IoT landscape, and the adoption of poor architectural solutions often make it difficult to integrate third-party devices in a seamless way. In the Arrowhead Tools project, we tackle these issues by proposing a tool-driven architecture that supports heterogeneous sensor management through well-established interoperability solutions for the IoT domain, i.e. the Eclipse Arrowhead framework and the recent Web of Things (WoT) standard released by the W3C working group. We deploy the architecture in a real SHM scenario, which validates each developed tool and

demonstrates the increased automation derived from their combined usage.

In parallel to these activities related to the efficient usage of the SSN, the implementation of a new generation of SHM monitoring network was studied. The network is no longer based on wired devices, but on wireless communications, and it is also characterized by various hardware upgrades addressing high-performance edge processing and monitoring features. In addition, this new sensor network features the implementation of a different approach to data management w.r.t. CS, i.e. the System Identification (SysId) algorithm. This Chapter will show how this algorithm is one of the most powerful means for dynamic systems analysis and, consequently, for vibration-based structural assessment.

Last but not least, it has been considered an Artificial Intelligence approach to SHM. Despite the outstanding improvements achieved by artificial intelligence in the SHM field, some challenges need to be coped with. Among them, the necessity to reduce the complexity of the models and the data-to-user latency time which are still affecting state-of-the-art solutions. This is due to the continuous forwarding of a huge amount of data to centralized servers, where the inference process is usually executed in a bulky manner. Conversely, the emerging field of Tiny Machine Learning (TinyML), promoted by the recent advancements by the electronic and information engineering community, made sensor-near data inference a tangible, low-cost and computationally efficient alternative. In line with this observation, this work explored the embodiment of the One Class Classifier Neural Network (OCCNN), i.e., a neural network architecture solving binary classification problems for vibration-based SHM scenarios, into a resource-constrained device. Therefore, without the use of the cited SSN, or the solution proposed above, but the test on a third platform devoted to TinyML application the Arduino Nano 33 BLE.

The remainder of this chapter is organized as follows. The basics of CS and related recovery algorithms are recalled in Section 4.1 to provide a theoretical introduction. Then, the core elements of an ad-hoc designed SHM architecture are presented in Section 4.1.3, hence discussing how the data compression and reconstruction tasks could be efficiently distributed in presence of a clustered network topology. The distinguishing features of the hardware and software components are coherently detailed. Section 4.1.4 follows, which presents the experimental validation, whilst conclusions are drawn at the end. In addition, the same Smart Sensor Network used for CS in Section 4.2 is deployed in an IoT toolchain architecture. Then, a different data management and structures evaluation approach based on System Identification is presented in Section 4.3, as well as new hardware solution to host such processing, then validation and results are reported. Lastly, the Section 4.4 outlines the use of TinyML technique with hints of theory and practical

implementation of an OCCNN processing processing a big experimental dataset.

The content of this Chapter is based upon the research works [P8, P9, P10, P11, P12]:

- “Compressive Sensing and On-board Data Recovery for vibration-based SHM” by Zauli M., Zonzini F., Testoni N., Marzani A. and De Marchi L. in European Workshop on Structural Health Monitoring: Special Collection of 2020 Papers-Volume 1, pp. 327–334, 2021. ©EWSHM 2020. Springer, Cham¹.
- “A Novel Smart Sensor Node with Embedded Signal Processing Functionalities Addressing Vibration-Based Monitoring” by Zauli M., Zonzini F., Coppola V., Der-timanis V., Chatzi E., Testoni N. and De Marchi, L. in European Workshop on Structural Health Monitoring: EWSHM 2022-Volume 3, pp. 1–6, 2022. ©EWSHM 2022. Springer, Cham².
- “Hardware-Oriented Data Recovery Algorithms for Compressed Sensing-Based Vibration Diagnostics” by Zonzini F., Zauli M., Carbone A., Romano F., Testoni N. and De Marchi L. in Applications in Electronics Pervading Industry, Environment and Society: APPLEPIES 2020 8 (pp. 69-75). Springer International Publishing.
- “Enhancing Vibration-Based Structural Health Monitoring via Edge Computing: A Tiny Machine Learning Perspective” by Zonzini F., Carbone A., Romano F., Zauli, M. and De Marchi L. in Quantitative Nondestructive Evaluation. American Society of Mechanical Engineers, 2021. p. V001T07A004.
- “An IoT Toolchain Architecture for Planning, Running and Managing a Complete Condition Monitoring Scenario” by Montori F., Zyrianoff I., Gigli L., Calvio A., Venanzi R., Sindaco S., Sciullo L., Zonzini F., Zauli M., Testoni N., Bertacchini A., Londero E., Alessi E., Di Felice M., Bononi L., Bellavista P., De Marchi L., Marzani A., Azzoni P. and Cinotti T. S. in IEEE Access, 2023.

From which part of the text is drawn. Concerning hardware, I completely designed and implemented the Wireless Sensor Network (used for SysId study), both hardware and software. Concerning software, I developed the firmware for the embedded system itself, and also the Cluster Head software (a Personal Computer, or Single Board Computer) with

¹Adapted by permission from Springer Nature Customer Service Centre GmbH: Springer Nature, Lecture Notes in Civil Engineering, Compressive Sensing and On-board Data Recovery for vibration-based SHM, ©2021.

²Adapted by permission from Springer Nature Customer Service Centre GmbH: Springer Nature, Lecture Notes in Civil Engineering, A Novel Smart Sensor Node with Embedded Signal Processing Functionalities Addressing Vibration-Based Monitoring, ©2022.

the programming of Matlab, and Python tools. Concerning the on-board processing I gave my support in the study of CS compression and decompression, programming the data gathering part for the SysId task, and I participated in the TinyML study (investigation of the Arduino board, Tensor Flow framework and Colab training and modelling).

4.1 Compressive Sensing

4.1.1 Basics

Two main ingredients are required to make the CS paradigm applicable: on one hand, the existence of a basis $\Psi \in \mathbb{R}^{N \times N}$ in which the class of processed signal is supposed to be sparse, i.e. $x = \Psi c$ where only $M \ll N$ significant coefficients can be found after a signal projection stage is applied. On the other hand, the existence of a sensing matrix $A \in \mathbb{R}^{M \times N}$ which performs the actual dimension reduction operation.

Once Ψ and A have been determined, the CS processing flow encompasses the three following steps:

1. *Compression*: given a generic signal instance $x \in \mathbb{R}^{N \times 1}$, its compressed form $y \in \mathbb{R}^{M \times 1}$ can be computed according with the matrix–vector multiplication

$$y = Ax \tag{4.1}$$

2. *Sparse coefficients recovery*: assuming that the estimation of the original signal samples can be treated either as an iterative or optimization–based problem, a wide number of algorithms were proposed, taking advantage of the underlying sparsity condition [146] to estimate the sparse coefficients \hat{c} . Independently of the fitness function of the specific algorithm, the common objective of each method is to recover \hat{c} by satisfying some prescribed criteria.
3. *Decompression*: a good approximation \hat{x} of the original data can be straightforwardly computed by projecting back the sought sparse coefficients in the time domain, i.e.

$$\hat{x} = \Psi \hat{c} \tag{4.2}$$

As far as the behavior of structures in dynamic regime is concerned, Fourier bases are conventionally exploited since the structural vibrations are sparse in this domain [147]. At the same time, even if a wide range of strategies exists for designing the optimal sensing matrix, Gaussian matrices, i.e. matrices where each entry is taken from a normal distribution, are effective in the vibration analysis field, paving the way to fully unsupervised CS approaches [148]. Accordingly, the Discrete Cosine Transform (DCT) matrix and the classical Gaussian matrix sampled from a standard normal distribution are employed in this work as sparsity and sensing matrix, respectively.

4.1.2 Data recovery algorithms

The implementation of the data recovery algorithm must meet the computational and storage resources of the monitoring network. The best trade-off between algorithmic complexity, memory storage, and retrieved signal accuracy is to be pursued. In this work, we concentrate on iterative solutions due to their faster convergence: this property is essential in real-time inspection scenarios where the latency due to mere processing should be kept to the minimum. In particular, three main approaches were considered worthy of investigation [146]:

- (i) *Orthogonal Matching Pursuit (OMP)*: considered as one of the most effective serial greedy strategies, the rationale behind this procedure is to update the values and positions of the non-zero signal coefficients step-by-step by exploiting a least-square method.
- (ii) *Compressive Sampling Matching Pursuit (CoSaMP)*: overcoming the main limitations given by the sequential approach at the basis of OMP, CoSaMP jointly refreshes all the non-null entries by refining at each iteration their value in the direction of the minimum residual error.
- (iii) *Iterative Hard Thresholding (IHT)*: in its essence, IHT is similar to CoSaMP, the main difference being related to the exploitation of a thresholding operator for the simultaneous update of the estimated set of signal coefficients.

4.1.3 Proposed SHM architecture

An HW/SW architecture for SHM has been designed, in which the entailed coding and decoding procedures are implemented directly on the sensors' boards, i.e. in strict proximity where the structural information is actually sensed. As schematically depicted in Fig. 4.1, a decentralized sensor network topology is proposed, which involves multiple Peripheral Sensor Nodes (PSN, or just Sensor Node - SN) directly deployed on the structure and arranged in clusters, each of them being coordinated by a corresponding Cluster Head Node (CHN, or just Cluster Head - CH).

The advantages of such a hierarchical approach are the following: (i) the computational complexity is minimized, a condition which is ensured by the inherent cluster parallelism, i.e. the capability to retrieve local information prior than returning the full-scale structural parameters; (ii) communication congestion is avoided while the local channel availability is increased, i.e. the sensor density N_j per cluster is significantly lower than the cumulative one; (iii) the available hardware and software resources of the network

are optimally allocated, subdividing the computational task between the PSNs and their master CHN.

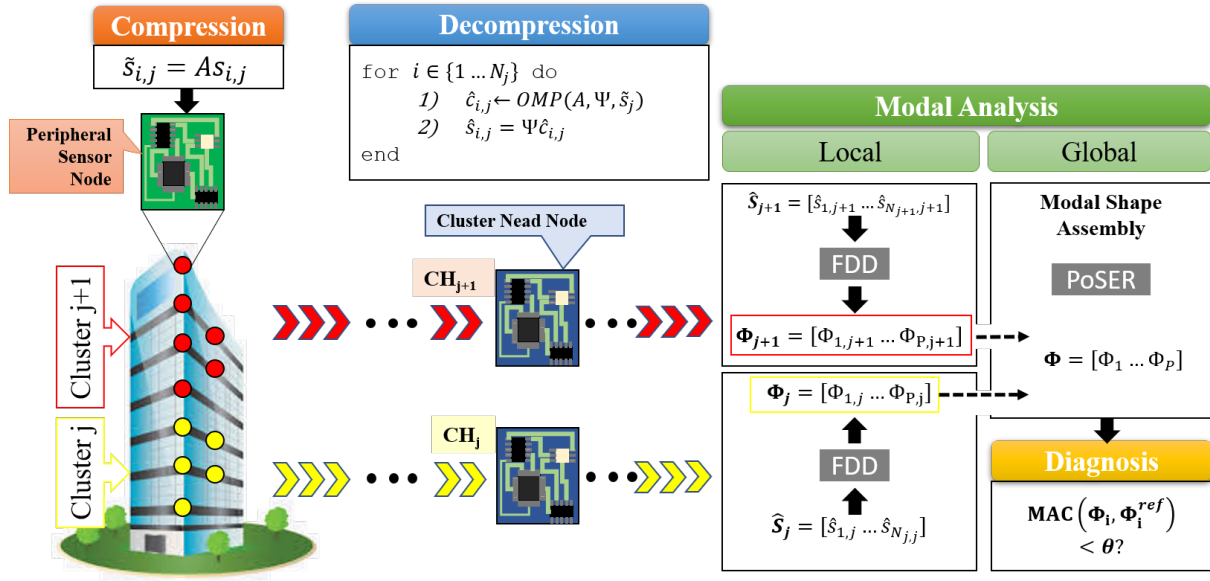


Figure 4.1: The proposed HW/SW architecture for modal analysis. From left to the right, the compression/decompression stages are allocated to the PSNs and the CHNs, respectively. Then, the pure modal analysis is performed, firstly identifying cluster-related modal shapes Φ_j and then merging the local estimates into a full-scale modal shape matrix Φ . Finally, the current health status can be derived by monitoring trends in MAC values over time.

As a main result, it is possible to reduce the latency in providing a final structural assessment and the power budget of the whole system, thanks to the combination of the streaming data processing and the limited amount of data which is exchanged through the network (i.e. only sensors' pre-processed modal features are required to be transmitted rather than the entire signal waveform).

As far as the algorithmic part is concerned, the proposed approach workflow involves the cascade of the compression/decompression stages, on top of which the pure modal identification process is stacked. Once the sensor-to-cluster assignment has been defined, the following tasks need to be accomplished:

1. *Compression*: each PSN acquires and on-board compresses vibration data, eventually returning s_i ;
2. *Decompression*: upon receiving the compressed signals $\tilde{s}_{i,j}, i \in \{1, \dots, N_j\}$, every CHN recovers the original time series from all its mastered PSNs and arranges them into a column matrix;

3. *Local Modal Analysis*: given $\hat{\mathbf{S}}_j = [\hat{s}_{1,j} \dots \hat{s}_{N_j,j}]$ the column matrix of reconstructed signals, the matrix $\Phi_j = [\Phi_{1,j} \dots \Phi_{P,j}]$ of cluster-dependent modal shape vectors $\Phi_{p,j}, p \in \{1, \dots, P\}$ is extracted by resorting to one of the available modal identification method. In particular, the Frequency Domain Decomposition method [141] is adopted in this work due to its favourable trade-off between the accuracy of the retrieved modal shape coordinates and the limited computational complexity of the underlying algorithm;
4. *Global Modal Analysis*: the full-scale modal shape matrix $\Phi = [\Phi_1 \dots \Phi_P]$ is computed by merging together local modal shape estimations Φ_j as prescribed by the PoSER [149] approach;
5. *Diagnosis*: the Modal Assurance Criterion [150] is computed between the currently estimated Φ and the reference modal shape matrix Φ^{ref} , which is thought to be representative of the structural healthy status. The final structural integrity characterization, here intended as a simple presence or absence of defects, is eventually obtained by identifying MAC reductions in equally-indexed modal shapes curves below a damage threshold $\theta = 90\%$.

4.1.4 Experimental validation

Materials

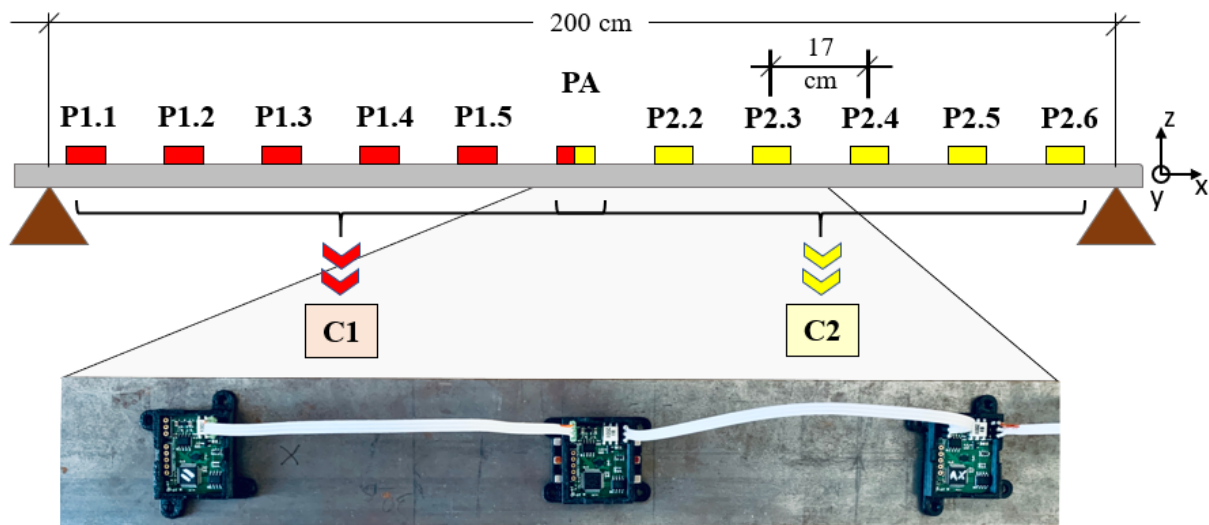


Figure 4.2: Experimental testbed and related sensor installation plan, comprising two clusters (C1 and C2, respectively) of six accelerometers. An inset depicting the practical connection of three PSNs is also enclosed.

The pinned–pinned steel beam schematically drawn in Fig. 4.2 was instrumented with a double chain of six PSNs, each of them being orchestrated by a purposely devoted CHN. Worthy to be noticed, the two clusters are overlapped in correspondence of their terminal position (position 'PA'), as requested by the PoSER algorithm.

From an electronic standpoint, the Smart Sensor Network developed within the Intelligent Sensor Systems Lab of the University of Bologna is employed, which constitute of light–weight (less than 4 g), small footprint (23 mm x 30 mm) and low-power (41 mA are absorbed in continuous mode from a 3.3 V voltage reference) sensor nodes. Each PSN is equipped with an STM32F303 microcontroller unit (MCU) which and a 6 Degree–of–freedom (DoF) Micro-electro-mechanical System (MEMS) inertial measurement unit providing both linear and angular vibration data. On the other hand, the CHN features a more powerful MCU with extended storage capabilities and embedded digital signal processing functionalities enabling for the execution of more burdensome operations. PSNs are connected in a wired daisy chain fashion by means of a Sensor Area Network (SAN) bus exploiting data–over–power communication. The complete hardware and software description of the network can be found in [137, 138] as mentioned in the introduction. Concerning the entailed CS operations, both the sensing matrix A and the DCT sparsity basis Ψ are pre–charged into the PSN/CHN node memory at the network startup since they do not need to be refreshed during the real–time monitoring phase.

Methods

A sampling rate of 200 Hz was selected to be compliant with the expected vibration behavior of the structure, whose three most energetic frequencies were predicted to lie below 50 Hz basing on closed analytic formulae (see [149]). Coherently, the parameter P was set equal to three.

Acceleration data along the z axis were acquired repeatedly over time windows of 75 s (i.e. each time series consisted of 15 000 samples), which were framed into data segment of $N = 512$ measurement values in order to be compliant with the available processing/storage capabilities of the nodes while ensuring a sufficient frequency resolution in the modal identification process. On the other hand, the number M of samples surviving after the compression stage was fixed by the compression factor $CR = N/M$, a quantity which was varied in the interval [2:10] for compression analysis. Concerning recovery algorithms, after a preliminary analysis the sparsity measure k , which is an important input parameter for the recovery algorithm, was fixed at 10.

Experiments were designed to leave the beam vibrating under ground borne vibration, so as to mimic the typical vibration conditions of operational excitation conditions.

In order to quantify the accuracy of the CS–framework, MAC index [151] was used to measure the level of modal correlation between CS–processed and uncompressed modal shape estimates. The target was to provide MAC values above the threshold $\theta = 90\%$, because such value is compatible with the subsequent assessment of the structural integrity [150].

About decompression stage the code is described in Section 4.1 was programmed in the C++ language to be compatible with the digital signal processing functionalities embedded in the sensor nodes' MCU. To this end, all the mathematical procedures and functions were purposely written without exploiting the built–in operations in order to actually customise the signal processing framework to the embedded resources of the network.

The three main metrics chosen to quantify the performance of each data recovery method are: (i) the memory footprint M , namely the total number of initialised data and temporary variables required for the complete reconstruction of a single set of coefficients \hat{c} , (ii) the running time T , i.e. the time needed to restore one single frame (which has been estimated by employing code functions measuring the elapsed time in between the start and stop of the required processing), and (iii) the Average Reconstruction Signal–to–Noise Ratio (ARSNR), which is computed off–line in a post–processing phase. The latter is conventionally used to quantify the noise levels introduced by the CS processing operations according with

$$\text{ARSNR} = 20 \log \left(\frac{\|x\|_2}{\|x - \hat{x}\|_2} \right) \quad (4.3)$$

in which $\|\cdot\|_2$ stands for the ℓ_2 norm of a vector. Finally, the Memory–per–Time–over–Accuracy (MTA) factor

$$\text{MTA} = \frac{M \cdot T}{e^{\text{ARSNR}/20}} \quad (4.4)$$

was introduced with the primary goal of providing an overall evaluation: the lower the MTA, the higher the recovery performance of the sought algorithms are. For the sake of clarity, ARSNR values were computed back in the linear scale to account for the singular values implied by the logarithmic operator, i.e. $\text{ARNSR} = 0$ or $\text{ARSNR} \downarrow 0$.

4.1.5 Results

Compression

MAC values are reported in the left panel of Fig. 4.3, superimposed to the benchmark level of 90% in order to better track the quality of the identified structural information. Beside, the three vertical charts in the right side of Fig. 4.3 refer to the different modal

components, each of them including exemplary full-scale reconstructed modal shapes for a selection of compression factors.

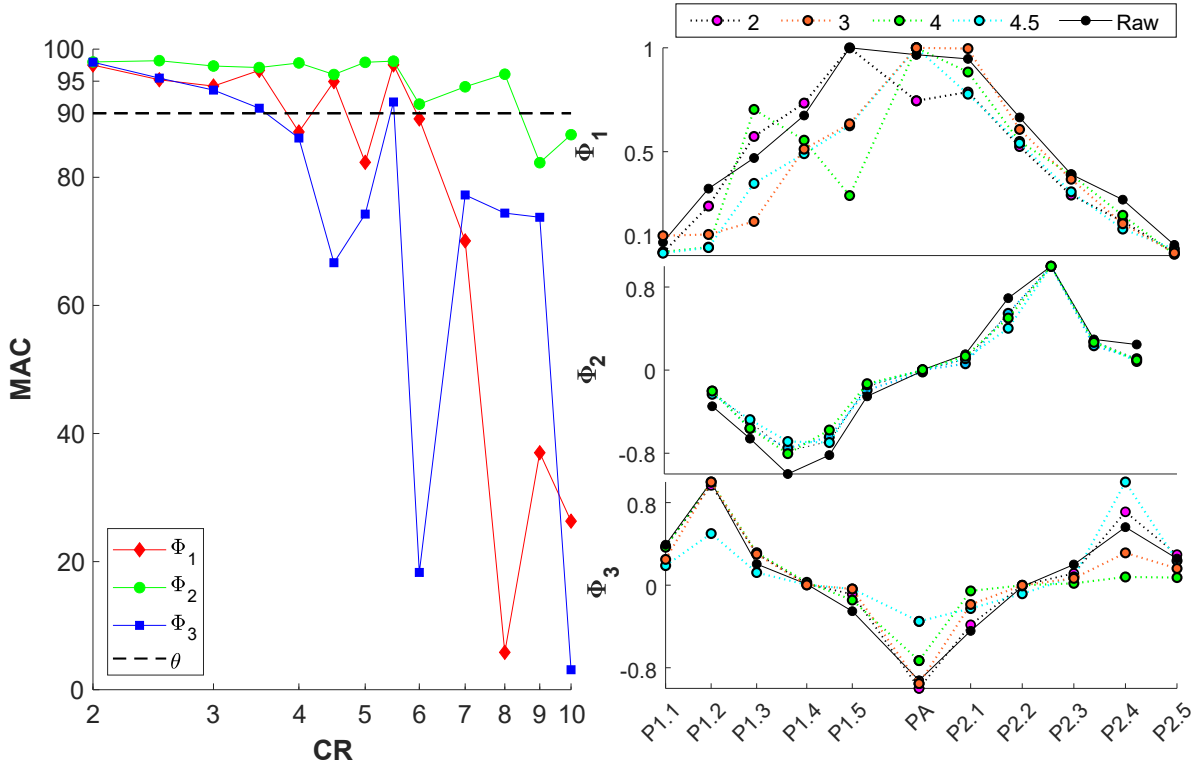


Figure 4.3: Left: trend in MAC values between CS-reconstructed and compression-free full-scale modal shapes as a function of the compression ratio, superimposed to the chosen accuracy level indicated by the black-dotted line at 90%. Red-rumbled, green-rounded and blue-squared line styles refer to the first, second and third modal shape, respectively. Right: reconstructed full-scale modal shapes for a representative selection of CR values.

It is worth noting that an abrupt reduction in modal fitting occurs for compression factors exceeding $CR = 4$. It is also evident that the performance is heavily dependent on the selected mode shape. In fact, if the MAC trend affecting the second modal shape (green-rounded line) is just slowly decreasing with increasing CRs, the behaviour associated with the first modal shape (red-rumbled curve) shows a more pronounced decreasing behaviour. A more peculiar pattern characterises the MAC associated to the third modal shape (blue-squared line). This phenomenon can be attributed to the fact that the energy of the third mode is very weak w.r.t. the other two. Indeed, in this case, the random effects associated to the sampling phase and to the superimposed noise generate the oscillations in the estimated MAC values.

On the contrary, MAC percentages for low CRs (i.e. $CR \in [2; 4]$) are always above 90% for all the inspected modal shapes, apart from the limit case $CR = 4$ where the modal fitting of the first and third mode slightly falls nearby 87%. An additional proof of the

obtained outcomes is provided by the good level of superposition in the corresponding modal shape curves depicted in left-hand side of Fig. 4.3.

Decompression

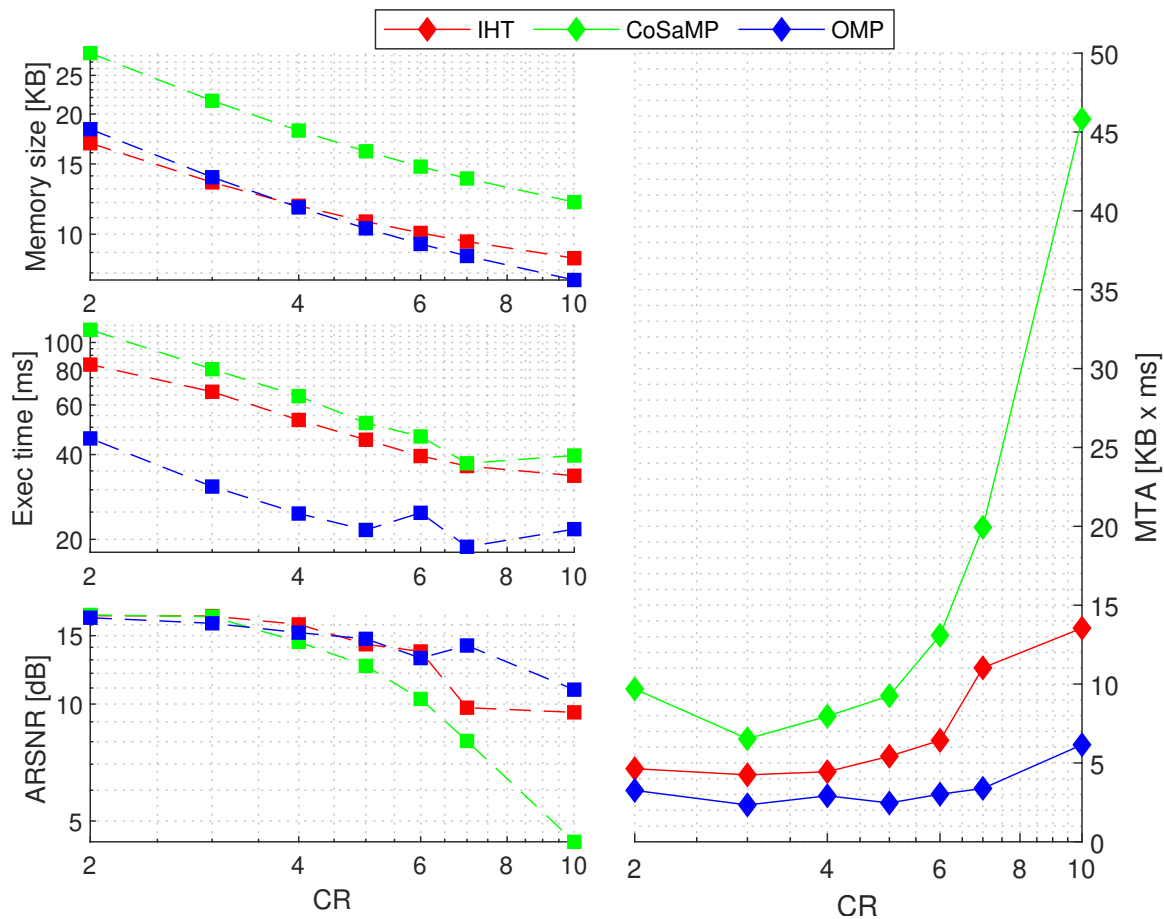


Figure 4.4: Cost analysis for the considered recovery algorithm. In the left-hand side, memory occupancy, execution time and ARSNR are displayed from top to the bottom. The MTA product between the three curves per CR is conversely displayed in the right panel.

The obtained results are depicted in Figure 4.4, where the panels in the left-hand side refer, from top to bottom, to the memory occupancy, the mean execution time and the ARSNR computed by averaging among the six accelerometers respectively. For the sake of clarity, the memory occupancy here reported only accounts for the variables involved in the data recovery algorithms themselves. Thus, assuming that the CS operators are pre-loaded during the network start-up configuration, it has been estimated that, in the worst cases associated to limited compression scenarios (e.g. $CR = 3$), the IHT, CoSaMP and OMP solutions may require a buffer size up to 1 MB due to the huge dimensions of the sensing matrix and the sparsity basis. Accordingly, an example of reconstructed signal

by resorting to the IHT algorithm is displayed in Fig. 4.5, which has been processed with a fixed CR value equal to 4. As it can be observed, the global shape of the waveform is preserved, even if the magnitude of the retrieved high-energy components is lowered.

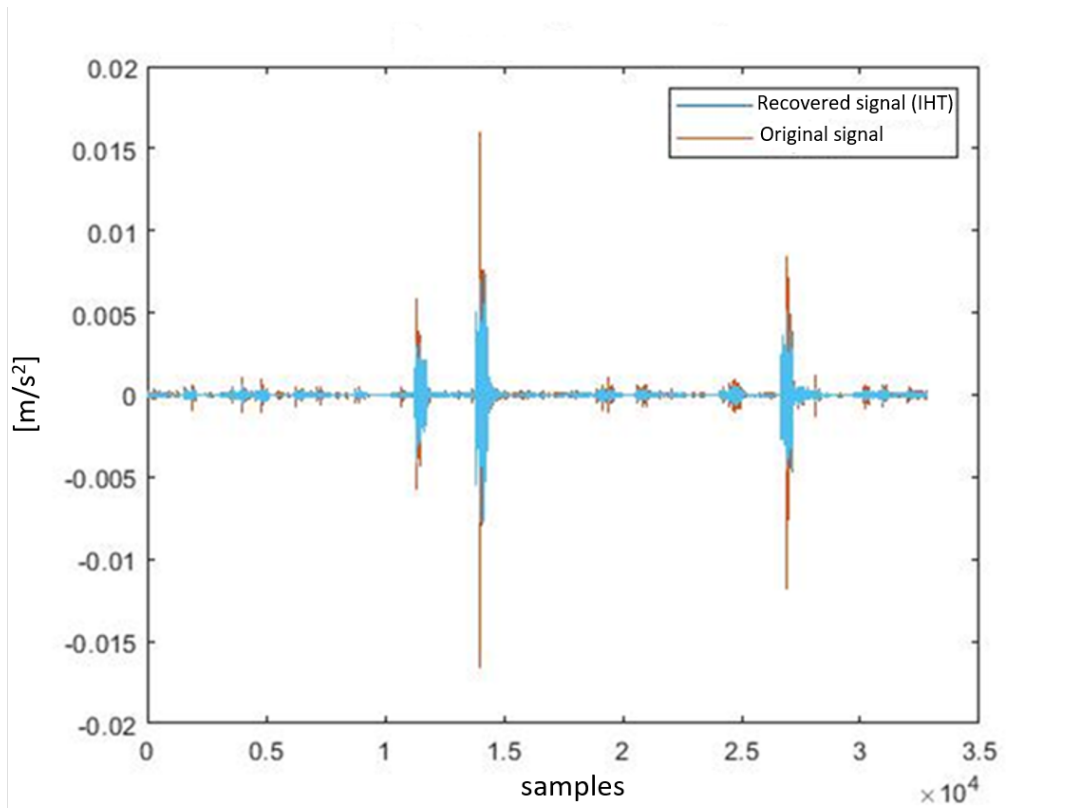


Figure 4.5: Example of IHT-reconstructed signal over 29 different signal frames.

The MTA product is displayed in the right chart to perform an overall cost analysis. As it can be observed, the OMP implementation largely outperforms the other alternatives at all the levels of analysis; its MTA is at least half of the total burden associated to the IHT and CoSaMP implementations for all the considered CRs. It is also worthy to mention that, despite the characteristics of IHT appear to be competitive in terms of memory size, its associated reconstruction accuracy is lower and it requires a larger execution time. Furthermore, the higher memory occupancy characterizing the CoSaMP algorithm is absolutely coherent with respect to the entailed algebraic procedures, given the double dimension of the buffer this technique works on.

4.2 IoT Toolchain Architecture

The Internet of Things (IoT) is now a dominant technology for building automation and industrial solutions and it the base for a variety of applications [152]. One of such is Condition Monitoring (CM), which is crucial for several scenarios in the Industry 4.0. CM is responsible for monitoring a defined physical appliance – or a set of those – via a number of sensors that are deployed in the field. The goal is the monitoring of certain condition parameters, such as vibration in machinery, in order to identify abnormal values and act in advance in case a possible fault is detected or predicted to occur in the future (as in predictive maintenance) [153].

As a proof-of-concept implementation, a use-case related to Structural Health Monitoring (SHM) is discussed, which is also a demonstrator for the Arrowhead Tools project³.

SHM, a particular instance of CM, is a relatively young discipline aimed at assessing the integrity condition of existing structures and critical assets by means of on-condition inspection procedures, meaning that the target structure can be controlled in real-time and over-time [154]. SHM shows two main benefits over standard, scheduled maintenance policies: first of all, it prevents the normal serviceability to be interrupted, since the target structure can be inspected while in its operative conditions and, secondly, it assists inspectors in the decision-making process via automated assessment procedures. However, despite the significant advancements achieved by the information and structural engineering community, the fulfillment of these functionalities compatible with the need of a safer, green and more digital industry still poses major concerns which demand novel maintenance strategies and architectures, such as in our proposal [155]. The current baseline is an SHM sensor network, hosting a number of inertial sensors that monitor the vibrations over a model building. We firstly provided sensors with a degree of interoperability by leveraging the W3C Web of Things (WoT) standard [156]. The W3C WoT is a recent standardization effort that abstract simple sensors and actuators into Web resources that bear a detailed description of their capabilities, their interaction affordances and their semantics. In our case, each of the SHM sensors is equipped with a WoT counterpart that governs all the incoming and outgoing communication. The baseline is enriched by the development of a number of engineering tools, all of them described in detail, that comply with our proposed toolchain architecture, making the use case an instance of our proposal. We then validate the advantages of our approach through selected experiments and we report the observed system behavior utilizing the MODRON [157] platform.

³<https://youtu.be/f8R5vz6kKN4>

4.2.1 The Arrowhead Tools Project

The ECSEL Arrowhead Tools project is one of the biggest EU projects at its time (2019-2022), it features about 90 partners from 17 EU countries and has triggered an investment of more than 100 millions of Euros, shared between the industrial partners, the countries and the EU commission.

The project aims to provide automation and digitalization technologies and solutions to European industry in order to address the integration gaps of Information and Operation technologies. This is achieved by the development of new open-source tools that operate at design time and run time in the engineering process of IoT industrial artifacts.

Within the Arrowhead Tools project, a detailed *engineering process model* has been proposed lately in [158, 159] and to which we will refer to as Arrowhead Tools Engineering Process (AHT-EP). The current version of the AHT-EP features concepts that are compatible with earlier similar models, in order to maintain a backward compliance, and at the same time retain the flexibility to meet current industrial requirements. The AHT-EP is built on top of the well-known *Extended Automation Engineering Model* defined in the ISO/IEC 81346 standard [160]. However, it allows a decoupled flow of information through the engineering process phases (EPPs) which no longer need to be traversed in a fixed order, if needed. The eight EPPs are depicted in Figure 4.6 and are connected via interfaces. Each EPP has an *incoming* (EP-I) and an *outgoing* (EP-O) interface. The term engineering process unit (EPU) means any of the three concepts. Now, the main activities within the Arrowhead Tools project demand the achievement of the project objectives via the development of software *tools*. Tools in the project have been precisely defined as software products (or hardware with adequate software on board) that improve an already established industrial baseline by supporting one or more EPPs [161]. The complete definition features additional properties, such as atomicity and interoperability, which enable the combination of a set of tools, applied in sequence, that can supervise the whole engineering process of a certain artifact. This makes tools suitable for compositional architectures, called *toolchains*, which are simply defined as the sequential composition of engineering tools within a fully fledged engineering process. Finally, tools and toolchains are designed to fulfill a set of project objectives that provide defined KPIs for the evaluation of the impact of the tool onto the baseline:

1. The seamless integration of legacy components into the architecture.
2. The reduction of engineering costs by 20% - 50%.
3. The interoperability with established IoT frameworks.

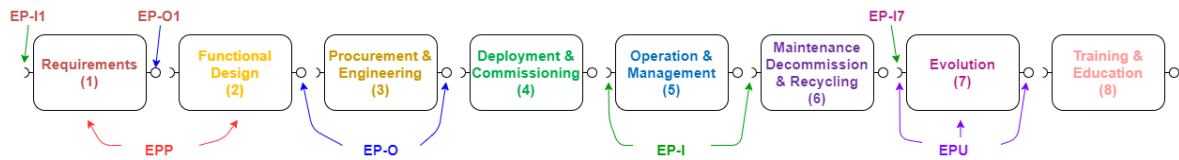


Figure 4.6: A graphical overview of the Arrowhead Tools Engineering Process. [©2023 IEEE]

4.2.2 The Eclipse Arrowhead Framework

The last decade has been dominated by a fast-paced industrial revolution, particularly affecting IoT-based ecosystems. In particular, the Industry 4.0 no longer relies on legacy and monolithic SCADA/DCS systems, instead they are supported by flexible Service-Oriented Architectures (SOA), where modular systems consume or provide services, ensuring loose coupling between modules and their reusability across multiple domains. The Eclipse Arrowhead Framework is a software platform released as an open source product of the Arrowhead Project⁴ that structures closed environments as Local Clouds: controlled ecosystems that implement the base concepts of SOA – loose coupling, late binding, and discovery – and hosts a single instance of a central coordination entity, called the Core Services [162]. Then, each Local Cloud acts as a System-of-Systems in which each system is either an *application system* (if an integral part of the baseline) or a *tool* (if it meets our previous definition). Regardless, they behave as service providers (servers exposed through endpoints) and/or service consumers (clients that query other services). Service consumption is supervised and managed by the Core Services, which must be deployed in the Local Cloud in a minimum set. The latter defines the “mandatory” Core Services in order to be Arrowhead-compliant; which are the Service Registry, the Authorization, and the Orchestration. The Service Registry retains a service record – a set of metadata – for each of the services in the Local Cloud acting as a registrar which enables discovery and loose coupling. Service providers can register themselves or a modeling facility may be used in the design phase of the Local Cloud, such as SysML [163]. The Authorization is a storage of a set of authorization rules that specify whether a consumer is authorized to use a certain service. In addition, it provides a token-based authentication mechanism. Finally, the Orchestration is the enabler of late binding, as it allows an additional actor, the cloud manager, to associate directly consumers to providers at run-time. This way, consumers cannot autonomously decide which service provider to query, instead, they query the Orchestration service to obtain the provider that was assigned to them.

⁴<http://www.arrowheadproject.eu/>

4.2.3 Toolchain architecture

In this Section we present the overall architecture of a toolchain-enabled condition monitoring scenario. We consider the baseline of the environment as a physical structure to monitor and a set of monitoring sensors deployed on it. Furthermore, we can imagine that the structure may be in a poorly connected environment, in which providing cable connection to all the sensor is hard, therefore edge devices communicate with each other via wireless connections and are powered by batteries.

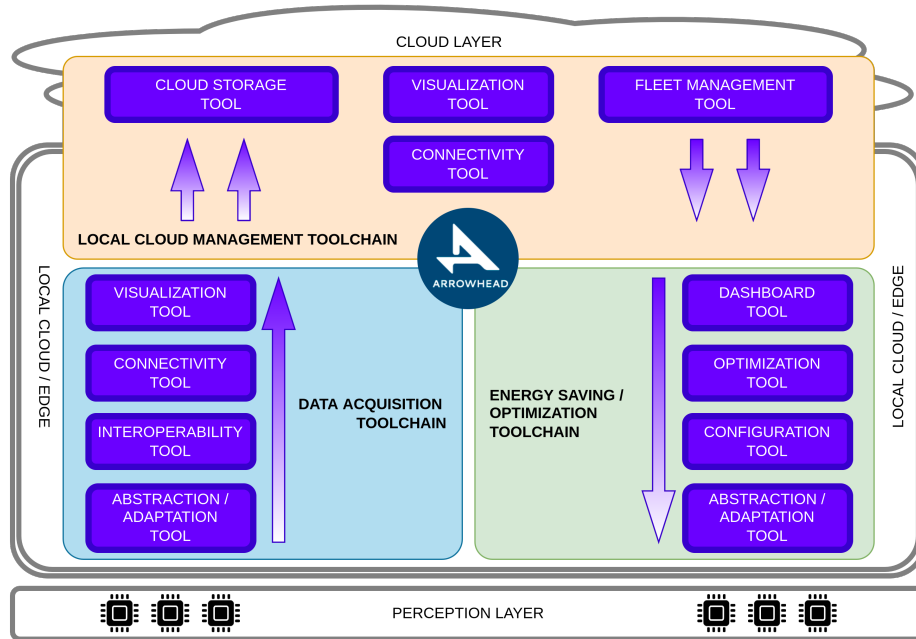


Figure 4.7: Generic toolchain architecture for condition monitoring.

In Section 4.2.1 we set three project objective for a condition monitoring scenario, in order to satisfy a number of KPIs that are necessary for the current standards. In order to fulfill said objectives, we propose a general condition monitoring toolchain architecture, presented in Figure 4.7, composed of a number of engineering tools organized in three distinct toolchains. The architecture is vertically divided into perception layer, where sensors are deployed, cloud layer, where remote services are running, and the Arrowhead Local Cloud, which conceptually includes every application system and tool that is deployed locally with the structure. Interactions among tools and application systems are mediated by a local instance of the Eclipse Arrowhead framework, which also hold a connection with the outer world (i.e. the cloud). Following, the description of our proposed toolchains:

The **Data Acquisition Toolchain** contributes to the first project objective, as it enhances the interoperability of the whole ecosystem by integrating a number of legacy systems that serve different purposes. In detail, the toolchain operates first through an

Abstraction/Adaptation tool, which produces a digital shadow of each physical entity (i.e. the sensors) via one or more IoT standards. It is the case of Arrowhead Services or Web of Things servients (more on this later). The Interoperability tool then is responsible for unifying the data representation and the IoT standard used within the local cloud, just like a translator. The Connectivity tool is responsible for enabling the communication of the local cloud to the outer world, for instance for pushing sensor data to the cloud. Finally, the Visualization tool, which can be inside the local cloud or deployed as a remote service, is in charge of filtering the raw data and displaying it to a final user.

The **Optimization Toolchain** contributes to the second project objective, as its goal is to adjust the local cloud environment in order to minimize the resource consumption of physical devices while meeting the application performance requirements (i.e. maximizing the data throughput). Ideally the process should be automatic and running in parallel with the previous toolchain during the whole lifecycle of the deployment. It uses a Configuration tool, which should be able to change parameters of devices from remote, without the need for human intervention. This is possible through the already mentioned Abstraction/Adaptation tool. Then, an Optimization tool must cyclically perform a computation that outputs the best working conditions for the devices according to their resources as well as the environment conditions (which can change over time). These are provided as an input to the Configuration Tool. Finally, a Dashboard tool should provide a final user a view and a control over the current working conditions.

The **Local Cloud Management Toolchain** contributes to the third project objective by integrating the scenario at cloud level with IoT frameworks. As the Connectivity tool provides the local cloud with bidirectional communication with the cloud services, we can envision both a Cloud Storage tool for data generated by the edge sensors, and a Fleet Management tool, which comes into play in case multiple local clouds are instantiated (i.e. multiple structures). The latter in fact is designed to perform automated maintenance tasks over edge services, such as sanity checks.

4.2.4 The Structural Health Monitoring Pilot

As an instance of the above described toolchain architecture, we present here its concrete implementation into the SHM pilot use case within the Arrowhead Tools project, which is reported in Figure 4.8.

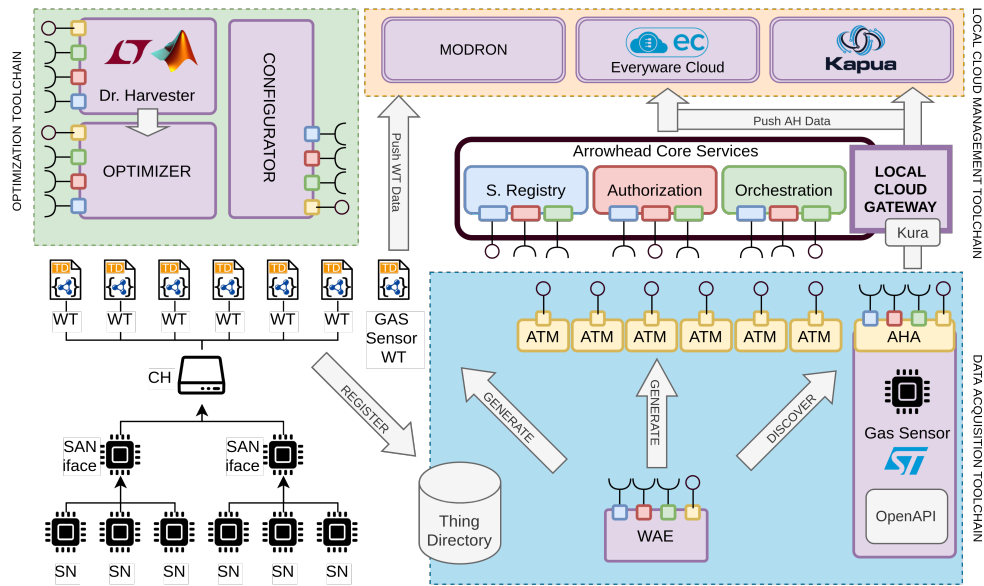


Figure 4.8: Toolchain architecture of the whole System-of-Systems. Main abbreviations are: WT (Web Thing), SN (Sensor node), CH (Cluster Head), WAE (WoT Arrowhead Adapter), ATM (Arrowhead Thing Mirror), OAS (OpenAPI Specification), AHA (Arrowhead Adapter), SR (Service Registry), A (Authorisation), O (Orchestration).

The baseline of the use case features a bridge or a building to monitor (*e.g.* a bridge or a building) and a set of inertial sensors for SHM permanently attached to it. Each sensor cluster is managed by a cluster head that acts as a sink for the data and interacts with any external actor. Thanks to the work carried out within the MAC4PRO project, sensors are abstracted into Web Things (WTs) in order to be accessible via the Web, following the W3C WoT standard [156], which works as an adaptation tool. We then developed a number of engineering tools, organized into our three distinct toolchains: The Data Acquisition Toolchain operates through the Gas Sensor tool, that adds important measurements into the environment, the WAE, that converts WoT elements into Arrowhead services and vice versa, and MODRON, a visualization and management dashboard. The Optimization Toolchain operates through equipping each sensing device with an energy harvester and by developing a number of tools that are able to dynamically and autonomously change sensor properties (*e.g.* the sampling frequency, the duty cycle, etc.) in order to minimize – or, potentially, zero – the battery depletion. The Local Cloud Management Toolchain integrates the scenario with the frameworks Eclipse Kura and Eclipse Kapua. This enables the remote management of multiple local clouds at the same time without having to interact with each of them separately. All the interactions taking place among tools and application systems are mediated and overseen by an instance of the Arrowhead Core Services deployed within the local cloud. We assume that every monitored structure corresponds to a single local cloud, while multiple of them are managed

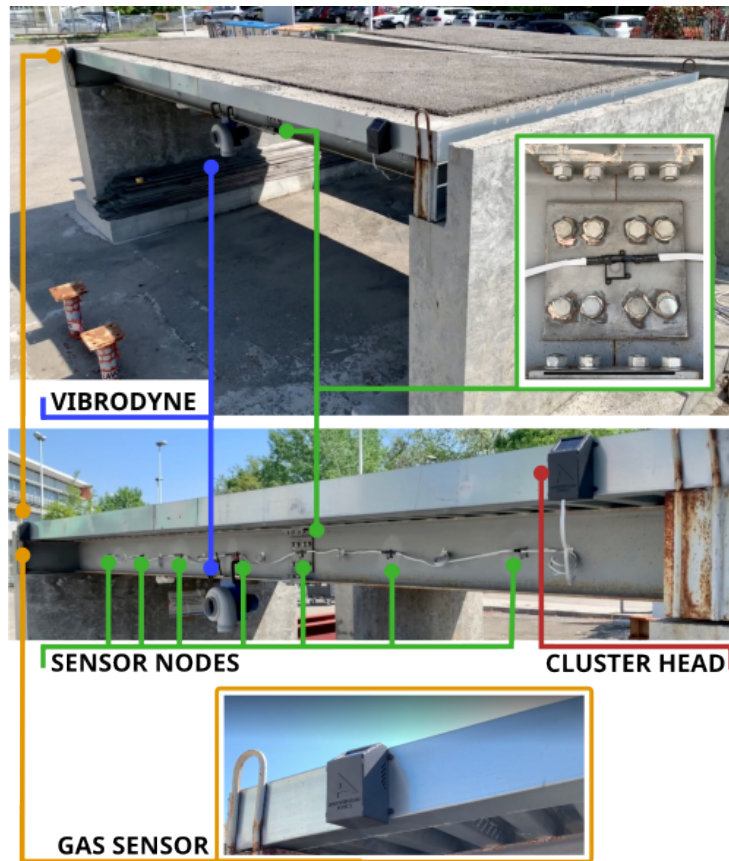


Figure 4.9: Bridge model under test. [©2023 IEEE]

through Eclipse Kapua, which is able to reach different instance of the Core Systems at the same time.

4.2.5 The Deployment Use Case

The effectiveness of the SHM application is validated on an existing use case, which consists of an experimental model of a bridge (Fig. 4.9) located at the Laboratory of Structural and Geotechnical Engineering of the University of Bologna. In detail, the structure represents a 1:4 scale reproduction of a real composite steel-concrete bridge crossing the A14 highway in Italy, near the city of Bologna. The scale replica preserves the materials and their properties, changes concern only the dimensions. More information about the model bridge manufacturing process and material properties can be found in [164].

The deployed Structural Health Monitoring sensor network and its main components are displayed in lower callout of Fig. 4.9, in which one CH (red point) and seven SNs (green points) are noticeable, placed at strategic positions for vibration analysis, i.e., in correspondence of the anti-nodal points of the first modal components. A snapshot of one SN installed at the bridge deck joint has also been enclosed in the upper part of Fig. 4.9.

Besides, a vibrodyne (Fig.4.9 blue point) has been applied to the bridge in order to apply a variable-intensity harmonic excitation up to its power supply settings. In addition to the SHM network outlined above, the deployment includes a Gas Sensor (Fig.4.9 orange points), which is in charge of gas monitoring.

4.2.6 Integration with Legacy Systems

The Data Acquisition Toolchain is composed by several tools that altogether concur in achieving the first project objective: the seamless interoperability and the integration of legacy systems. The demo environment illustrated in Section 4.2.5 hosts locally a physical instance of the Local Cloud Gateway. The latter is responsible for running the Kura bundle of each of the SHM sensors as well as of the Gas sensor. The bundles are available to a cloud instance of Kapua within the Local Cloud Management Toolchain. Furthermore, the Local Cloud Gateway hosts an instance of the Arrowhead Core Service, the WAE and works as a WiFi bridge for the CH of the sensor network, giving it the exposure over the internet for all the WTs that it runs. The WTs are then consumed by a cloud instance of MODRON, which is able to show the sensor values of each of the WT without the need for adapting to a underlying technology, as the WAE converts all services into WTs.

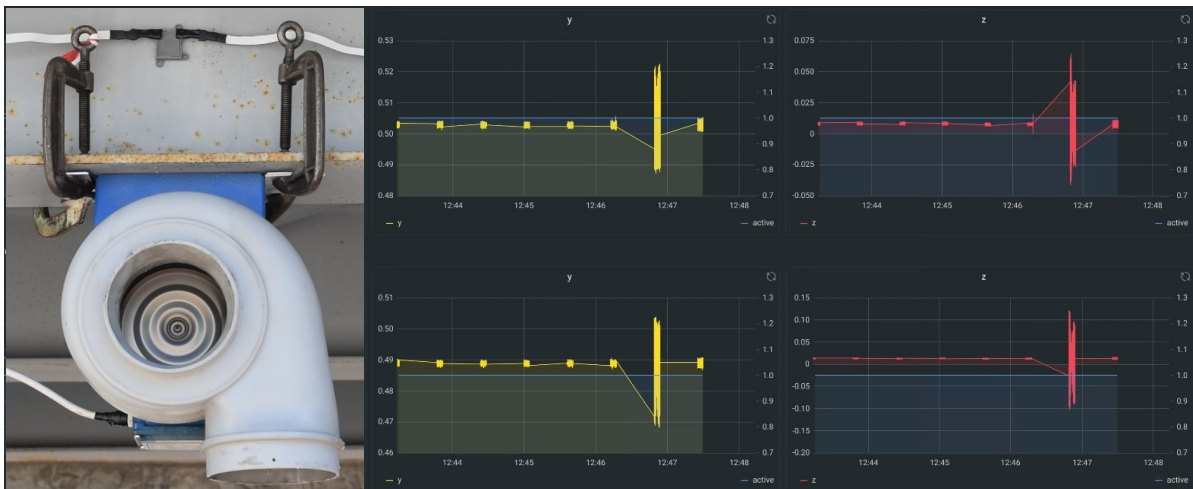


Figure 4.10: Sensor readings of the SHM sensors on MODRON, it shows an accelerometer bursts that change after the vibrodyne is turned on. [©2023 IEEE]

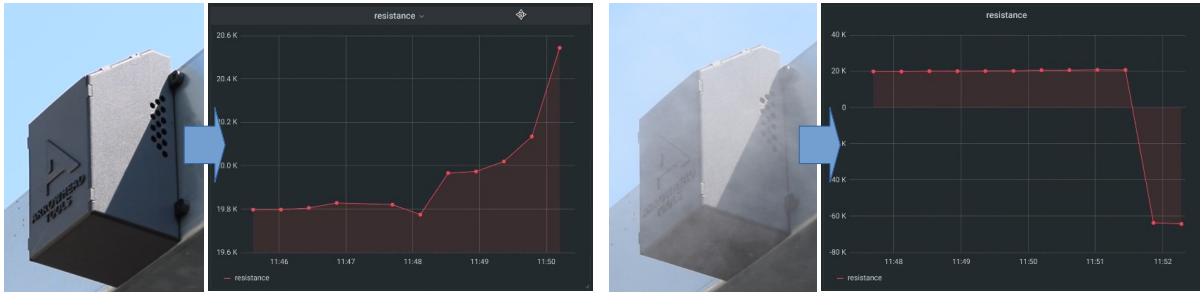


Figure 4.11: Sensor readings of the gas sensor on MODRON, it shows how the data from the gas sensor changes before and after the gas sensor is sprayed with gas. [©2023 IEEE]

The validation of the toolchain has taken place by means of the sensor values shown through the Grafana dashboard of MODRON. Figure 4.10 and 4.11 shows the sensor values reported into said dashboard. In particular, the upper figure shows how we solicit sensor readings by turning on the vibrodyne and, thus, injecting vibrations into the structure. These are captured by the accelerometers and reported in one of the last bursts on their Y and Z axes, also visible in the picture (the X axis is not very significant as the bridge does not vibrate much longitudinally). The exact same system is used to detect variations of the concentration of gas, as captured by the gas sensor in the lower part of the figure. In particular, we show how injecting gas in the environment (in this case through a spray can) causes the sensor resistance to dramatically drop – note that the readings in absence of gas appear to variate, however this is negligible as the scales on the two Y-axes are very different. The validation shows a small real world fully operational system, however, the main advantage here is the interoperability: in fact adding more physical sensors or other systems does not cause the complexity to increase, as the “hub” systems such as MODRON do not need any additional interface to cope with on-boarding processes, rather they take place seamlessly.

4.2.7 Results

In this research, we proposed an architectural approach for CM scenarios based on software toolchains that are responsible for a defined set of tasks. Different toolchains support the engineering process of the SoS and enable the separation of concerns for the different actors that typically interact with complex and scalable CM scenarios. Following the guidelines of the Arrowhead Tools project, we first established a number of goals that our architecture aims to accomplish and we then developed several engineering tools that compose the proposed toolchains at all layers of the architecture. We then experimented with the three developed toolchains in a real SHM scenario that involves inertial and gas sensors installed over a bridge. The tests proved the efficacy of the implemented

toolchains, in particular the improved automation of the whole engineering process for wider fruition by different stakeholders at different levels of abstraction.

4.3 Output-only SysId models for vibration analysis

SysId implemented via regression techniques aims at identifying the filter taps, also known as *model parameters*, by minimizing the error between the predicted and actually measured system response according to certain heuristics. As discussed beforehand, a characterizing feature of real-field monitoring is that the current structural status has to be inferred directly from the collected vibration response, a procedure which is usually referred to as *output-only* SysId. In these cases, the only accessible information is the one given by the observed vibration signals, while the input stimulus is assumed equal to a zero-mean white noise Gaussian term $e(t) \sim \mathcal{N}(0, \sigma_e^2)$, whose variance σ_e^2 needs to be explicitly computed. Among the most effective regression models available for this task, the Autoregressive (AR) and Autoregressive with Moving Average (ARMA) models can be listed.

In analytical terms, given $y[k]$ the system response gathered at a time stamp kT_s (with T_s indicating the sampling period), a univariate discrete-time ARMA model at a generic sample $k \in \{0, \dots, N-1\}$ reads:

$$y[k] + \sum_{i=1}^q \theta_i y[k - iT_s] = e[k] + \sum_{s=0}^p \gamma_s e[k - sT_s] \quad (4.5)$$

in which q and p specifically determine the number of parameters preserving memory of the past p input and q output instances, while θ_i and γ_s are the feedback and feed-forward taps of the corresponding filter. p and q are also known as the orders of the filter numerator and denominator polynomials, while their summation $N_p = p + q + 1$ equals the total amount of model coefficients to be determined.

Alternatively, AR models can be derived from Eq. (4.5) by zeroing the contribution of the moving average term in the right-hand side of the equation, yielding to:

$$y[k] + \sum_{i=1}^q \theta_i y[k - iT_s] = e[k] \quad (4.6)$$

In this case, $N_p = q + 1$ holds.

Therefore, all the structural features of interest can be obtained from the Fourier transform of Eq. (4.5) or (4.6). To this end, of particular interest is the estimation of the system power spectral density, computed as the square power of the associated filter frequency response function as:

$$S_y(f) = \left| \frac{1 + \sum_{s=0}^p \gamma_s e^{-j2\pi f s T_s}}{1 - \sum_{i=0}^q \theta_i e^{-j2\pi f i T_s}} \right|^2 \quad (4.7)$$

or

$$S_y(f) = \frac{\sigma_e^2}{|1 - \sum_{i=0}^q \theta_i e^{-j2\pi f i T_s}|^2} \quad (4.8)$$

depending on whether an ARMA or AR model has been adopted, respectively.

4.3.1 New Hardware for SHM

To enable the edge processing described in the previous Section, an optimized sensor node (SN) based on a wireless communication and a low-power, high-performance MCU has been designed. The wireless connection is crucial to simplify the deployment in large-scale structures, but poses major challenges in terms of energy-saving. To overcome this energy issue, a peculiar triggering solution built on the exploitation of two tri-axial MEMS accelerometers has been adopted: the first one is the ST Microelectronics AIS2IH [165], which is a very inexpensive and ultra-low-power device which wakes-up the second, high-performance, Analog Devices ADXL355 accelerometer [166], characterized by ultra-low noise density but higher energy consumption.

Thanks to this unique combination, the designed SN can acquire tri-axial accelerations, accessed via the digital output (SPI or I²C interface) of the MEMS accelerometers, in a full-scale acceleration range up to ± 8 g. In more detail, the AIS2IH is characterized by a sub-1 μ A current consumption, 12-bit resolution in low-power mode and an Output Data Rate (ODR) from 1.6 Hz to 1600 Hz. Conversely, the ADXL355 shows a current drain around 200 μ A, but it benefits from an ultra-low noise density of 22.5 μ g/ $\sqrt{\text{Hz}}$, 20-bit Analog-to-Digital Conversion (ADC) resolution and a maximum ODR of 4000 Hz.

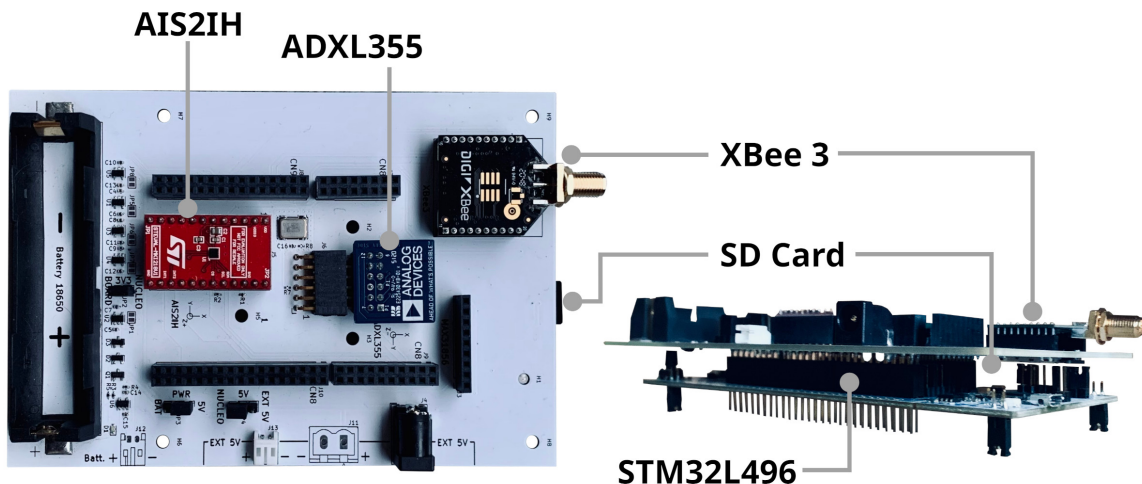


Figure 4.12: Top and lateral view of the developed Sensor Node

The accelerometers, together with all the peripherals, the MCU and the other components necessary to acquire, process and transmit data, are assembled in the evaluation

board shown in Fig. 4.12. The core of each SN is the 32-bit Ultra-Low-Power ST Microelectronics MCU STM32L496, a microcontroller based on an ARM Cortex-M4 operating at a frequency up to 80 MHz, with a Floating Point Unit, a Digital Signal Processing instruction set, 320 KiB of SRAM and 1 MB of Flash memory. This device is particularly appealing for all those applications in which low-power consumption is a primary issue: indeed, a consistent variety of power-saving modes have been implemented for its programming, e.g., 15 nA in shutdown mode, 115 nA in standby mode and 1.1 μ A in stop mode.

To expand the storage capability while maximizing the memory space necessary for data processing, an external SD Card has also been included for vibration signal retrieval. Finally, the communication between each SN and a common aggregating unit, intended either as a dedicated embedded device or a remote PC, is based on the 802.15.4 protocol, allowing the devices to communicate wirelessly via the Digi XBee 3 module, selected to ensure a good balance between transmission ranges and attainable data rates.

Hybrid Energy Harvesting

The wireless sensor node presented has an additional feature than the previous SSN. It hosts a MCP73832 by Microchip [167], a single cell Lithium-Ion, or Lithium-Polymer, charge management controllers up to 500 mA. This device can be used with a solar panel, or solar cell, as long as the generated voltage is between 4.5 V and 5.5 V. Many tests with different solar panels and solar cells have been conducted, finally the choice was on solar cell SM141K09L by IXYS [168] (Fig. 4.13) whose characteristics are shown in Table 4.1.

Table 4.1: Solar cell SM141K09L characteristics [168]

Grandezza fisica	Value
Open circuit voltage V_{oc}	6.22 V
Short circuit current I_{sc}	58.6 mA
Voltage at max. power point V_{MPP}	5.02 V
Current at max. power point I_{MPP}	55.1 mA
Maximum peak power P_{MPP}	277 mW
Fill factor FF	> 70%
Efficiency η	25%
Size	63 \times 23 mm

Using two of those cells by experimental test (Fig. 4.13) is possible to generate up

to 250 mW (approx. 55 mA at 4.5 V), while the SN in Section 4.3.1 has a maximum power consumption of 114 mW in data transmission mode and around 99 μ W in power save mode.

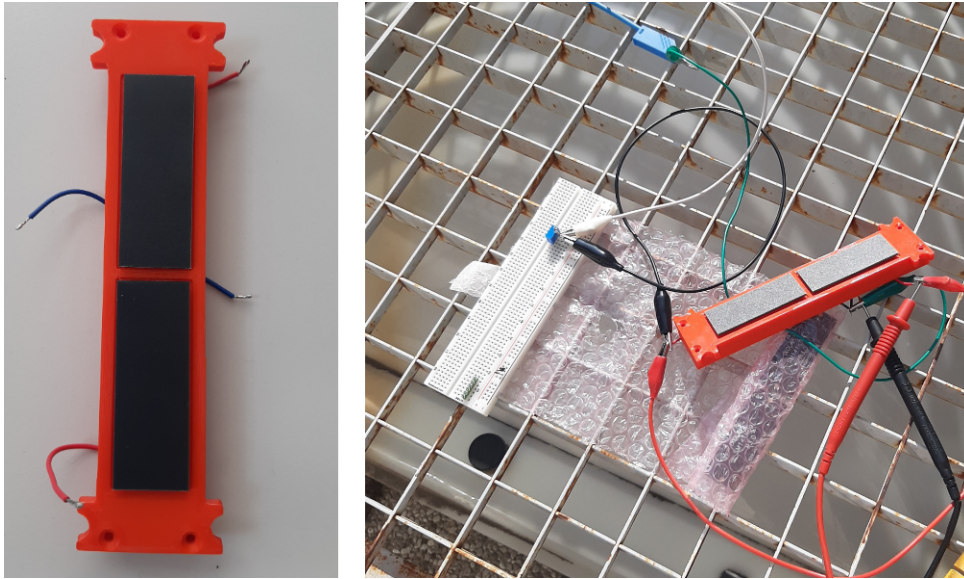


Figure 4.13: SM141K09L solar cells during test.

Moreover, a vibrational Energy Harvest based on electromagnetic technology has been studied. In particular, it was replicated the one in this paper [169] with some changes previously studied on COMSOL Multiphysics simulator. It was developed not only the electromagnetic part (grey cylindrical shape in Fig. 4.14), but also an ad-hoc circuit (PCB in Fig. 4.14) for power harvesting with a LT1302 [170] as main component, a high efficiency micropower step-up DC/DC converter.

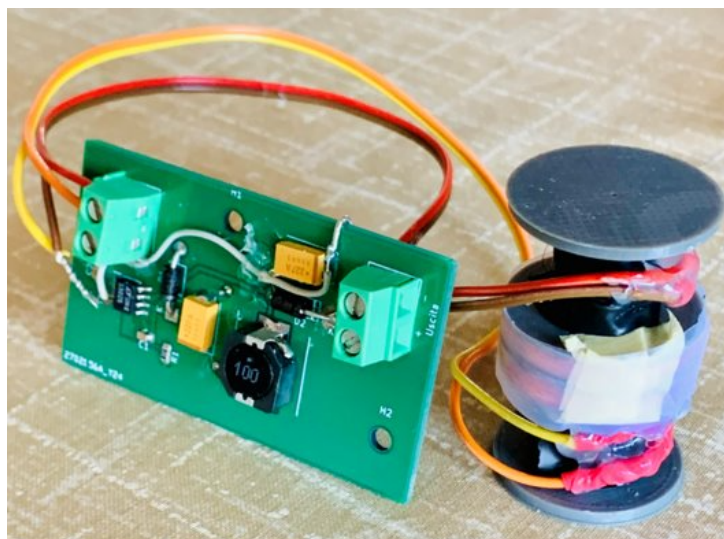


Figure 4.14: Electromagnetic Energy Harvester.

Finally, a solution based on a piezoelectric cantilever was evaluated in order to test an

other vibrational energy conversion method. The cantilever selected was a Mide Technologies 118-J1SS-1808YB [171], 71 x 25.4 x 0.71 mm size, theoretical peak power of 0.7 mW and 130 Hz resonant frequency.

Briefly, analyzing the results obtained from the implementation of the three different Energy Harvesters shown in this Section, the peak powers obtained are as follows:

- Solar Energy Harvester: 250 mW
- Electromagnetic Energy Harvester: 2 mW
- Piezoelectric Energy Harvester: 0.2 mW

About the results of the first last two vibrational Energy Harvesters, it is normal that the extracted powers are significantly less than the more efficient and established solar technology. However, the performance is still below expectations for the electromagnetic solution, in which we could see the possibility to obtain at least about 10 mW. The realization was definitely vitiated by the not completely successful adaptation of the EHs to a different vibration frequency. Thanks to this experience, it has already been started new COMSOL simulation based on Finite Element Method to get new designs.

4.3.2 Experimental validation

Materials and methods

The simply supported steel beam used in CS activity too has been adopted as a representative test-bed to assess the validity of the edge implementation of output-only SysId models for vibration diagnostics. To this end, one SN has been installed on the top surface of the beam, free to vibrate under hammer excitation (see Figure 4.15). A purposely developed Finite Element model has been adopted to predict the first four dominant modes of vibration, which were estimated equal to $f_1 = 6.74$ Hz, $f_2 = 26.95$ Hz, $f_3 = 60.63$ Hz, $f_4 = 107.79$ Hz for an effective span length of the beam equal to $L = 1.842$ m. These values were used during the evaluation process to measure the level of consistency between the expected and the actually measured modal components and, by extension, to validate the consistency of the retrieved structural signature via the implemented SysId processing at the edge.

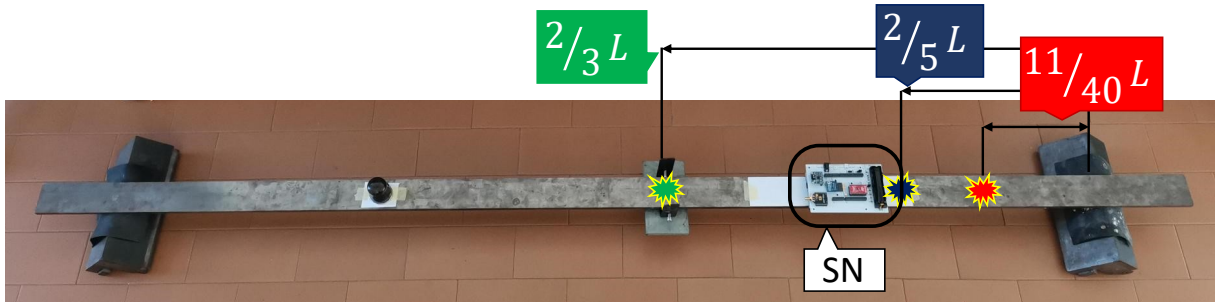


Figure 4.15: Experimental setup: simply supported steel beam with magnified damage positions (blue, red and green marker).

To this purpose, the collected data are processed directly on the SN which outputs the sought model parameters. The corresponding power spectral density is computed via Eq. (4.7) or (4.8) depending on the adopted regression model. Then, the accuracy of these spectra is judged by computing the Itakura–Saito Spectral Distance (ISD):

$$ISD = \frac{1}{N} \left[\frac{S_y^{SN}(f)}{S_y^{Mat}(f)} - \log \left(\frac{S_y^{SN}(f)}{S_y^{Mat}(f)} \right) - 1 \right] \quad (4.9)$$

which measures, in a cumulative manner, the level of superposition between the actually reconstructed spectral profile from the model parameters yielded by the SN ($S_y^{SN}(f)$) and the same spectrum computed offline in Matlab with identical routines ($S_y^{Mat}(f)$), serving as reference values. ISD equal to zero means perfect superposition, while 1 indicates complete misalignment. Finally, a comparison between the SysId-driven power spectrum and the one obtained with the standard Welch's algorithm has also been enclosed to assess the frequency alignment between the two different spectral estimation methods.

The processing framework has been configured to work with an ARMA(16,16) and an AR(16) model, whose respective orders have been estimated experimentally via the Bayesian Information Criterion (BIC) [172] in a preliminary phase.

4.3.3 Results

Nominal configuration

Results for the ISD are collected in Table 4.2 for different 800-long frames of the acquired signals, for the ARMA (first row) and AR (second row) case. As it can be observed, the spectral superposition is remarkably accurate, as confirmed by ISD quantities always below $7 \cdot 10^{-3}$, which prove the algorithmic accuracy of the implemented SysId processing and disclose new potential for spectral-based structural assessment.

Basing on these results, the power spectra of the ARMA (blue) and AR (red) in Figure 4.16 have been reconstructed and superimposed on the ones yielded by the Welch's

Table 4.2: ISD values (multiplied by 10^{-3}) for ARMA(16,16) and AR(16) model with 800-long frame size.

Model	Window frame											
	1	2	3	4	5	6	7	8	9	10	11	12
ARMA	6.34	6.21	6.50	6.38	6.20	6.47	6.71	6.83	6.86	6.57	6.66	7.04
AR	0.31	0.32	0.11	0.22	0.30	0.37	0.03	0.05	0.04	0.07	0.08	0.14

estimator (black curve). As a primary evidence, the peak spectral alignment between the three strategies is clearly evident, the SysId spectra being much sharper and smoother for the entire frequency axis. Note that this result, which is a defining trait of SysId processing, is of the utmost importance in view of modal identification, where the retrieval of the dominant modes of vibration is usually accomplished via peak-picking methods [173]. Indeed, spurious peaks, that are most likely due to insufficient spectral resolution for the considered signal length, are completely filtered out when moving from Welch to AR/ARMA spectra.

The average time taken to execute the ARMA and AR model at a clock frequency of 80 MHz amounts to 5.407 s and 0.585 s, respectively. Hence, assuming the power consumption of 15 mA in normal operating mode for this frequency, a power consumption of 3.66 J, comprising total time processing for an entire signal of 10400 samples (around 74 s), was measured for the ARMA case, which represents the most onerous strategy. Noteworthy, the same energy expenditure dramatically increases up to 7.50 J when the system clock reduces to 16 MHz. This result is largely due to the fact that, in this new configuration, despite being lower the energy expenditure (i.e., 7 mA) the processing time increases to a large extent (up to 325 s), thus undermining the energy savings associated to the lower power mode.

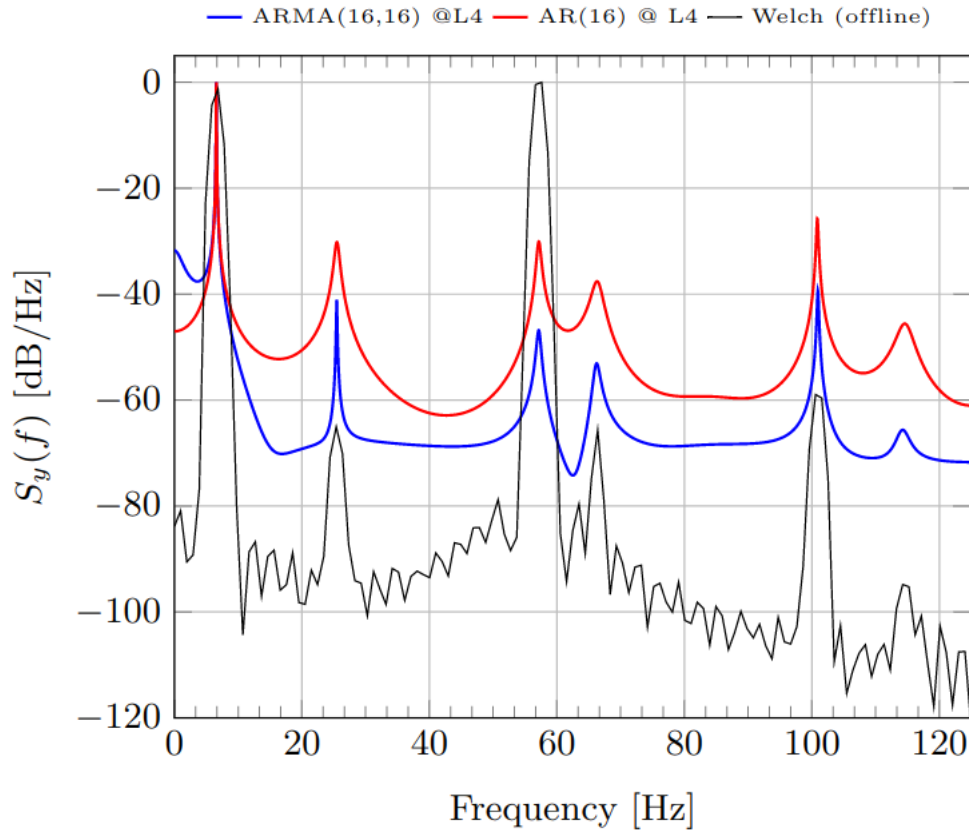


Figure 4.16: Normalized power spectra computed via the embedded ARMA(16,16) (blue) and AR(16) (red) SysId algorithms, compared to the Welch (black) estimation performed offline.

Damaged configuration

In a second phase of the experimental campaign, the nominal behavior of the beam was altered by adding a dead mass to the beam in different positions, as displayed in Figure 4.15. The corresponding power spectra obtained from the model parameters yielded by the SN in these configurations are depicted in Figure 4.17, for the ARMA (top) and AR (bottom) processing. A clear variation in the peak spectral values (highlighted by the gray background boxes) associated with the second and third modal components can be observed. Such variation is proportional to the entity of the hanged dead mass and its position with respect to the nodal and antinodal values of the mode shapes. More specifically, it is worth noticing that, thanks to the smooth profile characterizing the depicted spectral curves, even subtle changes can be tracked with satisfying resolution, which is a very valuable feature for damage detection tasks.

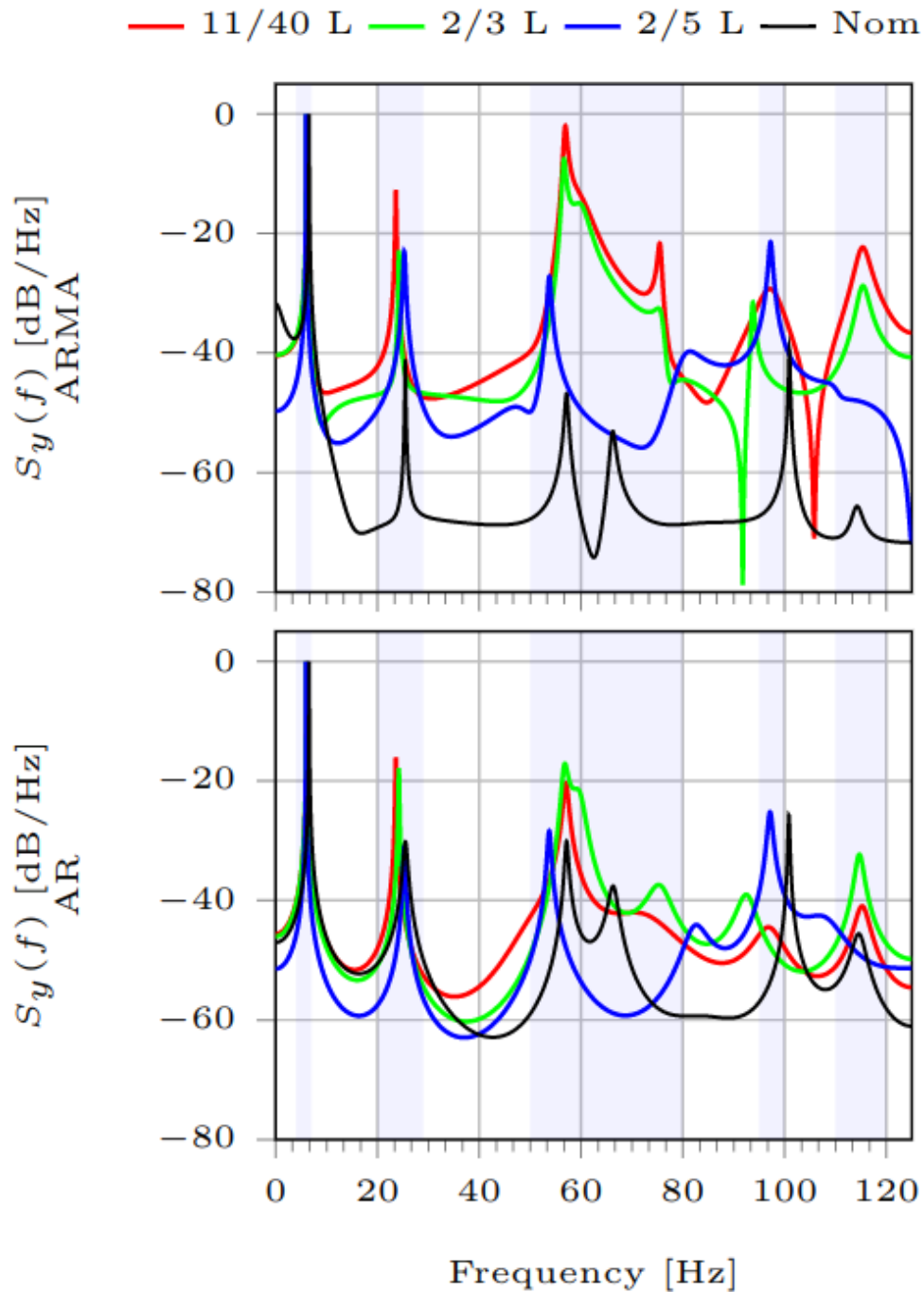


Figure 4.17: Normalized power spectra in damaged configurations computed by the SN from ARMA (top) and AR (bottom) model parameters. Apart from the mass-free configuration (label Nom), a dead mass has been hanged at three different positions to simulate the effect of anomalies. Grey background boxes have been included to underline the variations in the peak spectral values.

4.4 Artificial Intelligence perspective

Nowadays, physical complexity, wide dimensions and big data volume have become pivotal keywords in the Structural Health Monitoring (SHM) field, thus posing important challenges in the design of resilient and effective SHM systems [174]. Indeed, spanning from the civil to the industrial application domain, the urge for sensor network optimization has been faced by several authors [175], aiming at *(i)* reducing the total amount of information which should be transmitted over the network, *(ii)* increasing the responsiveness to subtle changes in the structural behaviour and *(iii)* lowering the latency in the data-to-user transfer process.

In this context, the Tiny Machine Learning (TinyML) paradigm, i.e. the implementation of very thin and low power demanding neural networks running on edge devices at the boundary between the physical and digital world, has very recently pioneered outstanding solutions to jointly cope with all the above mentioned issues. Hence, TinyML could bring a radical shift of perspective, moving from cloud-based data analytics, which is usually performed on remote servers in a time and energy consuming manner, to sensor-near data inference, empowered to smart sensors in charge of processing information in a streaming fashion. Accordingly, the advantage of TinyML is to shift the artificial intelligence itself in strict proximity where structural information is actually sensed, so as to expedite the inference time and, thus, the diagnostic process.

TinyML was successfully applied in several domains, such as the biomedical [176], the environmental [177, 178] and the image processing field [179], to name a few. Nevertheless, to the best of the authors' knowledge, no work can be found in the literature in which TinyML approaches have already been explored in the SHM context. In line with this observation, the present work specifically attempts at filling this gap.

To this end, among the multiple tasks involved in the SHM-chain, TinyML finds its natural application to damage detection and classification. Hereby, the main contribution of this work is to present the practical embodiment of a TinyML architecture on a resource-constrained device for the health assessment of vibrating structures, i.e. structures which can be thoroughly described by means of frequency-related quantities, conventionally extracted by resorting to operational modal analysis (OMA) strategies. These frequency parameters, which are also called as *modal parameters* since they can describe the *modal* (dynamic) properties of the structure, encompass natural frequencies of vibrations (i.e., the frequencies associated with the peak spectral values) and mode shapes (i.e., the specific spatial patterns exhibited by each modal component at different structural positions) [180].

Here, the health assessment process is tackled as a binary classification problem, by tracking over time the evolution of the above described modal parameters. To this end,

the very recent Once Class Classifier Neural Network (OCCNN) [181], which requires natural frequencies of vibration as inputs and provides the corresponding damage status (i.e. healthy/unhealthy) as output, was implemented and revised in a TinyML format.

4.4.1 OCCNN–based vibration diagnostics

In this section, the building blocks of the OCCNN–based vibration diagnostic process are presented, starting with the standard OMA algorithms and concluding with the OCCNN architecture. A graphical description of the complete processing flow is drawn in Fig. 4.18.

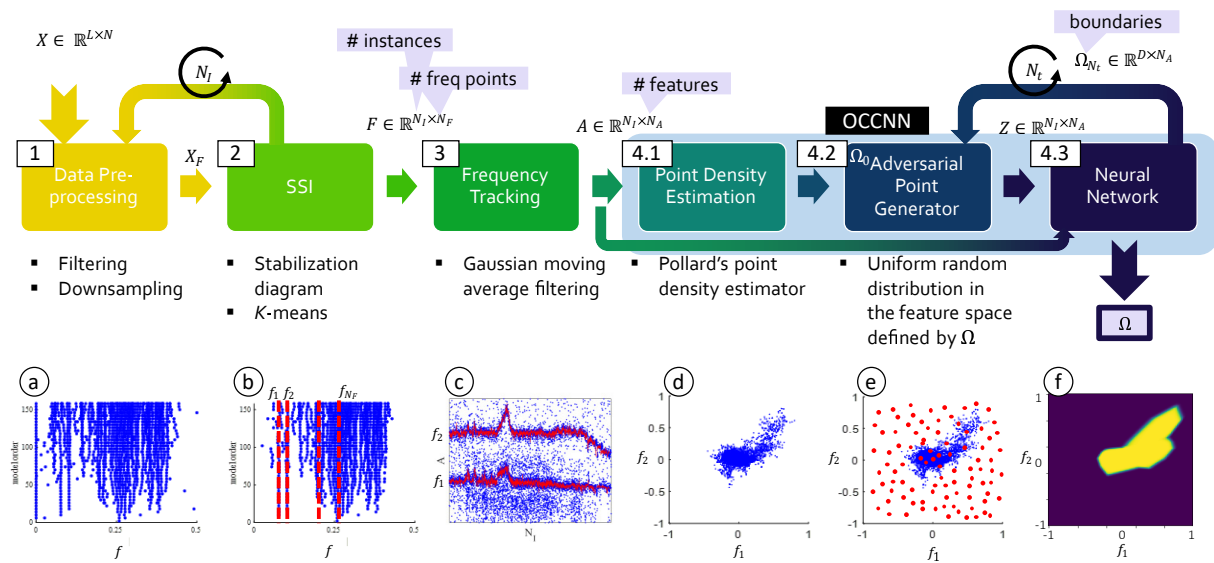


Figure 4.18: Workflow for OCCNN–based anomaly detection combined with OMA.

From modal analysis to feature reduction

Let's suppose that a number of L active sensors is installed on the target structure, each of them acquiring N –long time series, arranged in a matrix X . Since data might be corrupted by outliers as well as the sampling frequency is usually much higher than the frequency band of interest, a *data pre–processing* step is typically encompassed, in which the collected waveforms are manipulated to favour the feature extraction phase. To this end, filtering and downsampling are the two most widely applied operations.

Then, in order the modal parameters to be estimated (step 1), a consistent variety of OMA algorithms proved to be available, facing the problem of feature extraction either in the frequency or time domain. In this work, the Stochastic Subspace Identification (SSI) strategy [182] is applied (step 1) by virtue of its unsupervised nature. In its essence, SSI extracts modal information from the n topmost eigenvalues of the covariance matrix of the acquired signals, n being the so–called model order. By sweeping n in quite a

broad range, the stabilization diagram (Fig. 4.1(a)) can be depicted, which is a common graphical tool used to identify the true modes from artifacts by looking for the bold and longest vertical lines. The latter quantities, which are highlighted in Fig. 4.1(a) with red dotted vertical lines, can be numerically estimated by means of clustering algorithms, such as the k -means method [183] employed here. At the end of this procedure, which has to be repeated N_I times if N_I represents the number of successive time series that have been acquired, the vector F of clustered frequency values is computed and forwarded to the following *frequency tracking* phase (step 2).

At this stage, a feature reduction step is firstly encompassed by selecting the $N_A, \subseteq N_F$ frequency components of interests (referred to as features and indicated with A), corresponding to the most damage-sensitive frequency regions given by the combination of the experimental outcome and the mechanical properties of the structure. Therefore, a Gaussian moving average filter is applied to track the time evolution of these N_A components and obtain smoother frequency trends around each pivotal frequency (Fig. 4.1(b)). It is at this point that the actual artificial intelligence domain comes to play.

OCCNN architecture in a nutshell

OCCNN was firstly proposed in [181] for the purpose of anomaly detection and effectively applied for the structural assessment of the Z24 bridge structure [184]. Fed with data taken from the target (healthy) class, it serves the goal of determining whether the structure is in pristine or damaged conditions. It consists of three main elements: *(i)* a point density estimator (step 3.1), to identify the scattering distribution of the frequency values identified at the end of the modal phase; *(ii)* the adversarial point generator (step 3.2), which artificially engenders points belonging to the defective class Z (red points in Fig. 4.1(c)); *(iii)* a Neural Network (NN) architecture (step 3.3) finally learning the boundaries Ω between the healthy and unhealthy working conditions (e.g., the yellow and blue regions in Fig. 4.1(d)).

The NN represents the actual machine learning core of the entire process and it is designed as a simple feed-forward NN with two hidden layers, each of them comprising 50 neurons with Rectified Linear Unit (ReLU) as activation function, and one output layer. It is from the iteration of the two latter steps that the boundary learning capability of the OCCNN strategy can be tuned: the higher the number of repetitions (N_t), the higher the definition of the learned boundaries.

4.4.2 Experimental validation

Coherently with previous investigations, the performance of the OCCNN architecture are tested on the Z24 bridge use-case, for which a very consistent and large dataset has been publicly released ⁵.

Materials and methods

The Z24 bridge benchmark has been widely exploited for modal analysis studies since it represents one of the very few supervised examples available in the literature which comprises both nominal and man-induced damaged conditions, each of them including the proper label. More specifically, a long-term continuous experimental campaign was designed, in which the bridge, located in Switzerland and connecting the cities of Zürich and Bern, was monitored for almost one year prior its demolition. The monitoring system comprised eight tri-axial force-balance-type FBA-11 accelerometers by Kinematics, each of them acquiring data ($N = 65635$ samples) at a sampling frequency of 100 Hz. Besides, more than fifty environmental sensors were installed on the critical parts of the structure to ensure a good correlation with the actual damage level. Furthermore, during the last month, a short-term progressive damage test phase was followed in which different but controlled kinds of defects were provoked for the sake of damage assessment.

In this manner, it was possible to track the evolution of the structural parameters not only as a function of real structural diseases, but also in response of environmental and operational factors, such as temperature and humidity. Coherently, being capable to track with sufficient precision these environmental-related changes is of the uttermost importance since their effects could be even more significant to the one due to actual deterioration [185].

To summarize, a total amount of $N_I = 5651$ measurement instances were successively collected beyond the instrumentation failures, which are divided into 89% for the nominal status and the remaining 11% for defective ones. Given this distribution and in compliance with the nature of the OCCNN architecture, training and validation were done only by taking the 70% of data (4000 instances) pertaining to the nominal condition. Conversely, the remaining portion of the dataset (populated with both healthy and unhealthy points for a total amount of 1561 instances) was employed in the testing phase.

Concerning the structural identification process, modal analysis studies [186] for the Z24 bridge reveal that the most energetic content of the structure lies below 25 Hz; for this reason, a preliminary stage of dataset preparation was executed including a downsampling procedure combined with data filtering. Then, the SSI algorithm with varying model order

⁵<https://bwk.kuleuven.be/bwm/z24>

(up to $n = 160$) was applied to track the evolution of the first two modal components (i.e., $N_A = 2$) out of $N_F = 15$ clustered frequencies.

Implementation on the edge device

The Arduino Nano 33 BLE Sense board [187] was used as target platform for the validation of the explored TinyML architectures, and it is characterised by the tiniest form factor within the family of AI–empowered Arduino solutions. The microcontroller unit (MCU), which is the low–power nRF52840 component by Nordic Semiconductor, features 256 kB serial RAM and 1 MB FLASH memory with advanced digital signal processing functionalities enabled by a single–precision floating point unit. The device embeds several peripherals, such as an inertial measurement unit, a microphone, a temperature/humidity sensing element and a gesture/proximity sensor, which make it promising in several applications.

In Fig. 4.19, the three steps which need to be followed to transform a standard NN model run on remote stations into MCU–compliant models, are depicted. Once the classification architecture has been trained and validated offline in the standard TensorFlow programming environment, a quantized variant is obtained by resorting to the TensorFlow Lite extension, which converts the NN model and casts data types into an MCU–like format, allowing it to be run directly on sensor. In our specific use case, the sensor–near and real–time functionalities of the Arduino board were simulated by pre–loading the modal features extracted at the end of the feature tracking step into the non–volatile memory of the device. Such a framework is conceived to meet the typical procedure applied in the SHM context, in which an initial and offline phase of structural characterization is executed to derive a baseline, then followed by online structural diagnosis and prognosis. Here, they correspond to the training/validation and testing of the TinyML deployment process, respectively.



Figure 4.19: Sequence of steps to be implemented to transform NN architectures from Cloud/Server–based Tensorflow programming to MCU–compliant ML models passing through Tensorflow Lite quantization.

Results

Results for the implementation on the Arduino board are summarized in Tab. 4.3, in which the standard classification scores [188], i.e., accuracy, precision, recall and F1, have been computed together with other remarkable performance metrics, such as the execution time, the model size and the number of hyperparameters. Noteworthy, the TinyML approach proves to be highly robust with respect to rounding effects, data cast and quantization that were necessary implied by the TFLite converter. As can be observed, a negligible impact on the classification metrics is exhibited while moving from TF to Arduino, with a maximum decrease of less than one point percentage for all the four metrics, which consistently remains above 94%.

Table 4.3: Performance metrics of OCCNN model while moving from cloud-based TF to Arduino: beside the classical classification scores, the overall complexity in terms of memory consumption, number of hyperparameters and execution time, are enclosed.

Model size [kB]	13.232
Hyperparameters	2852
Execution time [ms]	1525
Accuracy [%]	
TensorFlow	96.60
TensorFlow Lite	95.95
Arduino 33 BLE Sense	95.73
Precision [%]	
TensorFlow	95.18
TensorFlow Lite	94.36
Arduino 33 BLE Sense	94.12
Recall [%]	
TensorFlow	100
TensorFlow Lite	100
Arduino 33 BLE Sense	99.93
F1 [%]	
TensorFlow	97.53
TensorFlow Lite	97.10
Arduino 33 BLE Sense	96.94

On another side, it is worth mentioning that the model complexity of the OCCNN architecture is interestingly low, showing a memory occupancy around a dozen of kB, a condition which makes its embodiment on the selected prototyping device feasible.

Similarly, the measured execution time of 1525 ms for a total of 1561 testing instances led to an single inference time of less than 1 ms, hence being absolutely compliant with typical duty cycle to be respected in the SHM scenario.

4.5 Conclusions

The research described in this last Chapter concerns the suitability of a hierarchical SHM architecture combining hardware-oriented CS strategies with conventional modal analysis procedures for the long-term and cost-effective diagnostics of aging structures. An experimental campaign conducted on a pinned-pinned steel beam revealed that vibration data can be compressed up to one fourth while attaining a modal shape reconstruction accuracy of 90% or more. Additional considerations can be found in [P13] and in [P14] about compressed data noise immunity.

Later this work dealt with comparison the effectiveness of three iterative data recovery algorithms in the context of CS-based vibration diagnostics in view of hardware-oriented implementations. The OMP, CoSaMP and IHT strategies were specifically investigated, and their performance were quantified on the basis of memory occupancy, processing time and reconstruction accuracy. Results deriving from in-field data show that the OMP algorithm is a suitable candidate to effectively compress vibration signals while preserving meaningful information.

The SHM Smart Sensor Network used in the first part was subsequently employed for a computer science research application, with a preliminary study [P15], then we tackled the interoperability and management issue in IoT-based Condition Monitoring applications and we provided a concrete experience on how an established baseline has been improved through the development of engineering tools. In practice, the usage of such tools guarantees an increased automation in the engineering process of the whole use case, thus reducing operational costs, as well as facilitating the inclusion of third-party legacy devices. Both the Eclipse Arrowhead framework and the WoT paradigm have been used extensively in conjunction.

In parallel with the use of the SHM SSN, a novel sensor node featuring advanced signal processing capabilities for vibration-based monitoring has been presented. From a hardware standpoint, the device is peculiar in that it presents an efficient triggering mechanism based on the coordination of a low-power wake-up accelerometers mastering a second, ultra-low noise density, high-performance and energy-hungry MEMS accelerometer. The SN also integrates a dedicated library for streaming vibration data processing, implementing System Identification algorithms. The synergistic combination of hardware and firmware components proved to be highly accurate in tracking the damage status of a laboratory steel beam under different working configurations.

Finally, a TinyML-enabled framework for vibration-based structural assessment is proposed, specifically resorting to the very recent OCCNN architecture. To this end, the embodiment of the latter NN model on an edge device (i.e., the Arduino Nano 33 BLE sense board) is tackled from a practical perspective and validated in the context of the

Z24 bridge use-case. The promising classification results corroborated by scores always above 94% paves the way to an efficient and reliable accurate diagnostic framework driven by TinyML. The combination of this approach and the first CS analysis has led to results published in [P16].

Conclusions

All the activities reported in this Thesis led to the successful realization of embedded systems which meet the specifications set by the many partners with whom I have collaborated. The reported design examples allow me to emphasize how, in many fields, there is an extreme need for experts capable to build ad-hoc electronic smart systems to ease the development of prototypes for academic departments' research, or industrial partners R&D teams.

My contribution was principally related to the design and development of the hardware and firmware parts. Whereas, concerning the implementation of data processing, in some projects, I actively participated, in others I gave my support in the development computational resources administration, or in the exploitation of specific MCU features for math operations (*e.g.* Digital Signal Processing functions for Cortex-M and Cortex-A microcontroller based devices).

In more detail, in the precision agriculture activity I participated in the choice of electronic components and in the firmware developing.

In the bioengineering projects, I have conducted autonomously the first activity related to the development of a vascular phantom setup and I lead the design and realization of the electronic boards in the other two activities. Besides the hardware design, I have realized the firmware of each systems managing threads such as on-board processing (*e.g.* sensor fusion for crutches orientation, digital filtering for auscultation), and the communication with host devices. In addition, in the last activity about auscultation device realization, I went very deep into auscultation techniques and contact microphones study.

For the automotive project related to the inner electronic motor temperature monitoring, I lead the research group including the industrial partner and the first prototype was totally designed and developed by me. For the second generation of the device, I supervised the project but, in the design phase, I benefited from a contribution of the partner's R&D team.

Finally, concerning the most relevant part of my Thesis about SHM, I was firstly involved in the use and study of a wired Smart Sensor Network. Such experience led me

to develop my own Wireless Sensor Network for Condition Monitoring. The new network development involved also the study of Energy Harvesting solutions and the complete design and development of both hardware and software.

Concerning software, I developed the firmware for the embedded system itself, and also the Cluster Head software (a Personal Computer, or Single Board Computer) with the programming of Matlab, and Python tools. This Thesis presents only a prototype of this network in Section 4.3 because the developments that followed are under patent application requested by an interested industrial partner.

Concerning the on-board processing I gave my support: i) in the study of CS compression and decompression, ii) I programmed the data gathering part for the SysId task, and iii) I participated in the investigation of the Arduino board, Tensor Flow framework and Colab training and modelling in the TinyML study.

Finally, in all these activity, I participated to the field tests for the experimental validation.

Copyright

In reference to IEEE copyrighted material which is used with permission in this thesis, the IEEE does not endorse any of University of Bologna's products or services. Internal or personal use of this material is permitted. If interested in reprinting/republishing IEEE copyrighted material for advertising or promotional purposes or for creating new collective works for resale or redistribution, please go to http://www.ieee.org/publications_standards/publications/rights/rights_link.html to learn how to obtain a License from RightsLink.

Author's publications

- [P1] Lorenzo Mistral Peppi, Matteo Zauli, Luigi Manfrini, Pier Andrea Traverso, Luca Corelli Grappadelli, and Luca De Marchi. “A Low-Cost and High-Accuracy Non-Invasive System for the Monitoring of Fruit Growth”. In: *2020 IEEE International Workshop on Metrology for Agriculture and Forestry (MetroAgriFor)*. IEEE. 2020, pp. 18–23.
- [P2] Lorenzo Mistral Peppi, Matteo Zauli, Luigi Manfrini, Luca Corelli Grappadelli, Luca De Marchi, and Pier Andrea Traverso. “Implementation and Calibration of a Low-Cost Sensor Node for High-Resolution, Continuous and No-Manning Recording of Fruit Growth”. In: *2021 IEEE International Instrumentation and Measurement Technology Conference (I2MTC)*. IEEE. 2021, pp. 1–6.
- [P3] Matteo Zauli, Cristiana Corsi, and Luca De Marchi. “Design and Prototype Development of a Low-Cost Blood Flow Simulator for Vascular Phantoms”. In: *2019 Computing in Cardiology (CinC)*. IEEE. 2019, Page–1.
- [P4] Matteo Zauli, Lorenzo Mistral Peppi, Luca Di Bonaventura, Valerio Antonio Arcobelli, Sabato Mellone, and Luca De Marchi. “To make an Electronic Stethoscope it takes microphone: mic technologies comparison for auscultation device”. In: *Sensors* (2023). To be submitted.
- [P5] Valerio Antonio Arcobelli, Matteo Zauli, Giulia Galteri, Luca Cristofolini, Lorenzo Chiari, Angelo Cappello, Luca De Marchi, and Sabato Mellone. “mCrutch: A Novel m-Health Approach Supporting Continuity of Care”. In: *Sensors* 23.8 (2023), p. 4151.
- [P6] Igor Valič, Matteo Zauli, Nicola Matteazzi, Gianluca Foffano, and Luca De Marchi. “A Wireless System for inner Temperature Measurement of High Speed Electric Motors”. In: *2021 IEEE International Workshop on Metrology for Automotive (MetroAutomotive)*. IEEE. 2021, pp. 248–253.
- [P7] Mariano Nerone, Igor Valič, Matteo Zauli, Alberto Leonardi, Nicola Matteazzi, and Luca De Marchi. “A Wirelessly-Powered Embedded System for Temperature Measurements of a High Performance Electric Motor Rotor”. In: *2022 IEEE Inter-*

- national Workshop on Metrology for Automotive (MetroAutomotive)*. IEEE. 2022, pp. 6–11.
- [P8] Matteo Zauli, Federica Zonzini, Nicola Testoni, Alessandro Marzani, and Luca De Marchi. “Compressive Sensing and On-Board Data Recovery for Vibration-Based SHM”. In: *European Workshop on Structural Health Monitoring: Special Collection of 2020 Papers-Volume 1*. Springer. 2021, pp. 327–334.
- [P9] Matteo Zauli, Federica Zonzini, Valerio Coppola, Vasilis Dertimanis, Eleni Chatzi, Nicola Testoni, and Luca De Marchi. “A Novel Smart Sensor Node with Embedded Signal Processing Functionalities Addressing Vibration-Based Monitoring”. In: *European Workshop on Structural Health Monitoring: EWSHM 2022-Volume 3*. Springer. 2022, pp. 1000–1008.
- [P10] Federica Zonzini, Matteo Zauli, Antonio Carbone, Francesca Romano, Nicola Testoni, and Luca De Marchi. “Hardware-Oriented Data Recovery Algorithms for Compressed Sensing-Based Vibration Diagnostics”. In: *Applications in Electronics Pervading Industry, Environment and Society: APPLEPIES 2020 8*. Springer. 2021, pp. 69–75.
- [P11] Federica Zonzini, Francesca Romano, Antonio Carbone, Matteo Zauli, and Luca De Marchi. “Enhancing vibration-based structural health monitoring via edge computing: A tiny machine learning perspective”. In: *Quantitative Nondestructive Evaluation*. Vol. 85529. American Society of Mechanical Engineers. 2021, V001T07A004.
- [P12] Federico Montori, Ivan Zyrianoff, Lorenzo Gigli, Alessandro Calvio, Riccardo Venanzi, Simone Sindaco, Luca Sciullo, Federica Zonzini, Matteo Zauli, Nicola Testoni, et al. “An IoT Toolchain Architecture for Planning, Running and Managing a Complete Condition Monitoring Scenario”. In: *IEEE Access* (2023).
- [P13] Federica Zonzini, Matteo Zauli, Mauro Mangia, Nicola Testoni, and Luca De Marchi. “Model-assisted compressed sensing for vibration-based structural health monitoring”. In: *IEEE Transactions on Industrial Informatics* 17.11 (2021), pp. 7338–7347.
- [P14] Federica Zonzini, Matteo Zauli, Mauro Mangia, Nicola Testoni, and Luca De Marchi. “HW-Oriented Compressed Sensing for Operational Modal Analysis: The Impact of Noise in MEMS Accelerometer Networks”. In: *2021 IEEE Sensors Applications Symposium (SAS)*. IEEE. 2021, pp. 1–5.

- [P15] Federico Montori, Ivan Zyrianoff, Lorenzo Gigli, Riccardo Venanzi, Simone Sindaco, Cristiano Aguzzi, Federica Zonzini, Matteo Zauli, Nicola Testoni, Enrico Alessi, et al. “A Toolchain Architecture for Condition Monitoring Using the Eclipse Arrowhead Framework”. In: *IECON 2021–47th Annual Conference of the IEEE Industrial Electronics Society*. IEEE. 2021, pp. 1–6.
- [P16] Federica Zonzini, Antonio Carbone, Francesca Romano, Matteo Zauli, and Luca De Marchi. “Machine learning meets compressed sensing in vibration-based monitoring”. In: *Sensors* 22.6 (2022), p. 2229.

Bibliography

- [1] Matthieu De Clercq, Anshu Vats, and Alvaro Biel. “Agriculture 4.0: The future of farming technology”. In: *Proceedings of the World Government Summit, Dubai, UAE* (2018), pp. 11–13.
- [2] David Christian Rose and Jason Chilvers. “Agriculture 4.0: Broadening responsible innovation in an era of smart farming”. In: *Frontiers in Sustainable Food Systems* 2 (2018), p. 87.
- [3] Burak Ozdogan, Anil Gacar, and Huseyin Aktas. “Digital agriculture practices in the context of agriculture 4.0”. In: *Journal of Economics Finance and Accounting* 4.2 (2017), pp. 186–193.
- [4] Mark Shepherd, James A Turner, Bruce Small, and David Wheeler. “Priorities for science to overcome hurdles thwarting the full promise of the ‘digital agriculture’ revolution”. In: *Journal of the Science of Food and Agriculture* (2018).
- [5] Remi Schmaltz. “What is precision agriculture”. In: *Retrieved July 12* (2017), p. 2018.
- [6] Abhishek Khanna and Sanmeet Kaur. “Evolution of Internet of Things (IoT) and its significant impact in the field of Precision Agriculture”. In: *Computers and electronics in agriculture* 157 (2019), pp. 218–231.
- [7] A Knierim, F Borges, M Kernecker, T Kraus, A Wurbs, et al. “What drives adoption of smart farming technologies? Evidence from a cross-country study”. In: *Proceedings of the European International Farm Systems Association Symposium, Chania, Greece*. 2018, pp. 1–5.
- [8] Alexandra Boini, Luigi Manfrini, Gianmarco Bortolotti, Luca Corelli-Grappadelli, and Brunella Morandi. “Monitoring fruit daily growth indicates the onset of mild drought stress in apple”. In: *Scientia Horticulturae* 256 (2019), p. 108520.
- [9] J Tromp. “Diurnal fruit shrinkage in apple as affected by leaf water potential and vapour pressure deficit of the air”. In: *Scientia horticulturae* 22.1-2 (1984), pp. 81–87.

- [10] Betty Klepper, V Douglas Browning, and Howard M Taylor. “Stem diameter in relation to plant water status”. In: *Plant Physiology* 48.6 (1971), pp. 683–685.
- [11] Brunella Morandi, Luigi Manfrini, Marco Zibordi, Massimo Noferini, Giovanni Fiori, and Luca Corelli Grappadelli. “A low-cost device for accurate and continuous measurements of fruit diameter”. In: *HortScience* 42.6 (2007), pp. 1380–1382.
- [12] SO Link, ME Thiede, and MG van Bavel. “An improved strain-gauge device for continuous field measurement of stem and fruit diameter”. In: *Journal of Experimental Botany* 49.326 (1998), pp. 1583–1587.
- [13] Ronald H Sauer, Peter A Beedlow, et al. *Electronic dendrometer*. US Patent 4,549,355. Oct. 1985.
- [14] Martin Thalheimer. “A new optoelectronic sensor for monitoring fruit or stem radial growth”. In: *Computers and Electronics in Agriculture* 123 (2016), pp. 149–153.
- [15] *Rotary Position Sensor - PHS11 Series*. URL: <https://www.ttelectronics.com/TTElectronics/media/ProductFiles/Potenti%5C%5Cometers/Datasheets/PHS11.pdf>.
- [16] *Technical data sheet - ABSpeciale*. URL: <https://www.filoalfa3d.com/upload/scheda/tds-abspeciale-nov-2016.pdf>.
- [17] *SX1272 mbed Shield*. URL: <https://os.mbed.com/components/SX1272MB2xAS/>.
- [18] *SX1272 datasheet*. URL: <https://www.semtech.com/products/wireless-rf/loracore/sx1272%5C#download-resources>.
- [19] *LD39050 500 mA low quiescent current and low noise voltage regulator*. URL: <https://www.st.com/resource/en/datasheet/ld39050.pdf>.
- [20] *MIC5365-3.3YD5-TR High Performance Single 150mA LDO*. URL: <https://www.microchipdirect.com/product/MIC5365-3.3YD5-TR>.
- [21] *STEVAl-ISV012V1, Data brief, STMicroelectronics*. URL: https://www.st.com/resource/en/data%5C_brief/steval-isv012v1.pdf.
- [22] *SPV1040 high efficiency solar battery charger with embedded MPPT*. URL: <https://www.st.com/en/power-management/spv1040.html>.
- [23] *L6924D battery charger*. URL: <https://www.st.com/en/power-management/spv1040.html>.
- [24] *microSD Card Power Consumption & SPI Performance*. URL: <https://goughlui.com/2021/02/27/experiment-microsd-card-power-consumption-spi-performance/>.

- [25] AN Lakso, L Corelli Grappadelli, J Barnard, and MC Goffinet. “An expolinear model of the growth pattern of the apple fruit”. In: *Journal of Horticultural Science* 70.3 (1995), pp. 389–394.
- [26] Charlotte Pratt. “Apple flower and fruit: morphology and anatomy”. In: *Horticultural Reviews* 10 (), pp. 273–308.
- [27] Rodrigo Wolff Porto, Valner J Brusamarello, Ivan Müller, Fabian Leonardo Cabrera Riano, and Fernando Rangel De Sousa. “Wireless power transfer for contactless instrumentation and measurement”. In: *IEEE Instrumentation & Measurement Magazine* 20.4 (2017), pp. 49–54.
- [28] *Galli Genviro 060 climatic chamber*. URL: <https://www.galli2europe.com/wp-content/uploads/2016/08/Galli-Climatic-Genviro-Ver151012-1.pdf>.
- [29] Chung Kit Ho, Adrian JY Chee, Billy YS Yiu, Anderson CO Tsang, Kwok Wing Chow, and CH Alfred. “Wall-less flow phantoms with tortuous vascular geometries: Design principles and a patient-specific model fabrication example”. In: *IEEE Transactions on Ultrasonics, Ferroelectrics, and Frequency Control* 64.1 (2016), pp. 25–38.
- [30] Francesca Galluzzo, Filippo Leonardo, Alessandro Ceruti, Luca De Marchi, and Cristiana Corsi. “Design of anthropomorphic atherosclerotic carotid artery flow phantoms for ultrasound images”. In: *2015 Computing in Cardiology Conference (CinC)*. IEEE. 2015, pp. 721–724.
- [31] Sita Drost, Bastiaan J de Kruif, and David Newport. “Arduino control of a pulsatile flow rig”. In: *Medical Engineering and Physics* 51 (2018), pp. 67–71.
- [32] Mohammad Reza Najjari and Michael W Plesniak. “PID controller design to generate pulsatile flow rate for in vitro experimental studies of physiological flows”. In: *Biomedical Engineering Letters* 7.4 (2017), pp. 339–344.
- [33] Peter R Culmer, Peter C Brooks, Daniella N Strauss, Denise H Ross, Martin C Levesley, Rory J O’Connor, and Bipin B Bhakta. “An instrumented walking aid to assess and retrain gait”. In: *IEEE/ASME Transactions on Mechatronics* 19.1 (2012), pp. 141–148.
- [34] Lisa I Iezzoni, Ellen P McCarthy, Roger B Davis, and Hilary Siebens. “Mobility impairments and use of screening and preventive services.” In: *American journal of public health* 90.6 (2000), p. 955.
- [35] Yasemin P Demir and Sibel A Yildirim. “Different walk aids on gait parameters and kinematic analysis of the pelvis in patients with Adult Neuromuscular Disease”. In: *Neurosciences Journal* 24.1 (2019), pp. 36–44.

- [36] Donald Lloyd-Jones, Robert Adams, Mercedes Carnethon, Giovanni De Simone, T Bruce Ferguson, Katherine Flegal, Earl Ford, Karen Furie, Alan Go, Kurt Greenlund, et al. “American heart association statistics committee and stroke statistics subcommittee”. In: *Heart disease and stroke statistics—2009 update: a report from the American Heart Association Statistics Committee and Stroke Statistics Subcommittee*. *Circulation* 119.3 (2009), pp. 480–486.
- [37] Kim Bertrand, Marie-Hélène Raymond, William C Miller, Kathleen A Martin Ginis, and Louise Demers. “Walking aids for enabling activity and participation: a systematic review”. In: *American Journal of Physical Medicine & Rehabilitation* 96.12 (2017), pp. 894–903.
- [38] Fatemeh Rasouli and Kyle B Reed. “Walking assistance using crutches: a state of the art review”. In: *Journal of biomechanics* 98 (2020), p. 109489.
- [39] William A Satariano, Jack M Guralnik, Richard J Jackson, Richard A Marottoli, Elizabeth A Phelan, and Thomas R Prohaska. “Mobility and aging: new directions for public health action”. In: *American journal of public health* 102.8 (2012), pp. 1508–1515.
- [40] World Health Organization. *Ageing and Health*. <https://www.who.int/news-room/fact-sheets/detail/ageing-and-health>. [Online; accessed 20-February-2023]. 2023.
- [41] Lisa Lighthall Haubert, Dee D Gutierrez, Craig J Newsam, JoAnne K Gronley, Sara J Mulroy, and Jacquelin Perry. “A comparison of shoulder joint forces during ambulation with crutches versus a walker in persons with incomplete spinal cord injury”. In: *Archives of physical medicine and rehabilitation* 87.1 (2006), pp. 63–70.
- [42] George G Deaver. “Posture and its relation to mental and physical health”. In: *Research Quarterly. American Physical Education Association* 4.1 (1933), pp. 221–228.
- [43] TY Chung. “Lower limb orthoses”. In: *Braddom’s Rehabilitation Care: A Clinical Handbook; Elsevier: Amsterdam, The Netherlands* (2018), pp. 75–84.
- [44] *Physiopedia*. <https://www.physio-pedia.com/Crutches>. [Online; accessed 27-January-2023]. 2023.
- [45] WMQ Yap, Z Hairodin, and EBK Kwek. “Axillary versus Forearm Crutches: A Prospective Cohort Comparing which is Superior for 3-Point Crutch Gait”. In: *Malaysian Orthopaedic Journal* 15.2 (2021), p. 36.

- [46] Frederick W Van Hook, Dale Demonbreun, and Barry D Weiss. “Ambulatory devices for chronic gait disorders in the elderly”. In: *American family physician* 67.8 (2003), pp. 1717–1724.
- [47] Dena Gardiner. *The principles of exercise therapy 4 th ed.* 2000.
- [48] H Stephen Kaye, Taewoon Kang, and Mitchell P LaPlante. *Mobility device use in the United States*. Vol. 14. National Institute on Disability and Rehabilitation Research, US Department . . . , 2000.
- [49] Henri L Hurkmans, Johannes B Bussmann, and Eric Benda. “Validity and interobserver reliability of visual observation to assess partial weight-bearing”. In: *Archives of physical medicine and rehabilitation* 90.2 (2009), pp. 309–313.
- [50] E Viehweger, L Zürcher Pfund, M Hélix, M-A Rohon, M Jacquemier, D Scavarda, J-L Jouve, G Bollini, A Loundou, and M-C Simeoni. “Influence of clinical and gait analysis experience on reliability of observational gait analysis (Edinburgh Gait Score Reliability)”. In: *Annals of physical and rehabilitation medicine* 53.9 (2010), pp. 535–546.
- [51] Xianggang Zhang, Zenghe Xiang, Qingxia Lin, and Qifang Zhou. “The design and development of a lower limbs rehabilitation exoskeleton suit”. In: *2013 ICME International Conference on Complex Medical Engineering*. IEEE. 2013, pp. 307–312.
- [52] Geoff V Merrett, Christian Peters, Georgina Hallet, and Neil M White. “An instrumented crutch for monitoring patients’ weight distribution during orthopaedic rehabilitation”. In: *Procedia Chemistry* 1.1 (2009), pp. 714–717.
- [53] E Sardini, M Serpelloni, M Lancini, and S Pasinetti. “Wireless instrumented crutches for force and tilt monitoring in lower limb rehabilitation”. In: *Procedia Engineering* 87 (2014), pp. 348–351.
- [54] Federica Tamburella, Matteo Lorusso, Nevio Luigi Tagliamonte, Francesca Bentivoglio, Alessandra Bigioni, Iolanda Pisotta, Matteo Lancini, Simone Pasinetti, Marco Ghidelli, Marcella Masciullo, et al. “Load auditory feedback boosts crutch usage in subjects with central nervous system lesions: A pilot study”. In: *Frontiers in Neurology* 12 (2021), p. 700472.
- [55] Marien Narváez and Joan Aranda. “Gait patterns monitoring using instrumented forearm crutches”. In: *Computers Helping People with Special Needs: 17th International Conference, ICCHP 2020, Lecco, Italy, September 9–11, 2020, Proceedings, Part II 17*. Springer. 2020, pp. 402–410.

- [56] Asier Brull, Asier Zubizarreta, Itziar Cabanes, and Ana Rodriguez-Larrad. “Sensorized tip for monitoring people with multiple sclerosis that require assistive devices for walking”. In: *Sensors* 20.15 (2020), p. 4329.
- [57] Mattia Corzani. “mHealth Apps for Older Adults and persons with Parkinson’s Disease”. In: *Internet of Things for Human-Centered Design: Application to Elderly Healthcare*. Springer, 2022, pp. 233–259.
- [58] Daniele Giansanti. “The Role of the mHealth in the Fight against the Covid-19: Successes and Failures”. In: *Healthcare*. Vol. 9. 1. MDPI. 2021, p. 58.
- [59] Karthikeyan Iyengar, Gaurav K Upadhyaya, Raju Vaishya, and Vijay Jain. “COVID-19 and applications of smartphone technology in the current pandemic”. In: *Diabetes & Metabolic Syndrome: Clinical Research & Reviews* 14.5 (2020), pp. 733–737.
- [60] Long Chiau Ming, Noorazrina Untong, Nur Amalina Aliudin, Norliza Osili, Nuro-laini Kifli, Ching Siang Tan, Khang Wen Goh, Pit Wei Ng, Yaser Mohammed Al-Worafi, Kah Seng Lee, et al. “Mobile health apps on COVID-19 launched in the early days of the pandemic: content analysis and review”. In: *JMIR mHealth and uHealth* 8.9 (2020), e19796.
- [61] Shaoxiong Sun, Amos A Folarin, Yatharth Ranjan, Zulqarnain Rashid, Pauline Conde, Callum Stewart, Nicholas Cummins, Faith Matcham, Gloria Dalla Costa, Sara Simblett, et al. “Using smartphones and wearable devices to monitor behavioral changes during COVID-19”. In: *Journal of medical Internet research* 22.9 (2020), e19992.
- [62] Zartashia Ghani, Johan Jarl, Johan Sanmartin Berglund, Martin Andersson, and Peter Anderberg. “The cost-effectiveness of mobile health (mHealth) interventions for older adults: Systematic review”. In: *International Journal of Environmental Research and Public Health* 17.15 (2020), p. 5290.
- [63] *RS Pro Rechargeable Lithium ion battery*. URL: <https://docs.rs-online.com/cd82/A700000009044205.pdf>.
- [64] *RP2040 - A microcontroller by Raspberry Pi*. URL: <https://datasheets.raspberrypi.com/rp2040/rp2040-datasheet.pdf>.
- [65] *LSM6DSOX - System-in-package featuring a 3D digital accelerometer and a 3D digital gyroscope*. URL: <https://www.st.com/en/mems-and-sensors/lsm6dsox.html>.

- [66] *MCP73831/2 - Miniature single-cell charge management controllers*. URL: <https://ww1.microchip.com/downloads/aemDocuments/documents/APID/ProductDocuments/DataSheets/MCP73831-Family-Data-Sheet-DS20001984H.pdf>.
- [67] *FX293X-100A-0100-L*. URL: <https://www.te.com/usa-en/product-20009605-15.html>.
- [68] Sebastian Madgwick et al. “An efficient orientation filter for inertial and inertial/magnetic sensor arrays”. In: *Report x-io and University of Bristol (UK)* 25 (2010), pp. 113–118.
- [69] *SMART-DX EVO*. <https://www.btsbioengineering.com/products/smart-dx-evo/>. BTS Bioengineering.
- [70] Aida M Valevicius, Peter Y Jun, Jacqueline S Hebert, and Albert H Vette. “Use of optical motion capture for the analysis of normative upper body kinematics during functional upper limb tasks: A systematic review”. In: *Journal of electromyography and kinesiology* 40 (2018), pp. 1–15.
- [71] Inge Söderkvist and Per-Åke Wedin. “Determining the movements of the skeleton using well-configured markers”. In: *Journal of biomechanics* 26.12 (1993), pp. 1473–1477.
- [72] Malay Sarkar, Irappa Madabhavi, Narasimhalu Niranjana, and Megha Dogra. “Auscultation of the respiratory system”. In: *Annals of thoracic medicine* 10.3 (2015), p. 158.
- [73] Vlad Voin, Rod J Oskouian, Marios Loukas, and R Shane Tubbs. “Auscultation of the heart: the basics with anatomical correlation”. In: *Clinical Anatomy* 30.1 (2017), pp. 58–60.
- [74] Muhammad EH Chowdhury, Amith Khandakar, Khawla Alzoubi, Samar Mansoor, Anas M. Tahir, Mamun Bin Ibne Reaz, and Nasser Al-Emadi. “Real-time smart-digital stethoscope system for heart diseases monitoring”. In: *Sensors* 19.12 (2019), p. 2781.
- [75] Rangaraj M Rangayyan. *Biomedical signal analysis*. John Wiley & Sons, 2015.
- [76] V Nivitha Varghees and KI Ramachandran. “A novel heart sound activity detection framework for automated heart sound analysis”. In: *Biomedical Signal Processing and Control* 13 (2014), pp. 174–188.
- [77] Abraham Bohadana, Gabriel Izbicki, and Steve S Kraman. “Fundamentals of lung auscultation”. In: *New England Journal of Medicine* 370.8 (2014), pp. 744–751.
- [78] F Dalmay, MT Antonini, P Marquet, and R Menier. “Acoustic properties of the normal chest”. In: *European Respiratory Journal* 8.10 (1995), pp. 1761–1769.

- [79] Steffen Kreikemeier, Sabine Margolf-Hackl, J Raether, E Fichtl, and J Kiessling. “Comparison of different directional microphone technologies for moderate-to-severe hearing loss”. In: *Hear. Rev* 20 (2013), pp. 44–45.
- [80] Caitlin N Teague, Sinan Hersek, Hakan Töreyn, Mindy L Millard-Stafford, Michael L Jones, Géza F Kogler, Michael N Sawka, and Omer T Inan. “Novel methods for sensing acoustical emissions from the knee for wearable joint health assessment”. In: *IEEE Transactions on Biomedical Engineering* 63.8 (2016), pp. 1581–1590.
- [81] Anders Askenfelt, Jan Gauffin, Johan Sundberg, and Peter Kitzing. “A comparison of contact microphone and electroglottograph for the measurement of vocal fundamental frequency”. In: *Journal of Speech, Language, and Hearing Research* 23.2 (1980), pp. 258–273.
- [82] Alessio Carullo, Federico Casassa, Antonella Castellana, Arianna Astolfi, Lorenzo Pavese, and Giuseppina Emma Puglisi. “Performance comparison of different contact microphones used for voice monitoring”. In: *Proceedings of the International Congress on Sound and Vibration*. Vol. 22. 2015, pp. 12–16.
- [83] Peter V Loeppert and Sung B Lee. “SiSonic™-The first commercialized MEMS microphone”. In: *Proceedings of the Solid-State Sensors, Actuators, and Microsystems Workshop*. 2006, pp. 27–30.
- [84] Madhubabu Anumukonda, Swathi Ramasahayam, LVR Prasada Raju, and Shubhajit Roy Chowdhury. “Detection of cardio auscultation using MEMS microphone”. In: *2015 9th International Conference on Sensing Technology (ICST)*. IEEE. 2015, pp. 173–177.
- [85] Rinat K Kusainov and Vladimir K Makukha. “Evaluation of the applicability of MEMS microphone for auscultation”. In: *2015 16th International Conference of Young Specialists on Micro/Nanotechnologies and Electron Devices*. IEEE. 2015, pp. 595–597.
- [86] Michael Klum, Fabian Leib, Casper Oberschelp, David Martens, Alexandru-Gabriel Pielmus, Timo Tigges, Thomas Penzel, and Reinhold Orglmeister. “Wearable multimodal stethoscope patch for wireless biosignal acquisition and long-term auscultation”. In: *2019 41st Annual International Conference of the IEEE Engineering in Medicine and Biology Society (EMBC)*. IEEE. 2019, pp. 5781–5785.
- [87] Sung Hoon Lee, Yun-Soung Kim, Min-Kyung Yeo, Musa Mahmood, Nathan Zavanelli, Chaeuk Chung, Jun Young Heo, Yoonjoo Kim, Sung-Soo Jung, and Woon-Hong Yeo. “Fully portable continuous real-time auscultation with a soft wearable

- stethoscope designed for automated disease diagnosis”. In: *Science Advances* 8.21 (2022), eabo5867.
- [88] Murata. *Piezoelectric Diaphragms*. <https://www.murata.com/en-global/products/sound/diaphragm>. [Online; accessed 28-February-2023]. 2023.
- [89] Y Yasuno and Y Riko. “A chronological review of production and applications of electret condenser microphone for consumer use”. In: *Proceedings of 8th International Symposium on Electrets (ISE 8)*. IEEE. 1994, pp. 943–948.
- [90] Jerad Lewis. “Analog and digital MEMS microphone design considerations”. In: *Technical Article MS-2472. Analog Devices* (2013).
- [91] Sung Hoon Lee, Yun-Soung Kim, and Woon-Hong Yeo. “Advances in microsensors and wearable bioelectronics for digital stethoscopes in health monitoring and disease diagnosis”. In: *Advanced Healthcare Materials* 10.22 (2021), p. 2101400.
- [92] Supreeya Swarup and Amgad N Makaryus. “Digital stethoscope: Technology update”. In: *Medical Devices: Evidence and Research* (2018), pp. 29–36.
- [93] Aparna Lakhe, Isha Sodhi, Jyothi Warriar, and Vineet Sinha. “Development of digital stethoscope for telemedicine”. In: *Journal of medical engineering & technology* 40.1 (2016), pp. 20–24.
- [94] Ian McLane, Dimitra Emmanouilidou, James E West, and Mounya Elhilali. “Design and comparative performance of a robust lung auscultation system for noisy clinical settings”. In: *IEEE journal of biomedical and health informatics* 25.7 (2021), pp. 2583–2594.
- [95] Pengcheng Shi, Yirui Li, Wendong Zhang, Guojun Zhang, Jiangong Cui, Shuotong Wang, and Bo Wang. “Design and Implementation of Bionic MEMS Electronic Heart Sound Stethoscope”. In: *IEEE Sensors Journal* 22.2 (2021), pp. 1163–1172.
- [96] *User Manual eKuore*. URL: %5Curl%7Bhttps://drive.google.com/file/d/1B9inPIaAhtvIg8ITtR9AZKS1qFb87j46/view%7D.
- [97] *User Manual ThinklabsOne*. URL: %5Curl%7Bhttps://www.thinklabs.com/_files/ugd/51509e_21101c5aaa294c49a519d6897ad1332a.pdf%7D.
- [98] Ashwin Ramanathan, Lindsay Zhou, Faezeh Marzbanrad, Robert Roseby, Kenneth Tan, Ajay Kevat, and Atul Malhotra. “Digital stethoscopes in paediatric medicine”. In: *Acta Paediatrica* 108.5 (2019), pp. 814–822.
- [99] Stephanie Graceffo, Amyna Husain, Salahuddin Ahmed, Eric D McCollum, and Mounya Elhilali. “Validation of auscultation technologies using objective and clinical comparisons”. In: *2020 42nd Annual International Conference of the IEEE Engineering in Medicine & Biology Society (EMBC)*. IEEE. 2020, pp. 992–997.

- [100] Valerie Rennoll, Ian McLane, Mounya Elhilali, and James E West. “Optimized Acoustic Phantom Design for Characterizing Body Sound Sensors”. In: *Sensors* 22.23 (2022), p. 9086.
- [101] G Drzewiecki, H Katta, Andreas Pfahnl, David Bello, and David Dicken. “Active and passive stethoscope frequency transfer functions: Electronic stethoscope frequency response”. In: *2014 IEEE Signal Processing in Medicine and Biology Symposium (SPMB)*. IEEE. 2014, pp. 1–4.
- [102] Daniel Weiss, Christine Erie, Joseph Butera III, Ryan Copt, Glenn Yeaw, Mark Harpster, James Hughes, and Deeb N Salem. “An in vitro acoustic analysis and comparison of popular stethoscopes”. In: *Medical Devices: Evidence and Research* (2019), pp. 41–52.
- [103] RL Watrous, DM Grove, and DL Bowen. “Methods and results in characterizing electronic stethoscopes”. In: *Computers in cardiology*. IEEE. 2002, pp. 653–656.
- [104] *Murata 7BB-35-3L0 datasheet*. Murata. URL: <https://www.murata.com/en-eu/api/pdfdownloadapi?cate=&partno=7BB-35-3L0%7D>.
- [105] *Primo High sensitivity Electret Condenser Microphone datasheet*. Primo. URL: <https://micbooster.com/datasheets/EM272Z1.pdf%7D>.
- [106] *STMicroelectronics MP23ABS1 datasheet*. <https://www.st.com/resource/en/datasheet/mp23abs1.pdf>. STMicroelectronics.
- [107] *STMicroelectronics IMP34DT05 datasheet*. <https://www.st.com/resource/en/datasheet/imp34dt05.pdf>. STMicroelectronics.
- [108] Kiichi Takahashi, Kyoichi Ono, Hirokazu Arai, Hiroyuki Adachi, Masato Ito, Akie Kato, and Tsutomu Takahashi. “Detection of pathologic heart murmurs using a piezoelectric sensor”. In: *Sensors* 21.4 (2021), p. 1376.
- [109] Anastasiia Makarenkova, Anna Poreva, and Mykola Slozko. “Efficiency evaluation of electroacoustic sensors for auscultation devices of human body life-activity sounds”. In: *2017 IEEE First Ukraine Conference on Electrical and Computer Engineering (UKRCON)*. IEEE. 2017, pp. 310–313.
- [110] *What Are The Parts Of A Stethoscope*. <https://www.excel-medical.com/what-are-the-parts-of-a-stethoscope/>. [Online; accessed 30-January-2023]. 2023.
- [111] Autodesk. *Free web app for 3D design, electronics, and coding*. <https://www.tinkercad.com/>. [Online; accessed 08-February-2023]. 2023.

- [112] Littmann. *3M Littmann Stethoscope Spare Parts Kit Classic III Cardiology IV and CORE, 40016, Black, 10 Kit/Case*. https://www.littmann.com/3M/en_US/littmann-stethoscopes/products/~/3M-Littmann-Stethoscope-Spare-Parts-Kit-Classic-III-Cardiology-IV-and-CORE-40016-Black-10-Kit-Case/?N=5142935+8711017+3290598392&rt=rud. [Online; accessed 08-February-2023]. 2023.
- [113] Texas Instruments. *OPA2197 36-V, Precision, Rail-to-Rail Input/Output, Low Offset Voltage, Operational Amplifiers*. https://www.ti.com/lit/ds/symlink/opa2197.pdf?ts=1675935297682&ref_url=https%253A%252F%252Fwww.ti.com%252Fproduct%252FOPA2197. [Online; accessed 09-February-2023]. 2023.
- [114] Nuri Celik, Ruthsenne Gagarin, Gui Chao Huang, Magdy F Iskander, and Benjamin W Berg. “Microwave stethoscope: Development and benchmarking of a vital signs sensor using computer-controlled phantoms and human studies”. In: *IEEE transactions on Biomedical Engineering* 61.8 (2013), pp. 2341–2349.
- [115] Michael Klum, Julian Stehling, Alexandru Pielmus, Timo Tigges, and Reinhold Orglmeister. “Validation System for Digital Stethoscopes”. In: *Current Directions in Biomedical Engineering* 5.1 (2019), pp. 261–264.
- [116] Bounce Rubber Bands. *Sizing Chart*. <https://www.bouncerrubberbands.com/sizing-chart/>. [Online; accessed 05-April-2023]. 2023.
- [117] *RDNet 4 - RCF sound system management and control software*. URL: <https://www.rcf.it/it/products/product-detail/rdnet>.
- [118] Amirtahà Taebi, Brian E Solar, Andrew J Bomar, Richard H Sandler, and Hansen A Mansy. “Recent advances in seismocardiography”. In: *Vibration* 2.1 (2019), pp. 64–86.
- [119] Pranav Gupta, Mohammad J Moghimi, Yaesuk Jeong, Divya Gupta, Omer T Inan, and Farrokh Ayazi. “Precision wearable accelerometer contact microphones for longitudinal monitoring of mechano-acoustic cardiopulmonary signals”. In: *NPJ digital medicine* 3.1 (2020), p. 19.
- [120] Keya Pandia, Omer T Inan, and Gregory TA Kovacs. “A frequency domain analysis of respiratory variations in the seismocardiogram signal”. In: *2013 35th Annual International Conference of the IEEE Engineering in Medicine and Biology Society (EMBC)*. IEEE. 2013, pp. 6881–6884.
- [121] Panagiotis D Hatziantoniou and John N Mourjopoulos. “Generalized fractional-octave smoothing of audio and acoustic responses”. In: *Journal of the Audio Engineering Society* 48.4 (2000), pp. 259–280.

- [122] Christopher Hummersone. *1/N-Octave Smoothing*. <https://it.mathworks.com/matlabcentral/fileexchange/55161-1-n-octave-smoothing>. [Online; accessed 03-March-2023]. 2023.
- [123] S. Li, B. Sarlioglu, S. Jurkovic, N. R. Patel, and P. Savagian. “Analysis of Temperature Effects on Performance of Interior Permanent Magnet Machines for High Variable Temperature Applications”. In: *IEEE Transactions on Industry Applications* 53.5 (2017).
- [124] D. Kim, D. H. Kang, C. Kim, J. Kim, Y. Kim, and S. Jung. “Operation Characteristic of IPMSM Considering PM Saturation Temperature”. In: *IEEE Transactions on Applied Superconductivity* 30.4 (2020), pp. 1–4.
- [125] Zhi Gao. “Sensorless Stator Winding Temperature Estimation for Induction Machines”. In: (Jan. 2006).
- [126] D. Staton, A. Boglietti, and A. Cavagnino. “Solving the more difficult aspects of electric motor thermal analysis in small and medium size industrial induction motors”. In: *IEEE Transactions on Energy Conversion* (2005), pp. 620–628.
- [127] Marco Cavazzuti, Gloria Gaspari, Stefano Pasquale, and Enrico Stalio. “Thermal management of a Formula E electric motor: Analysis and optimization”. In: *Applied Thermal Engineering* 157 (2019), p. 113733.
- [128] Phuong Thi Luu, Ji-Young Lee, Ji-Heon Lee, and Jung-Woo Park. “Electromagnetic and thermal analysis of permanent-magnet synchronous motors for cooperative robot applications”. In: *IEEE Transactions on Magnetics* 56.3 (2020), pp. 1–4.
- [129] Zhi Gao. “Sensorless stator winding temperature estimation for induction machines”. PhD thesis. Georgia Institute of Technology, 2006.
- [130] M. Kovačić, M. Vražić, and I. Gašparac. “Bluetooth wireless communication and 1-wire digital temperature sensors in synchronous machine rotor temperature measurement”. In: *Proceedings of 14th International Power Electronics and Motion Control Conference EPE-PEMC 2010*. 2010, T7-25-T7-28.
- [131] C. Du-Bar, J. Åström, T. Thiringer, S. Lundmark, and M. Alatalo. “Design of an online temperature monitoring system for an experimental IPMSM”. In: *2016 XXII International Conference on Electrical Machines (ICEM)*. 2016, pp. 1533–1538.
- [132] D. Fernandez, D. Reigosa, T. Tanimoto, T. Kato, and F. Briz. “Wireless permanent magnet temperature field distribution measurement system for IPMSMs”. In: *2015 IEEE Energy Conversion Congress and Exposition (ECCE)*. 2015, pp. 3996–4003.

- [133] D. Park, H. Jung, H. Cho, and S. Sul. “Design of Wireless Temperature Monitoring System for Measurement of Magnet Temperature of IPMSM”. In: *2018 IEEE Transportation Electrification Conference and Expo (ITEC)*. 2018, pp. 656–661.
- [134] Thomas J Bajzek. “Thermocouples: a sensor for measuring temperature”. In: *IEEE Instrumentation & Measurement Magazine* 8.1 (2005), pp. 35–40.
- [135] *Carbolite Gero AX 30 laboratory oven*. URL: <https://www.carbolite-gero.com/products/ovens/laboratory-ovens/ax-laboratory-bench-top-oven/function-features/>.
- [136] *MAX31850/MAX31851 Cold-Junction Compensated, 1-Wire Thermocouple-to-Digital Converters*. URL: <https://datasheets.maximintegrated.com/en/ds/MAX31850-MAX31851.pdf>.
- [137] Nicola Testoni, Cristiano Aguzzi, Valentina Arditi, Federica Zonzini, Luca De Marchi, Alessandro Marzani, and Tullio Salmon Cinotti. “A Sensor Network with Embedded Data Processing and Data-to-Cloud Capabilities for Vibration-Based Real-Time SHM”. In: *Journal of Sensors* (2018).
- [138] Nicola Testoni, Federica Zonzini, Alessandro Marzani, Valentina Scarponi, and Luca De Marchi. “A tilt sensor node embedding a data-fusion algorithm for vibration-based shm”. In: *Electronics* 8.1 (2019), p. 45.
- [139] Sandeep Sony, Shea Laventure, and Ayan Sadhu. “A literature review of next-generation smart sensing technology in structural health monitoring”. In: *Structural Control and Health Monitoring* 26.3 (2019), e2321.
- [140] Mario Paz, Young Hoon Kim, et al. *Structural dynamics*. Springer, 1991.
- [141] Rune Brincker, Lingmi Zhang, and Palle Andersen. “Modal identification of output-only systems using frequency domain decomposition”. In: *Smart materials and structures* 10.3 (2001), p. 441.
- [142] Zilong Zou, Yuequan Bao, Hui Li, Billie F Spencer, and Jinping Ou. “Embedding compressive sensing-based data loss recovery algorithm into wireless smart sensors for structural health monitoring”. In: *IEEE Sensors Journal* 15.2 (2014), pp. 797–808.
- [143] S M O’Connor, J P Lynch, and A C Gilbert. “Compressed sensing embedded in an operational wireless sensor network to achieve energy efficiency in long-term monitoring applications”. In: *Smart Materials and Structures* 23.8 (2014).
- [144] Roman Klis and Eleni N. Chatzi. “Vibration monitoring via spectro-temporal compressive sensing for wireless sensor networks”. In: *Structure and Infrastructure Engineering* 13.1 (2017), pp. 195–209.

- [145] *Arrowhead Tools*. <https://tools.arrowhead.eu/home/>. [Online; accessed 23-January-2023]. 2023.
- [146] Meenu Rani, Sanjay B Dhok, and Raghavendra B Deshmukh. “A systematic review of compressive sensing: Concepts, implementations and applications”. In: *IEEE Access* 6 (2018), pp. 4875–4894.
- [147] Venkata Sainath Gupta Thadikemalla and Abhay S Gandhi. “A data loss recovery technique using compressive sensing for structural health monitoring applications”. In: *KSCE Journal of Civil Engineering* 22.12 (2018), pp. 5084–5093.
- [148] Hongchun Sun, Zhiyuan Wang, and Yong Xu. “Research on sampling of vibration signals based on compressed sensing”. In: *Vibroengineering Procedia* 10 (2016), pp. 459–463.
- [149] Federica Zonzini, Alberto Girolami, Luca De Marchi, Alessandro Marzani, and Davide Brunelli. “Cluster-based Vibration Analysis of Structures with Graph Signal Processing”. In: *IEEE Transactions on Industrial Electronics* (2020).
- [150] Raouf A Ibrahim. *Handbook of Structural Life Assessment*. Wiley Online Library, 2017.
- [151] Randall J Allemang. “The modal assurance criterion—twenty years of use and abuse”. In: *Sound and vibration* 37.8 (2003), pp. 14–23.
- [152] Luigi Atzori, Antonio Iera, and Giacomo Morabito. “Understanding the Internet of Things: definition, potentials, and societal role of a fast evolving paradigm”. In: *Ad Hoc Networks* 56 (2017), pp. 122–140.
- [153] Robert Bond Randall. *Vibration-based condition monitoring: industrial, automotive and aerospace applications*. John Wiley & Sons, 2021.
- [154] Alessandro Pegoretti. “Structural Health Monitoring: Current State and Future Trends”. In: (2018).
- [155] Alessandro Massaro. “Information technology infrastructures supporting Industry 5.0 facilities”. In: (2022).
- [156] Matthias Kovatsch, Ryuichi Matsukura, Michael Lagally, Toru Kawaguchi, Kuni-hiko Toumura, and Kazuo Kajimoto. *Web of Things (WoT) Architecture*. W3C Recommendation. <https://www.w3.org/TR/wot-architecture/>. Apr. 2020.
- [157] Cristiano Aguzzi, Lorenzo Gigli, Luca Sciullo, Angelo Trotta, Federica Zonzini, Luca De Marchi, Marco Di Felice, Alessandro Marzani, and Tullio Salmon Cinotti. “MODRON: A Scalable and Interoperable Web of Things Platform for Structural Health Monitoring”. In: *2021 IEEE 18th Annual Consumer Communications & Networking Conference (CCNC)*. IEEE. 2021, pp. 1–7.

- [158] Gianvito Urgese, Paolo Azzoni, Jan van Deventer, Jerker Delsing, and Enrico Macii. “An Engineering Process model for managing a digitalised life-cycle of products in the Industry 4.0”. In: *NOMS 2020-2020 IEEE/IFIP Network Operations and Management Symposium*. IEEE. 2020, pp. 1–6.
- [159] Géza Kulcsár, Pál Varga, Marek S Tatara, Federico Montori, Michel A Inigo, Gianvito Urgese, and Paolo Azzoni. “Modeling an Industrial Revolution: How to Manage Large-Scale, Complex IoT Ecosystems?” In: *2021 IFIP/IEEE International Symposium on Integrated Network Management (IM)*. IEEE. 2021, pp. 896–901.
- [160] ISO Central Secretary. *Industrial systems, installations and equipment and industrial products — Structuring principles and reference designations*. Standard IEC 81346. Geneva, CH: International Organization for Standardization, 2019. URL: <https://www.iso.org/standard/75265.html>.
- [161] Géza Kulcsár, Marek S Tatara, and Federico Montori. “Toolchain modeling: Comprehensive engineering plans for industry 4.0”. In: *IECON 2020 The 46th Annual Conference of the IEEE Industrial Electronics Society*. IEEE. 2020, pp. 4541–4546.
- [162] Jerker Delsing. *Iot automation: Arrowhead framework*. CRC Press, 2017.
- [163] Géza Kulcsár, Kadosa Koltai, Szvetlin Tanyi, Bálint Péceli, Ákos Horváth, Zoltán Micskei, and Pál Varga. “From models to management and back: Towards a system-of-systems engineering toolchain”. In: *NOMS 2020-2020 IEEE/IFIP Network Operations and Management Symposium*. IEEE. 2020, pp. 1–6.
- [164] Mirco Tarozzi, Giacomo Pignagnoli, and Andrea Benedetti. “Identification of damage-induced frequency decay on a large-scale model bridge”. In: *Engineering Structures* 221 (2020), p. 111039.
- [165] *AIS2IH - MEMS digital output motion sensor: high-performance 3-axis accelerometer for automobile applications*. ST Microelectronics. URL: <https://www.st.com/resource/en/datasheet/ais2ih.pdf>.
- [166] *ADXL354/ADXL355 - Low Noise, Low Drift, Low Power, 3-Axis MEMS Accelerometers*. https://www.analog.com/media/en/technical-documentation/data-sheets/adxl354_adxl355.pdf. Analog Devices.
- [167] *MCP73831/2 Miniature Single-Cell, Fully Integrated Li-Ion, Li-Polymer Charge Management Controllers*. Microchip. URL: <https://ww1.microchip.com/downloads/aemDocuments/documents/APID/ProductDocuments/DataSheets/MCP73831-Family-Data-Sheet-DS20001984H.pdf>.
- [168] *SM141K09L - Monocrystalline Solar Cell 277 mW 6.22 V*. <https://ixapps.ixys.com/DataSheet/SM141K09L.pdf>. ANYSOLAR Ltd.

- [169] Daniel J Apo and Shashank Priya. “High power density levitation-induced vibration energy harvester”. In: *Energy Harvesting and Systems* 1.1-2 (2014), pp. 79–88.
- [170] *LT1302/LT1302-5 - Mmicropower step-up DC/DC converters*. <https://www.analog.com/media/en/technical-documentation/data-sheets/lt1302.pdf>. Linear Technology.
- [171] *S118-J1SS-1808YB - Piezoelectric Bending Transducer*. <https://piezo.com/products/piezoelectric-bending-transducer-s118-j1ss-1808yb>. MIDE Technologies.
- [172] Andrew A Neath and Joseph E Cavanaugh. “The Bayesian information criterion: background, derivation, and applications”. In: *Wiley Interdisciplinary Reviews: Computational Statistics* 4.2 (2012), pp. 199–203.
- [173] Soojin Cho, Chung-Bang Yun, Jerome P Lynch, Andrew T Zimmerman, Billie F Spencer Jr, and Tomonori Nagayama. “Smart wireless sensor technology for structural health monitoring of civil structures”. In: *Steel Structures* 8.4 (2008), pp. 267–275.
- [174] Mohammed Abdulkarem, Khairulmizam Samsudin, Fakhrol Zaman Rokhani, and Mohd Fadlee A Rasid. “Wireless sensor network for structural health monitoring: A contemporary review of technologies, challenges, and future direction”. In: *Structural Health Monitoring* 19.3 (2020), pp. 693–735.
- [175] Fuh-Gwo Yuan, Sakib Ashraf Zargar, Qiuyi Chen, and Shaohan Wang. “Machine learning for structural health monitoring: challenges and opportunities”. In: *Sensors and Smart Structures Technologies for Civil, Mechanical, and Aerospace Systems 2020*. Vol. 11379. International Society for Optics and Photonics. 2020, p. 1137903.
- [176] Ali Moin, Andy Zhou, Abbas Rahimi, Alisha Menon, Simone Benatti, George Alexandrov, Senam Tamakloe, Jonathan Ting, Natasha Yamamoto, Yasser Khan, et al. “A wearable biosensing system with in-sensor adaptive machine learning for hand gesture recognition”. In: *Nature Electronics* 4.1 (2021), pp. 54–63.
- [177] Francesco Alongi, Nicolo Ghielmetti, Danilo Pau, Federico Terraneo, and William Fornaciari. “Tiny Neural Networks for Environmental Predictions: an integrated approach with Miosix”. In: *2020 IEEE International Conference on Smart Computing (SMARTCOMP)*. IEEE. 2020, pp. 350–355.

- [178] Andrea Albanese, Matteo Nardello, and Davide Brunelli. “Automated Pest Detection with DNN on the Edge for Precision Agriculture”. In: *IEEE Journal on Emerging and Selected Topics in Circuits and Systems* (2021).
- [179] Lorenzo Lamberti, Manuele Rusci, Marco Fariselli, Francesco Paci, and Luca Benini. “Low-Power License Plate Detection and Recognition on a RISC-V Multi-Core MCU-based Vision System”. In: *2021 IEEE International Symposium on Circuits and Systems (ISCAS)*. IEEE. 2021, pp. 1–5.
- [180] Carlo Rainieri and Giovanni Fabbrocino. “Operational modal analysis of civil engineering structures”. In: *Springer, New York* 142 (2014), p. 143.
- [181] Elia Favarelli, Enrico Testi, and Andrea Giorgetti. “One class classifier neural network for anomaly detection in low dimensional feature spaces”. In: *2019 13th International Conference on Signal Processing and Communication Systems (ICSPCS)*. IEEE. 2019, pp. 1–7.
- [182] Edwin Reynders, Rik Pintelon, and Guido De Roeck. “Uncertainty bounds on modal parameters obtained from stochastic subspace identification”. In: *Mechanical systems and signal processing* 22.4 (2008), pp. 948–969.
- [183] Greg Hamerly and Charles Elkan. “Learning the k in k-means”. In: *Advances in neural information processing systems* 16 (2004), pp. 281–288.
- [184] Elia Favarelli and Andrea Giorgetti. “Machine Learning for Automatic Processing of Modal Analysis in Damage Detection of Bridges”. In: *IEEE Transactions on Instrumentation and Measurement* 70 (2020), pp. 1–13.
- [185] Serdar Soyoz and Maria Q Feng. “Long-term monitoring and identification of bridge structural parameters”. In: *Computer-Aided Civil and Infrastructure Engineering* 24.2 (2009), pp. 82–92.
- [186] Edwin Reynders and Guido De Roeck. “Continuous vibration monitoring and progressive damage testing on the Z 24 bridge”. In: *Encyclopedia of structural health monitoring* (2009).
- [187] *Arduino Nano 33 BLE Sense - Reference Manual*. URL: <https://docs.arduino.cc/resources/datasheets/ABX00031-datasheet.pdf>.
- [188] George Forman et al. “An extensive empirical study of feature selection metrics for text classification.” In: *J. Mach. Learn. Res.* 3.Mar (2003), pp. 1289–1305.